PREPARATION AND CHARACTERIZATION OF ELECTROSTATICALLY SELF-ASSEMBLED PERYLENE-DIIMIDE/POLYELECTROLYTE COMPOSITES

by

THOMAS A. EVERETT

B.S., Truman State University, 2004

AN ABSTRACT OF A DISSERTATION

submitted in partial fulfillment of the requirements for the degree

DOCTOR OF PHILOSOPHY

Department of Chemistry
College of Arts and Sciences

KANSAS STATE UNIVERSITY
Manhattan, Kansas

2010

Abstract

This doctoral thesis covers the synthesis, preparation, and characterization of a series of four perylene diimide derivatives, and the nanofibrous composite materials formed by these perylene diimides when complexed with oppositely charged polyelectrolytes. The perylene diimides include a symmetric dication ($TAPDI^{2+}$), a symmetric dianion ($PDISO_3^{2-}$), and two singly charged asymmetric varieties ($C_{11}OPDI^{+}$ and C_7OPDI^{+}) that contain a hydrophilic head group and hydrophobic ether tail. For all studies presented in the following chapters, poly(acrylate) (PA^{-}) or poly(diallyldimethylammonium) chloride ($PDDA^{+}$) are used as the polyelectrolytes (PEs). The patterned deposition of sheer aligned, nanofibrous material within a fluidic device is conclusively demonstrated. Thin films of the nanofibrous composite are prepared from aqueous solutions of the semiconducting perylene diimides and oppositely charged polyelectrolyte precursors. By sequentially exposing a clean glass substrate to the cationic and anionic precursor solutions, a thin film of composite material is deposited in a layer-by-layer fashion. By utilizing electrostatic self-assembly (ESA) and layer-by-layer (LbL) procedures, precise control of film thickness and optical density are obtained. The effect of perylene diimide structure and charge on resultant composite film morphology is explored. Through spectroscopic and microscopic studies of bulk perylene diimide solutions and composite thin films, it was determined that the formation of these fibrous materials is dependent on the aggregation of the PDI within the precursor solutions. The molecular orientation of the perylene diimide within the composite nanofiber was determined to be perpendicular to the fiber long axis. For the special case of C_7OPDI^{+}/PA^{-} composite, flow induced fiber alignment was observed for both dip coated and flow coated samples. The influence of solution flow profile, PE molecular weight (MW), and PDI structure on deposition efficiency, macroscopic and microscopic morphology, and the potential for nanofiber alignment are investigated. Film formation mechanisms involving two unique routes are also presented.

PREPARATION AND CHARACTERIZATION OF ELECTROSTATICALLY SELF-ASSEMBLED PERYLENE-DIIMIDE/POLYELECTROLYTE COMPOSITES

by

THOMAS A. EVERETT

B.S., Truman State University, 2004

A DISSERTATION

submitted in partial fulfillment of the requirements for the degree

DOCTOR OF PHILOSOPHY

Department of Chemistry
College of Arts and Sciences

KANSAS STATE UNIVERSITY
Manhattan, Kansas

2010

Approved by:

Major Professor
Dr. Daniel A. Higgins

Copyright

Abstract

This doctoral thesis covers the synthesis, preparation, and characterization of a series of four perylene diimide derivatives, and the nanofibrous composite materials formed by these perylene diimides when complexed with oppositely charged polyelectrolytes. The perylene diimides include a symmetric dication ($TAPDI^{2+}$), a symmetric dianion ($PDISO_3^{2-}$), and two singly charged asymmetric varieties ($C_{11}OPDI^{+}$ and C_7OPDI^{+}) that contain a hydrophilic head group and hydrophobic ether tail. For all studies presented in the following chapters, poly(acrylate) (PA^{-}) or poly(diallyldimethylammonium) chloride ($PDDA^{+}$) are used as the polyelectrolytes (PEs). The patterned deposition of sheer aligned, nanofibrous material within a fluidic device is conclusively demonstrated. Thin films of the nanofibrous composite are prepared from aqueous solutions of the semiconducting perylene diimides and oppositely charged polyelectrolyte precursors. By sequentially exposing a clean glass substrate to the cationic and anionic precursor solutions, a thin film of composite material is deposited in a layer-by-layer fashion. By utilizing electrostatic self-assembly (ESA) and layer-by-layer (LbL) procedures, precise control of film thickness and optical density are obtained. The effect of perylene diimide structure and charge on resultant composite film morphology is explored. Through spectroscopic and microscopic studies of bulk perylene diimide solutions and composite thin films, it was determined that the formation of these fibrous materials is dependent on the aggregation of the PDI within the precursor solutions. The molecular orientation of the perylene diimide within the composite nanofiber was determined to be perpendicular to the fiber long axis. For the special case of C_7OPDI^{+}/PA^{-} composite, flow induced fiber alignment was observed for both dip coated and flow coated samples. The influence of solution flow profile, PE molecular weight (MW), and PDI structure on deposition efficiency, macroscopic and microscopic morphology, and the potential for nanofiber alignment are investigated. Film formation mechanisms involving two unique routes are also presented.

Table of Contents

List of Figures

List of Tables

Acknowledgements

I would like to thank Dr. Dan Higgins for his leadership and teachings during my studies at Kansas State University. Through example, he has shown me what it is to be a good scientist. Without his guidance and timely critiques, my time here would have been much less productive and enjoyable.

It would also be unfitting to not give thanks to all the Higgins' group members that passed through while I was here, they were always ready to discuss experimental results, celebrate successes, and give insightful suggestions when things were not working. I would especially like to thank Dr. Jeff Lange who in addition to helpful discussion was always ready to accompany me on many duck hunting and fishing excursions around the central Kansas area. Without him my sanity would be even more questionable.

The faculty and staff at KSU are to be commended for their role in my success, especially Jim Hodgson, Tobe Eggers, Ron Jackson, Richard and Stuart Bachamp, Christer Aakeröy, Takashi Ito, Chris Culbertson, Pernilla Viberg, Kurt Hoeman and Scott Klasner. Without their efforts and aid this work would not be where it is today.

It would also be a mistake not to mention the sources of funding which ultimately made this work possible, they include; the National Science Foundation, the Office of Naval Research, and Kansas State University.

Lastly, I want to thank my wife, Christi, for her encouragement and never-ending support. Without her, I never would have made it.

Dedication

This work is dedicated to Christi, who I thank daily for her encouragement and eternal patience. I love you!

List of Abbreviations

LbL	Layer-by-Layer
ESA	Electrostatic Self-Assembly
PE	Polyelectrolyte
PDI	Perylene Diimide
$C_{11}OPDI^{+}$	N-(3(Octyloxy)propyl)-N'(2-(trimethylammonio)-ethyl)perylene-3,4,9,10-tetracarboxylic diimide Iodide
C_7OPDI^{+}	N-(3-(butoxypropyl)-N'(2-(trimethylammonio)-ethyl)perylene-3,4,9,10-tetracarboxylic diimide
$TAPDI^{2+}$	N,N'-bis(2-(trimethylammonio)ethyl)-Perylene-3,4,9,10-tetracarboxylic diimide
$PDISO_3^{2-}$	N,N'-bis(3-sulfonatopropyl)perylene-3,4,9,10-tetracarboxylic diimide
$PDDA^{+}$	Poly(diallyldimethylammonium)
PA^{-}	Poly(acrylic) Acid
PDMS	Poly(dimethylsiloxane)
MW	Molecular Weight
AFM	Atomic Force Microscope
ROI	Region of Interest
CI	Confidence Interval

CHAPTER 1 - Research Introduction

Layer-by-layer (LbL) deposition has recently gained much attention for the fabrication of thin films. LbL deposition is a versatile, self-assembly technique that utilizes many different inter- and intra-molecular forces for the preparation of multilayered, functional thin films. One subclass of the LbL technique is electrostatic self-assembly (ESA). In a typical ESA LbL procedure, the desired substrate, of arbitrary shape and size, is sequentially exposed to a series of solutions containing oppositely charged target molecules and/or polyelectrolytes (PE). Through electrostatic and hydrophobic forces, these molecules adsorb to the substrate surface, forming a uniform organic film. It is widely accepted that for this process to proceed, a complete surface charge reversal must occur.[1, 2] One aspect that makes LbL assembly such an interesting research topic is the degree of control that is not offered by alternative thin film preparation procedures (spin coating, drop casting, spray coating, sputtering, Langmuir-Blogdett, etc.). LbL deposition procedures allow precise control over the film's physical attributes, such as film thickness and composition. In addition, LbL procedures allow for very simple sample preparation and easy scale-up for industrial applications. This high degree of control allows scientists and engineers to custom design specialized materials better suited for their intended purpose.

History of Layer-by-Layer Procedures

LbL deposition was first demonstrated by R.K. Iler in 1966.[3] This pioneering work demonstrated the controlled deposition of colloidal thin films by alternately exposing a smooth surface (i.e. glass) to oppositely charged colloidal sols. In this early work, the author suggests that LbL deposition could be applicable to a large number of different systems. Despite the suggested utility of the thin film deposition technique, it was not until 26 years later that more focused research on LbL deposition was carried out.

In 1992, Decher, Hong, and Schmitt published the first in-depth study of ultrathin PE multilayered films.[4] This preliminary study is considered to be the first well

documented study on LbL deposition in which a mechanism of film formation is proposed. In this work, Decher demonstrated the deposition of four PE pairs; polystyrenesulfonate, polyvinylsulfate, poly-4-vinylbenzyl-((N,N-diethyl-N-methyl-)-ammonium iodide and polyallylamine hydrochloride. By alternately exposing a clean substrate to the oppositely charged PEss, a linear increase in absorbance and film thickness was observed for an optically clear polymer film. The absorbance increase was linear out to 100 alternating PE bi-layers with no significant changes in the films' absorption behavior. This work was the foundation of modern LbL studies and although it did identify that electrostatics were the major controlling interaction involved between the PE pairs, it did nothing to describe the structure and organization of the multiple PE bilayer.

Five years later, Decher published a second article in *Science* entitled "Fuzzy Nanoassemblies: Toward Layered Polymeric Multicomposites",[5] which presented a very clear and concise model of the multilayer polymeric films that he had previously produced. In this work, he proposed a model that could be used to describe any multilayered, polymeric film that was composed of simple flexible PEs.[5] The model suggests that discrete layered structures are actually never formed, as was previously believed. Instead, entangled bilayer morphologies are formed. For each bilayer deposited (which is typically composed of both a cationic and anionic component) there exists a concentration gradient across the bilayer thickness. Only at the extreme top and bottom of the bilayer does pure PE exist. In between the pure polyelectolytes, a mixture of cationic and anionic PE precursors exists, as shown in Figure 1.1.

Figure 1.1 Schematic of PE multilayer film. Grey color represents positively charged polymer and red color represents negatively charged polymer. Note the

gradual transition between the pure PE layers. Dashed lines show the polymer interfaces if NO intermixing was observed.

These early works on LbL deposition laid the ground work for subsequent scientists to explore new thin films and composite material constructed from a variety of compounds. From much of this subsequent work, the importance of hydrophobic effects (in addition to electrostatic effects) in driving self-assembly has become evident, and several new classes of materials have been developed. Materials such as polymer/small molecule composites, small molecule/small molecule composites, and polymer/nanoparticle composites, have been developed, some of which have found some interesting applications.

Functional LbL Polyelectrolyte Films

Since the preliminary LbL studies, much work has been done to explore the uses of multilayered films formed by the LbL process. Some of the more interesting applications that were developed from these early discoveries include controlled drug delivery, antimicrobial coatings, and bioprotective coatings.

Controlled drug delivery was achieved by Hammond et al.[6] In their work, they demonstrated the encapsulation of gentamicin into a multilayered PE composite.[6] They utilized a readily biodegradable, positively charged polymer and negatively charged gentamicin, then, through sequential deposition, degradable films were cast onto a nonedegradeable base film. Hammond was able to show that by simply controlling deposition conditions such as antibiotic concentration and PE concentration, they could ultimately control the gentamicin dose and release rate.

In a similar study, Kotov et al. demonstrated antimicrobial properties of a clay/PE/nanoparticle composite.[7] Through the addition of clay, the multilayer films were made mechanically robust, and the silver nanoparticles imparted antibacterial character to the resultant multilayer composite.

The previous two examples demonstrated the ability of LbL films to have both biocompatible and antibacterial properties. Such films could undoubtedly have useful applications in the healthcare industry, but they also only scratch the surface of possible

applications. For example, the research of Marchetti et al. demonstrated the use of LbL procedures to encapsulate pancreatic islet cells.[8] By encapsulation of the islet cells, the cells were protected against attack by the immune system, but still allowed secretion of insulin and cell waste through the encapsulation layer. Pioneering work such as Marchetti's will undoubtedly continue into the future, advancing science and technology as new discoveries are made.

LbL Deposition of Small Molecules

One of the more interesting areas, from both an academic and functional material standpoint, of modern LbL research is the use of small molecules in LbL ESA. Typically, small molecules are used in one of two ways, incorporation of charged small molecules with oppositely charged PE[9-16] or with a second oppositely charged small molecule.[17-20] What makes the use of small molecules interesting is the wide range of conformations the solid films may adopt. Unlike PE pairs that form films having layered architectures, films composed of small molecules may take on extended one dimensional fibrous structures.[21] The fact that these unique structures are formed in systems containing small molecules suggests that the film growth mechanism may be significantly different than that of films prepared by PE pairs only. Ultimately, this fundamental difference may lead to the development of new materials having applications in optics as new optical coatings,[10, 12, 14, 22-24] catalysts,[19, 25] chemical sensors,[25]and in the healthcare field.[6]

ESA for the Production of Aligned Materials

One aspect of LbL deposition, which for the most part has eluded researchers, is the ability of ESA techniques, including LbL deposition, to produce materials that exhibit an extended in-plane organization.

In an early study, Cooper et al. demonstrated the deposition of ordered multilayered compounds composed of polypeptide/dye multilayers.[9] The polypeptide used was a poly(L-lysine) hydrogen bromide salt and the anionic dyes, copper phthalocyanine tetrasulfonic acid (CPTA), alcian blue (AB) and congo red (CR). Cooper's results show a uniform increase in film thickness and optical density as a function of deposition cycle. They also noted evidence of induced ordering of the dye by

the polypeptide matrix. From linear dichroism measurements, they concluded that order was induced by solution flow present in the dipping process. Although their results suggest the possibility of producing aligned materials, no further attempts were made to verify or explain in greater detail this flow induced ordering phenomena.

In 2000, Lavrentovich et al. published a report demonstrating the deposition of lyotropic chromonic liquid crystalline dyes onto PE coated glass substrates.[26] Through primarily electrostatic interaction, the dye was adsorbed to the PE surface. After deposition of the dye compounds, the films were mechanically rubbed and then rinsed. The mechanical process of rubbing was found to induce in-plane alignment of the dye molecules. Even though this was a simple technique that ultimately resulted in aligned material, the use of mechanical means to induce alignment is undesirable in many applications.

LbL Deposition for the Production of Patterned Materials

A second challenge that researchers face is the task of depositing materials in a spatially defined, specific region. Such patterned deposition would be useful for the electronic industry in the construction of organic light emitting diodes, and other devices where accurate placement of active materials is necessary. A number of researchers have successfully shown the ability to form materials having a patterned, layered structure but only a few have demonstrated the controlled deposition of materials with definitive in-plane orientation.

For example, Lefaux and Mather demonstrated the patterned deposition of poly(styrene sulfonate) and Poly(allylamine hydrochloride) within a microfluidic device.[27] The use of the microfluidic chip allows the LbL deposition to only occur in the regions defined by the microfluidic channel. By changing the microfluidic architecture, specific patterns could be produced. This strategy works great for the production of patterned films. However, no control of film structure and organization on the molecular scale are obtained. Lefaux and Mather's work, although demonstrating patterned deposition of polymeric materials, did not show any in-plane organization.

In a related study by Lee et al., a microfluidic chip was employed to control the deposition of collagen fibers which were subsequently used for *in vitro* cell cultures.[28] In

their work, they demonstrated the patterned deposition of aligned collagen fibers and calculated the degree of alignment of the fibers within the microfluidic channels. Their results indicate that narrower microfluidic channels gave a narrower distribution of angles. However, for all cases they examined, they saw a preference of the collagen fibers to align parallel to the channel direction when solution was actively flowing.

Thesis Overview

The work described in the following chapters is the culmination of 5 years of academic research and the results obtained from this work. The original goal of the research project was to construct high efficiency photovoltaics (PVs) (i.e. solar cells) from water soluble perylene diimide and PE precursors. Like much research however, this ultimate goal was never completely realized. Early attempts at the fabrication of working PV devices utilized a coating technique known as drop casting. In drop casting, a drop of solution, which contains the active components, is placed onto the substrate and subsequently allowed to dry. The perylene diimide/PE films produced in this manner where typically non-uniform in nature and showed highly varied surface roughnesses. Even post-deposition procedures such as solvent vapor or thermal annealing did little to decrease the surface roughness. Ultimately, it was determined that a combination of surface pinholes and molecular aggregation of the perylene diimide were the root cause of the surface roughness and failure in producing working PV devices. This realization forced a change in the direction of my thesis project, to one more fundamental in nature, where innovative deposition techniques were used in hopes of easily producing uniform films. One of the first alternative deposition strategies attempted was layer-by-layer deposition. The unexpected observation of nanofibers in dip-coated perylene diimide/polyectrolyte films directed the research toward a more fundamental route, which closely examined how water soluble perylene diimide (PDI) aggregates in its respective precursor solution, how the aggregation impacts the film morphology and organization of electrostatic self-assembled composite films, and to a lesser degree how the aggregation could be controlled. The results from this research work toward understanding how preassembled molecular aggregates may be used to produce both patterned and aligned nanostructures in a bottom up fashion, and how, by better

understanding the film formation mechanism, ultimately more efficient PV devices may be constructed.

Chapter 2 of this dissertation discusses the experimental setups involved in the work. Included are the procedures used to synthesize the PDIs, construction and programming of the automated sample preparation robots, and the methods used to characterize the precursor solutions and the composite thin films. Chapters 3, 4, and 5 are the heart of the research; they discuss in detail the methodology and results of the experiments that were carried out. Chapter 6 summarizes the project in its entirety and outlines what could be the next steps required in this research project.

The appendices present additional information on other projects that I worked on during my tenure at Kansas State. Of these, only Appendix C: Multiphoton photolithography does not have a direct relation to the perylene diimide/PE project, although this technique could be useful in designing and implementing future experiments involving PDI/PE nanofibrous composites.

REFERENCES

(1) Dubas, S. T.; Schlenoff, J. B. *Macromolecules.* **1999**, *32*, 8153-8160.

(2) Schlenoff, J. B.; Ly, H.; Li, M. *J.Am.Chem.Soc.* **1998**, *120*, 7626-7634.

(3) Iler, R. K. *J. Colloid Interface Sci.* **1966**, *21*, 569.

(4) Decher, G.; Hong, J. D.; Schmitt, J. *Thin Solid Films.* **1992**, *210/211*, 831-835.

(5) Decher, G. *Science.* **1997**, *277*, 1232-1237.

(6) Chuang, H. F.; Smith, R. C.; Hammond, P. T. *Biomacromolecules.* **2008**, *9*, 1660-1668.

(7) Podsiadlo, P.; Paternel, S.; Rouillard, J. M.; Zhang, Z.; Lee, J.; Lee, J.; Gulari, E.; Kotov, N. A. *Langmuir.* **2005**, *21*, 11915.

(8) Krol, S.; Guerra, S.; Grupillo, M.; Diaspro, A.; Gliozzi, A.; Marchetti, P. *Nano Lett.* **2006**, *6*, 1933.

(9) Cooper, T. M.; Campbell, A. L.; Crane, R. L. *Langmuir.* **1995**, *11*, 2713-2718.

(10) Yoo, D.; Wu, A.; Lee, J. -.; Rubner, M. F. *Synth.Metals.* **1997**, *85*, 1425-1426.

(11) Yoo, D.; Lee, J. -.; Rubner, M. F. *Mat.Res.Soc.Symp.Proc.* **1996**, *413*, 395-399.

(12) Ariga, K.; Lvov, Y.; Kunitake, T. *J.Am.Chem.Soc.* **1997**, *119*, 2224-2231.

(13) Chang-Yen, D. A.; Lvov, Y.; McShane, M. J.; Gale, B. K. *Sensors and Actuators B.* **2002**, *87*, 336-345.

(14) Bradley, M. S.; Tischler, J. R.; Bulovic, V. *Adv Mater.* **2005**, *17*, 1881-1886.

(15) Everett, T. A.; Twite, A. A.; Xie, A.; Battina, S. K.; Hua, D. H.; Higgins, D. A. *Chem.Mater.* **2006**, *18*, 5937-5943.

(16) Weitzel, C. R.; Everett, T. A.; Higgins, D. A. *Langmuir.* **2009**, *25*, 1188-1195.

(17) Zhang, X.; Gao, M.; Kong, X.; Sun, Y.; Shen, J. *J.Chem.Soc.Chem.Commun.* **1994**, 1055-1056.

(18) Araki, K.; Wagner, M. J.; Wrighton, M. S. *Langmuir.* **1996**, *12*, 5393-5398.

(19) Tang, T.; Qu, J.; Mullen, K.; Webber, S. E. *Langmuir.* **2006**, *22*, 26-28.

(20) Doherty, W. J.; Friedlein, R.; Salaneck, W. R. *J.Phys.Chem.C.* **2007**, *111*, 2724-2729.

(21) Würthner, F.; Chen, Z.; Dehm, V.; Stepanenko, V. *Chem.Comm.* **2006**, , 1188-1190.

(22) Lee, J. -.; Yoo, D. S.; Handy, E. S.; Rubner, M. F. *Appl.Phys.Lett.* **1996**, *69*, 1686-1688.

(23) Durstock, M. F.; Spry, R. J.; Baur, J. W.; Taylor, B. E.; Chiang, L. Y. *J.Appl.Phys.* **2003**, *94*, 3253-3259.

(24) Clark, S. L.; Handy, E. S.; Rubner, M. F.; Hammond, P. T. *Adv Mater.* **1999**, *11*, 1031-1035.

(25) Ariga, K.; Hill, J. P.; Ji, Q. *Phys.Chem.Chem.Phys.* **2007**, *9*, 2319-2340.

(26) Schneider, T.; Lavrentovich, O. D. *Langmuir.* **2000**, *16*, 5227-5230.

(27) Lefaux, C. J.; Mather, P. T. *Mater.Res.Soc.Proc EXS-2 M.4.6.1-3.* **2004**,

(28) Lee, P.; Lin, R.; Moon, J.; Lee, L. P. *Biomed.Microdev.* **2006**, *8*, 35-41.

CHAPTER 2 - Experimental Methods

This chapter describes the synthesis of the perylene diimide compounds used throughout this dissertation. It also covers the construction and programming of the automated systems used in sample preparation and the techniques used in the characterization of the samples. Chapters 3, 4, and 5 give further detail on chemical structures, experimental setups and sample preparation conditions.

Perylene Diimide Synthesis

Synthesis of N-(3(octyloxy)propyl)-N'-(2-(trimethylammonio)ethyl)perylene-3,4,9,10-tetracarboxylic diimide iodide ($C_{11}OPDI^{+}\bullet I^{-}$)

Unless otherwise noted, all starting materials were obtained from Aldrich and used as received. Discussion of this synthesis is broken down into separate procedures used in the preparation of each precursor.

Preparation of 3-(octyloxy)propanenitrile (Performed by Srinivas K. Battina and Duy H. Hua)

A mixture of 4.0 g (76 mmol) acrylonitrile, 4.4 g (34 mmol) 1-octanol and 0.05 g (0.9 mmol) dry sodium methoxide was prepared in a nitrogen-purged flask. The reaction mixture was left stirring under positive nitrogen pressure for 24 h. Acetic acid (0.2 mL) was subsequently added and unreacted acrylonitrile was removed on a rotary evaporator. The product was collected by adding 25 mL of water to the flask, followed by extraction into four 25 mL portions of chloroform. The chloroform solution was dried over sodium sulfate and the faint yellow liquid product was collected by rotary evaporation. After further drying on a vacuum line, 3.8 g (62 % yield) of the product was obtained. NMR spectra showed the product to be of high purity. ^{1}H NMR (400 MHz, $CDCl_3$) δ 3.64 (t, 2 H, CH_2O), 3.48 (t, 2 H, CH_2O), 2.57 (t, 2 H, CH_2CN), 1.58 (pent, 2 H, CH2), 1.28 (bs, 10 H, CH_2), 0.88 (t, 3 H, CH_3) ppm.

Preparation of 3-(octyloxy)propanamine. (Performed by Srinivas K. Battina and Duy H. Hua)

To a solution of 5.0 g (27 mmol) 3-(octyloxy)propanenitrile in 20 mL of ethanol (distilled over magnesium), 0.2 g (0.9 mmol) platinum oxide was added. The mixture was placed in a hydrogenator and shaken under 30 psi hydrogen gas at room temperature for 1 day. Afterward, the mixture was diluted with ethanol, filtered through a layer of Celite, and concentrated to give 4.9 g (96% yield) of 3-(octyloxy)propanamine. The product was used without further purification. ^{1}H NMR (400 MHz, $CDCl_3$) δ 3.47 (t, 2 H, CH_2O), 3.39 (t, 2 H, CH_2O), 2.72 (t, 2 H, CH_2N), 1.85 (bs, 2 H, NH_2), 1.78 (pent, 2 H, CH_2), 1.56 (pent, 2 H, CH_2), 1.28 (bs, 10 H, CH_2), 0.88 (t, 3 H, CH_3) ppm; ^{13}C NMR (100 MHz, $CDCl_3$) δ 71.3 (t, CH_2O), 69.6 (t, CH_2O), 47.6 (t, CH_2N), 32.0 (t), 30.1 (t), 30.0 (t), 29.7 (t), 29.5 (t), 26.4 (t), 22.9 (t), 14.3 (q, CH_3) ppm; MS (electrospray CI) m/z 188.02 (M+1).

Preparation of N-(3-(octyloxy)propyl)-N'-(2-(N,N-dimethylamino)ethyl)perylene-3,4,9,10-tetracarboxylic diimide.

A one-pot procedure was employed in this synthesis. To a 300 mL round-bottom flask were added 300 mg (0.75 mmol) perylene tetracarboxylic dianhydride, 450 mg (2.4 mmol) 3-(octyloxy)propanamine, 67.6 mg (0.77 mmol) N,N-dimethylethylenediamine, and 200 mL of pyridine. The reaction mixture was refluxed and stirred under a nitrogen atmosphere for ≈ 24 h. The pyridine was subsequently removed on a rotary evaporator. The resulting solids were rinsed with three 25 mL portions of cold ethanol, collected by vacuum filtration, and dried under vacuum overnight. The crude product was a mixture of two symmetrically-substituted perylene diimides and the desired asymmetrically substituted compound. The asymmetric compound was obtained in high purity as the middle band on a silica gel column, using a mixture of chloroform, ethanol, and triethylamine (volume ratio of 20:1:0.1) as the eluent. After drying under vacuum, 110 mg (22% yield) of the desired product was obtained. ^{1}H NMR (400 MHz, $CDCl_3$) δ 8.6 (m, 8 H, perylene), 4.36 (m, 4 H, diimide CH_2N), 3.59 (t, 2 H, CH_2O), 3.40 (t, 2 H, CH_2O), 2.72 (t, 2 H, CH_2N), 2.39 (s, 6 H, $(CH_3)_2N$), 2.05 (pent, 2 H, CH_2), 1.45 (pent, 2 H, CH_2) 1.20 (bs, 10 H, CH_2), 0.82 (t, 3 H, CH_3) ppm. ^{13}C NMR (100 MHz, $CDCl_3$) δ

163.5 (4 C, C=O), 134.5 (4 C), 131.5 (4 C), 131.4 (4 C), 123.5 (2 C), 123.4 (2 C), 123.1 (2 C), 71.2, 69.1, 57.2, 46.0 (2 C), 38.6, 32.0, 30.0, 29.7, 29.5, 28.4, 26.4, 22.8, 14.4 ppm. MS (MALDI) m/z 632.37 (M+1).

Conversion to iodide salt ($C_{11}OPDI^{+}\bullet I^{-}$)

To a 100 mL-round-bottom flask containing a stir bar and 50 mL of chloroform were added 100 mg (0.16 mmol) N-(3-(octyloxy)propyl)-N'-(2-(N,N-dimethylamino)ethyl)perylene-3,4,9,10-tetracarboxylic diimide and 100 μL (1.6 mmol) of iodomethane. The reaction mixture was refluxed overnight under a nitrogen atmosphere. $C_{11}OPDI^{+}\bullet I^{-}$ precipitated from the solution as the reaction proceeded. Chloroform and excess iodomethane were removed on a rotary evaporator. The product was suspended and washed in three portions of ethanol, and was collected by centrifugation. The final product was obtained in good yield after drying overnight in a vacuum oven at 50°C. MS, (MALDI) m/z 646.27 (M+; without iodide); calculated m/z for $C_{40}H_{44}N_3O_5^{+}$: 646.33 (100%). The mass spectrum indicated the sample was of good purity.

Synthesis of N-(3(butoxypropyl)-N'-(2-(trimethylammonio)ethyl)perylene-3,4,9,10-tetracarboxylic diimide iodide ($C_7OPDI^{+}\bullet I^{-}$)

A one-pot procedure was employed in this synthesis. To a 300 mL round-bottom flask were added 0.75 mmol perylene tetracarboxylic dianhydride, 2.4 mmol 3-(butoxy)propanamine, 0.77 mmol N,N-dimethylethylenediamine, and 200 mL of pyridine. The reaction mixture was refluxed and stirred under a nitrogen atmosphere for ≈ 24 h. The pyridine was subsequently removed on a rotary evaporator. The resulting solids were rinsed with three 25 mL portions of cold ethanol, collected by vacuum filtration, and dried under vacuum overnight. The crude product was a mixture of two symmetrically-substituted perylene diimides and the desired asymmetrically substituted compound. The asymmetric compound was obtained in high purity as the middle band on a silica gel column, using a mixture of chloroform, ethanol, and triethylamine (volume ratio 20:1:0.1) as the eluent. After drying under vacuum, the desired product was

obtained. ^{1}H NMR (400 MHz, $CDCl_3$) δ 8.6 (m, 8 H, perylene), 4.32 (m, 4 H, diimide CH_2N), 3.59 (t, 2 H, CH_2O), 3.40 (t, 2 H, CH_2O), 2.72 (t, 2 H, CH_2N), 2.39 (s, 6 H, $(CH_3)_2N$), 2.05 (pent, 2 H, CH_2), 1.45 (pent, 2 H, CH_2) 1.5 (bs, 2 H, CH_2), 0.9 (t, 3 H, CH_3) ppm.

To convert the asymmetric product to the desired iodide salt, 0.16 mmols of N-(3-(butoxy)propyl)-N'-(2-(N,N-dimethylamino)ethyl)perylene-3,4,9,10-tetracarboxylic diimide was added to a 100 mL-round-bottom flask containing a stir bar, 50 mL of chloroform and 1.6 mmols iodomethane. The reaction mixture was refluxed overnight under a nitrogen atmosphere. $C_7OPDI^+ \bullet I^-$ precipitated from the solution as the reaction proceeded. Chloroform and excess iodomethane were removed on a rotary evaporator. The product was suspended and washed in three portions of ethanol, and was collected by centrifugation. The final product was obtained in good yield after drying overnight in a vacuum oven at 50^{o}C.

Synthesis of bis(trimethylammonioethyl)-perylene-3,4,9,10-tetracarboxylic diimide ($TAPDI^{2+} \bullet 2I^-$) (As performed by Corey R. Weitzel)

The symmetric TAPDI was prepared in two ways, directly and indirectly. The indirect procedure involved the synthesis of asymmetric $C_{11}OPDI$ or C_7OPDI, during which the symmetric TAPDI is produced as a secondary product which was collected during the purification of the target compound. For our purpose, it was sufficient to collect the desired symmetric product during the synthesis of the asymmetric compounds and subsequently covert it to the iodide salt (as described below). However, when the compound was to be synthesized purposefully, the following representative procedure was used:

To a round-bottom flask containing 100 mLs of pyridine, 0.79 mmols of perylene 3,4,9,10-tetracarboxylic dianhydride, and 3.68 mmols N,N-dimethylethylenediamine were added. The reaction mixture was then refluxed for 24 hours under a nitrogen atmosphere. After 24 hours, the pyridine was removed on a rotary evaporator. The resultant deep red solid product is the desired crude TAPDI. The crude TAPDI was then refluxed with with 100 mL 6% K_2CO_3 for 20 minutes to remove any unreacted perylene

dianhydride. The resultant dark green product was then collected by immediately filtering the hot solution through a fritted glass filter. The collected solid was then rinsed with the K_2CO_3 solution until filtrate was colorless, and subsequently dried with a brief cold acetone rinse followed by several rinses with high purity water. The resultant crude product was then dried in an oven at 65 °C for several hours. ^{1}H NMR (400 MHz, $CDCl_3$) δ 8.7 (m, 8 H, perylene), 4.4 (m, 4 H, diimide (CH_2N), 2.7 (t, 4 H, (CH_2N), 2.39 (s, 12 H, $(CH_3)_2N$) ppm.

To convert the purified symmetric product to the desired iodide salt, the bis(dimethylaminoethyl)-perylene-3,4,9,10-tetracarboxylic diimide was added to a 100 mL round-bottom flask containing a stir bar, 50 mL of chloroform and a molar excess of iodomethane. The reaction mixture was then refluxed overnight under a nitrogen atmosphere. The desired symmetric iodide salt, $TAPDI^{2+}•2I^-$, precipitated from the solution as the reaction progressed. After 12 hours the chloroform and excess iodomethane was removed on a rotary evaporator. The product was then further purified by suspending and washing with cold ethanol, followed immediately by centrifugation. The centrifugation process was repeated a minimum of 3 times to insure all iodomethane was removed. The final product was obtained in good yield after drying overnight in a vacuum oven at 50^{o}C.

Synthesis of N, N'-Bis(3-sulfonatopropyl)perylene-3,4,9,10-tetracarboxylic Diimide ($PDISO_3^{2-}$) (As performed by Corey R. Weitzel)

The synthesis of $PDISO_3^{2-}$ has been previously reported.[1] Briefly, this procedure involves the addition of perylene 3,4,9,10-tetracarboxylic dianhydride, zinc acetate and 3-aminopropane sulfonic acid in a 1:1:3 molar ratio to a round-bottom flask containing 140 mL of pyridine. The reaction mixture was then refluxed under nitrogen for 7 days. The crude product was then collected by vacuum filtration and rinsed with 3:1 (by volume) ethyl acetate:hexane solution. After drying in a vacuum oven at 80 °C for 8 hours, the product was dissolved in slightly basic water followed by centrifugation, which removed any insoluble products. After centrifugation, the product was precipitated from solution by combining with an equivalent volume of 2M HCl and collected by centrifugation, giving a dark red solid product which was subsequently transferred to a fritted filter and

rinsed with cold 1:1 (by volume) 2-propanol:ether solution. The collected product was then dried under vacuum overnight.

Layer-by-Layer Deposition

All samples were prepared using electrostatic self-assembly in a Layer-by-Layer (LbL) fashion.[2-4] In a typical LbL procedure, a glass substrate, which has a native negative charge, is sequentially exposed to a solution containing a cationic compound followed by a solution containing an anionic compound. Upon exposure to the charged precursor solutions a surface charge reversal takes place, allowing for the electrostatic self-assembly of the composite materials. This sequential process may then be repeated to "grow" films having the desired thickness and optical density. In addition, this procedure allows for precise control over sample composition and ultimately physical properties.

All LbL samples described in chapters 3 and 4 were prepared using a computer-controlled robotic dip-coater designed and constructed in-house. This dip-coater is described in more detail below. Samples as described in chapter 5, were prepared using a fluidic flow-control apparatus that is described below.

Dip Coater

Design and Construction

The computer controlled dip-coater that was constructed for use on this dissertation was designed to easily control all aspects of layer-by-layer assembly via computer control. The dip-coater was comprised of a rack and pinion gear set attached to a moveable vertical arm, on which the sample substrates were mounted, a multi-position turn-table, which allowed for the positioning of up to 8 unique deposition solutions, 2 stepper motors, two stepper motor controllers, and a personal computer. Figure 2.1 shows pictures of the dip coater with relevant parts marked. Mechanical motion of the sample and the deposition reservoirs was accomplished by the direct connection of the stepper motors to the rack and pinion gear set and to the central axis of the rotary table, respectively. Motion control was achieved through a custom Labview program that was written in-house and a personal computer. The computer was used to produce a 5 V TTL

pulse train which was subsequently translated by the stepper motor controllers to control the stepper motors. To achieve reproducible motion, mechanical and optical switches were used to indicate the "home" position of the vertical dip mechanism and the rotary table respectively. By indexing beaker positions and vertical displacement off of the "home" positions, precise control of dipping solution selection, and depth of dip was achieved.

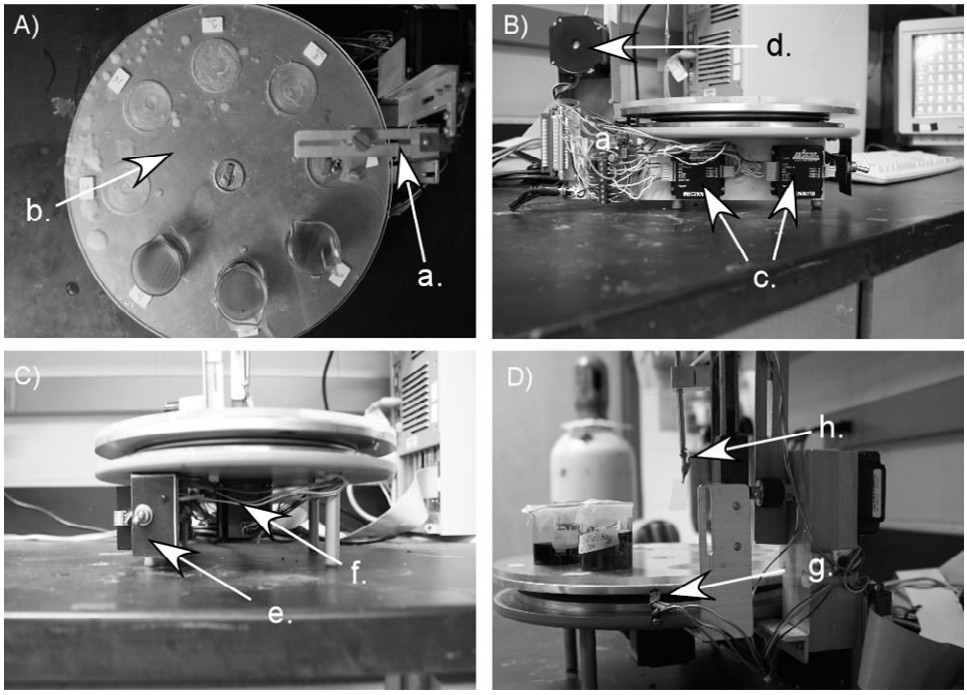

Figure 2.1 Dip-coater Images. Panel 2.1A shows a top-down view of the rotary table with room for up to 8 beakers (only 3 beakers shown) for precursor and rinse solutions. (a.) indicates the vertical dipping arm; (b.) indicates the rotary table. Panel 2.1B displays a side view of the dip coater, note the motor controllers (c.) and the vertical stepper motor (d.) indicated by the arrows. Panel 2.1C shows a front view of the dip coater, the power switch (e.) and rotary table's stepper motor (f) are shown. Panel 2.1D is a rear view of the dip coater showing the optical table switch (g.) and the substrate clip (h.).

Dip-Coater Software

Software for the dip coater was programmed using the National Instruments Labview programming environment. The main program can be broken down into 3 key processes, although the actual program is much more complicated.

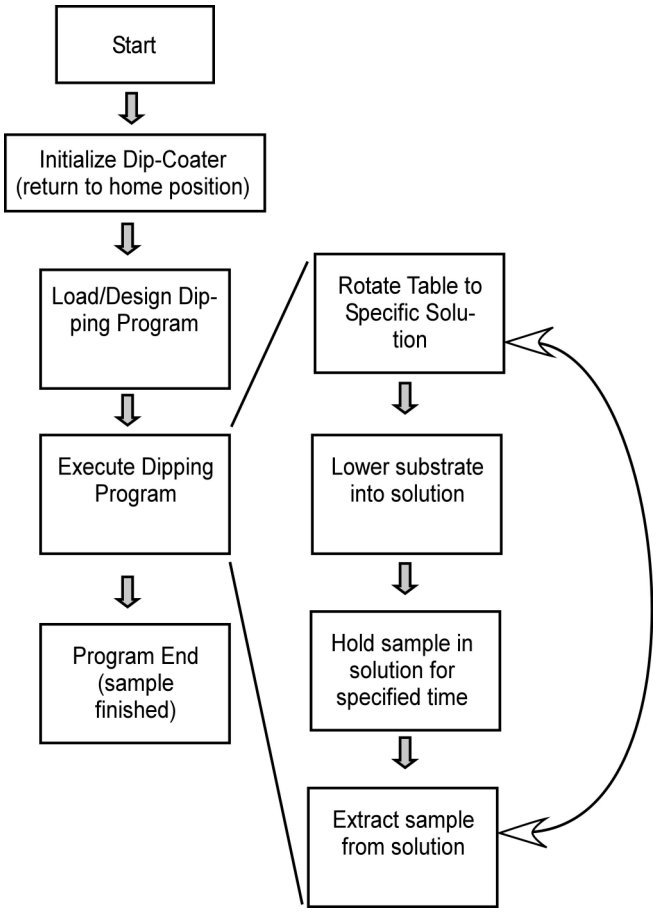

Figure 2.2 Dip-coater programming flow-chart

These processes are: dip coater initialization, dipping procedure input, and execution of procedure. A flow chart describing software execution is shown in Figure 2.2. The initialization of the dip coater was completed upon startup of the software, and involved rotating the rotary table until the optical switch is triggered, and the raising of the dipping mechanism until the mechanical limit switch is triggered. When both switches were triggered, the dip-coater was considered in the "home" position. Once at the "home" position the program proceeds to the dipping procedure programming screen. At the programming screen, the user has two options; 1) compose a new dipping procedure, or 2) load a previously saved procedure. If composing a new procedure, solution location, dipping rate, extraction rate and immersion time must all be specified for each individual solution to be used in the LbL procedure. Once finished, the user may choose to save the program for future use and then click "Done". At this point, the procedure program was executed. The rotary table is advanced to the first solution

location, which was previously defined in the dipping procedure. The vertical dipping mechanism was then engaged and the substrate was lowered into the precursor solution at the desired rate. Once the motor had traveled the predetermined distance, the robot went into a stand-by mode, counting down the time remaining for the substrate to remain in solution. After reaching the predetermined "pause time", the substrate was extracted from the solution until the dipping mechanism triggered it's home position limit switch, at which time the table advanced to the next solution position. This process was repeated until the dipping program was completed and the desired number of layers was achieved.

Microfluidic Solution Flow Control Apparatus

Design and Construction

The microfluidic flow apparatus used for controlled solution delivery during the microfluidic LbL deposition was designed to facilitate the fabrication of multilayered, patterned samples. The flow control apparatus was constructed as a modular device consisting of 3 solution reservoirs, 3 computer controlled solenoid pinch valves, a solenoid air valve, solenoid control module, a Plexiglas flowcell, a variable rate peristaltic pump, and a personal computer. By constructing the apparatus in a modular fashion, changes to the experimental setup could quickly and easily be accomplished Figure 2.3 shows both a diagram and pictures of the actual device, the white arrow in Figure 2.3B indicates one of the 3 solenoid pinch valves.

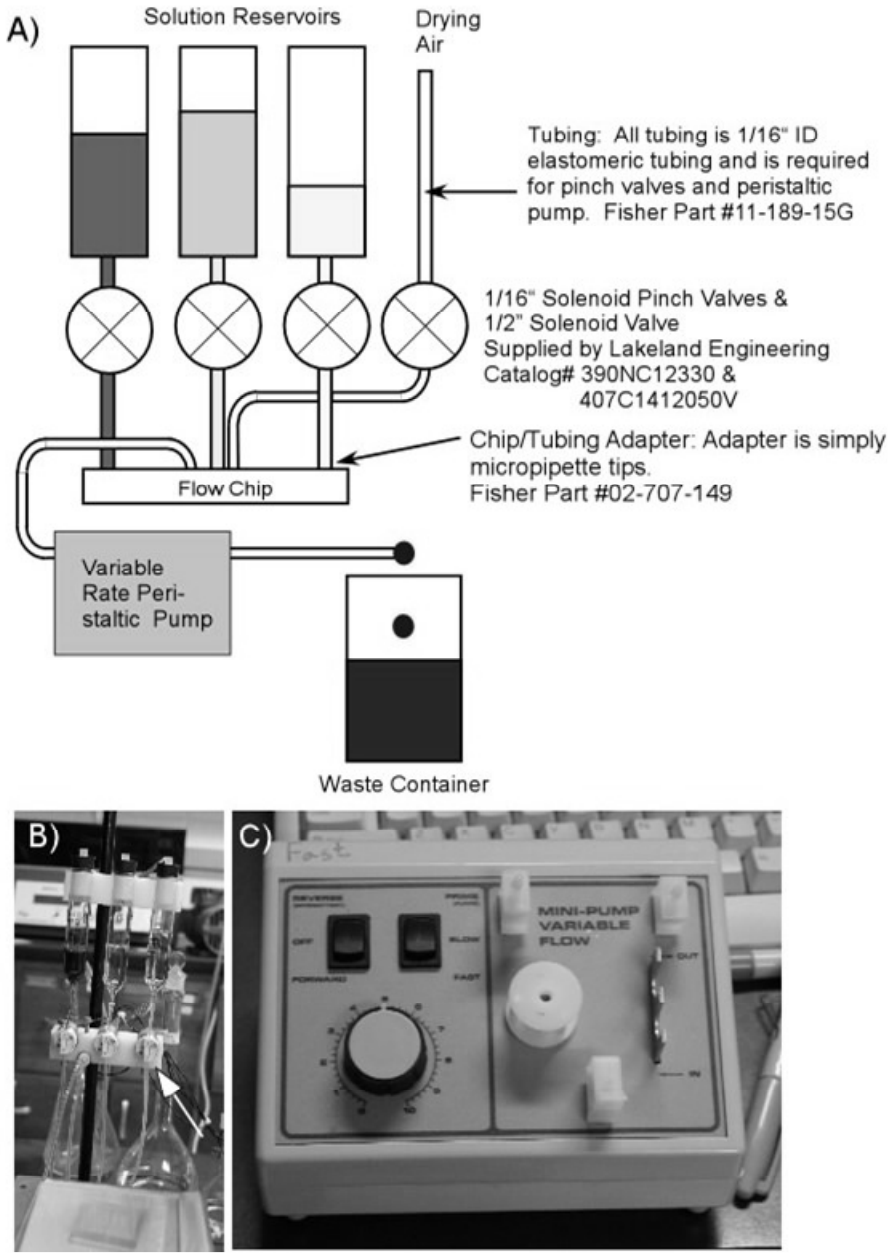

Figure 2.3 Flow Control Apparatus. A) Schematic diagram of microfluidic flow apparatus indicating all relevant part numbers and manufacturers for the modular setup. B) Photograph of solution reservoirs and solenoid pinch valves. The white arrow indicates one of the three pinch valves. C) Photograph of the peristaltic pump used to control solution flow rates.

By driving the pinch valves using the parallel port of a computer, software written in the Labview programming environment, and a variable rate peristaltic pump, control of the flow apparatus was achieved. Again, by utilizing computer control, better sample-to-

sample reproducibly was obtained in addition to accurate timing of solution flow duration and volume.

Flow Control Software

The computer software that controlled the flow apparatus acted as a timer and a switch, turning on and off the solenoid valves at program-determined intervals. The program allowed the user to load, edit or save a sample preparation procedure, in tabular form, and then execute the procedure. Figure 2.4 shows an example of a sample procedure that is read by the software.

Step Number	Solution Number	Hold Time (s)
1	1 (precursor)	30
2	2 (Rinse)	30
3	4 (dry)	30
4	3 (precursor)	30
5	2 (rinse)	30
6	4 (dry)	30

Figure 2.4 Sample Flow-apparatus procedure. The text in parenthesis, in the solution number column is only for clarification; in the actual program this text is omitted.

The sample procedure shown in Figure 2.4 has three columns indicating the step of the procedure, the solution number, and the length of time the solution would be flowed through the flow cell. Each row of the table represents a single step of the bilayer formation process. The completion of the 6 steps would yield a sample of 1 bilayer.

Solution flow rates were kept constant throughout the entire routine for preparing a sample. Solution flow rates were determined by the peristaltic pump used and the inside diameter of the elastomeric tubing (and to a lesser extent the dimensions of the fluidic device).

Sample Characterization

UV-vis

Absorbance spectra were collected using an HP 8453 diode array spectrometer. A custom made sample holder was constructed to allow collection of absorbance spectra from thin films. Figure 2.5 shows a model of the sample holder. For all collected spectra, an appropriate blank was used to correct for any absorbance offset that may have been introduced by the solvent or the substrate/cuvette.

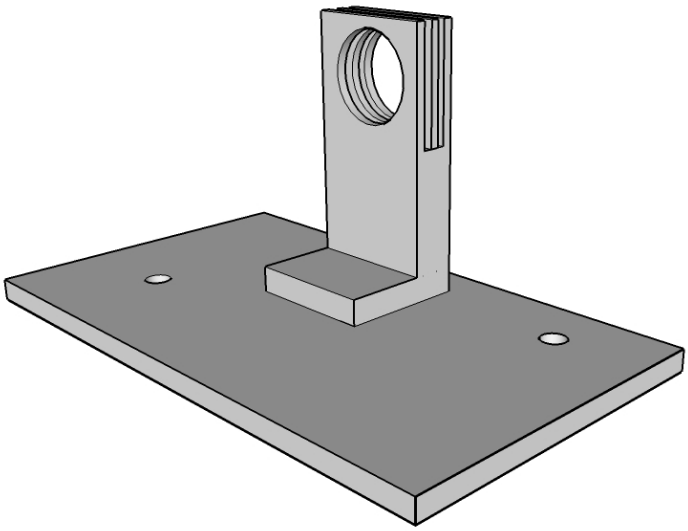

Figure 2.5 Thin-Film UV-vis sample holder

For absorbance dichroism measurements, as described in chapter 4, polarized absorbance spectra were collected. The polarization dependent absorption spectra were collected by inserting a calibrated sheet polarizer between the sample holder and the light source, resulting in linearly polarized incident light. A clean glass coverslip was then placed into the sample holder and a blank absorbance spectrum was recorded. Next, the PDI composite sample was placed in the sample holder such that the incident light was polarized either parallel or perpendicular to the dipping direction (the samples were prepared by the dipcoating process) and a sample absorbance spectrum was recorded. The sample was then rotated 90° and a second sample spectrum was collected. After the absorbance spectra were corrected for scattering and fit using the spectral fitting procedure described below, the sample dichroism was calculated using the peak absorbances following:

$$D = \frac{A_{\parallel} - A_{\perp}}{A_{\parallel} + A_{\perp}}$$

where the subscripts indicate the corrected absorbance for light polarized parallel to the dipping direction or polarized perpendicular to the dipping direction. The sign of the D-value indicates if the perylene molecules within the film have a preferential orientation, while the magnitude of D indicates the overall degree of order. A D-value of +1 indicates perfect alignment of the PDI chromophore's long axis (i.e. parallel to the PDI hydrophobic tails) parallel to the dipping direction, and a D-value of -1 indicates perfect alignment of the PDI chromophore long axis perpendicular to the dipping direction.

Background Subtraction and Spectral Fitting

In most cases the accurate determination of PDI absorbance at 490 nm was needed. This was accomplished through background subtraction and subsequent mathematical fitting of the background subtracted spectra.

To correct for elastic light scattering (i.e. Rayleigh scattering), which is proportional to λ^{-4}, the recorded absorption spectrum background was fit to an exponential function. Though theory tells us scattering intensity is proportional to wavelength, in practice, fitting the absorption spectra to a simple exponential function was sufficient for the correction of the absorption spectra. Subtracting the fit function from the absorption spectra resulted in the scattering corrected absorption spectra. The corrected subtracted spectra was then fit to the double gaussian function:

$$F(x) = B + H_1 e^{-\left(\frac{(P_1 - X)}{W_1}\right)^2} + H_2 e^{-\left(\frac{(P_2 - X)}{W_2}\right)^2}$$

Where B is the y-offset value, H_1 and H_2 are the height of the peaks 1 and 2, P_1 and P_2 are the peak positions in nm, and W_1 and W_2 are the width of the peaks, again in nm. Through this fitting process, the maximum absorbance magnitude could be directly taken as the optimized P_1 values.

Fluorescence

Through the course of this work, fluorescence spectra were recorded using a SPEX Fluoromax-2 fluorimeter. Both thin film and bulk solution spectra were recorded. Typically, a standard cell holder was used. However, when needed, a home built heated/cooled cell holder was used. Figure 2.6 shows a cartoon of the home-built cuvette holder. Note the inlet and outlet ports on the front of the cell holder that were connected to an actively heated or chilled water bath.

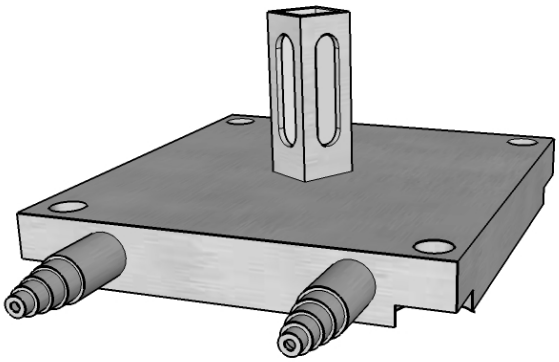

Figure 2.6 Heated/Cooled fluorescence cell holder. The inlet and outlet ports are shown, and are located on the front of the cell holder.

Van't Hoff Plots

In chapter 4, studies of the temperature dependent aggregation of three perylene diimide derivatives are reported. In these studies a series of fluorescence emission spectra were recorded as a function of solution temperature, for each of the three different perylene diimide derivatives. The peak intensity for each spectrum was determined and a plot of the natural log of the fluorescence intensity vs. 1/Temperature (K) was made. It was assumed that the nonfluorescent PDI aggregates existed in a dynamic equilibrium which was modeled by the following equilibrium process:

$$PDI_n \Leftrightarrow PDI_{n-1} + PDI^*$$

where PDI_n represents the non-fluorescent PDI aggregate containing n monomers and PDI^* designates a fluorescent monomer or monomer-like species. Under these conditions it was assumed that the aggregate concentration was relatively constant and the observed fluorescence was primarily due to the monomer-like species. Thus, it could

be assumed that the fluorescence intensity was proportional to the equilibrium constant. By fitting the plots to a best fit line, a measure of the equilibrium dissociation constant was obtained. Additionally the change in enthalpy and change in entropy was calculated from the slope and y-intercept following the Van't Hoff equation.

$$\ln K = -\frac{\Delta H}{RT} + \frac{\Delta S}{R}$$

Optical Microscopy (Confocal)

Confocal sample scanning microscopy was used to study how the PDI/PE composite materials form and how perylene diimide was organized in thin films. Figure 2.7 shows the general microscope setup, which has been described previously,[5] with only the most critical optical components shown. These parts include an argon-ion laser, with the 514 nm laser line selected (typically at a power of 200 nW), mirrors, high numerical aperture objective lens (NA = 1.3), a high precision sample scanning stage, a dichroic mirror that reflects 514 nm light and passes longer wavelengths, a filter set to select the emission of the desired wavelength, that was subsequently detected by the avalanche photo diode.

Images were obtained by raster scanning the sample across the laser focus. Any fluorescence emitted by the sample was instantaneously collected by the objective and directed to the avalanche photo diode for detection. Images were built up on a pixel by pixel basis until a complete image was formed. Typical images were 100 X 100 pixels and 10 X 10 um.

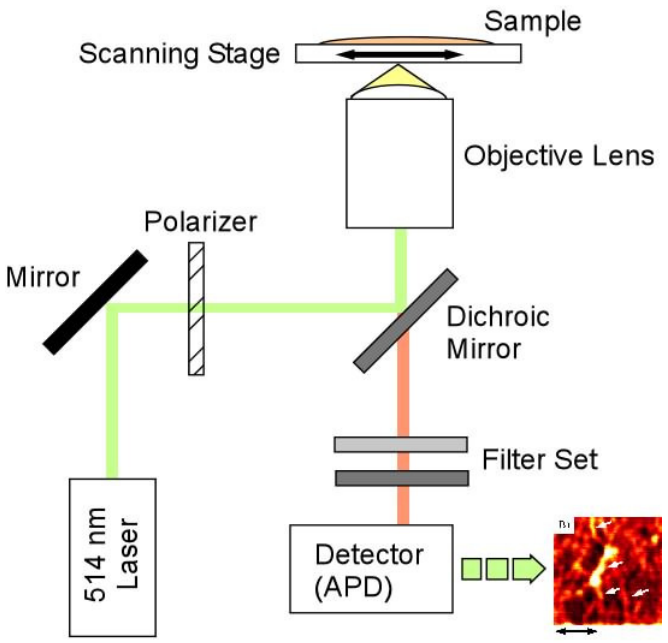

Figure 2.7 Confocal Microscope. Shown is the typical organization of optical components for the confocal microscope. The key components include the laser light source, dichroic mirror, objective lens, scanning sample stage, and the avalanche photo diode detector. Not shown is the computer that is used to process and reassemble the fluorescence image.

Tapping-Mode Atomic Force Microscopy (TM-AFM)

Atomic force microscopy, a type of scanning probe microscopy, was used extensively through the course of this work. The ultra-high resolution (ability to image single atoms under ideal conditions) enabled the visualization of nanofibers that were not resolvable using optical microscopy techniques. Although very high spatial resolution was attained using this technique, no chemical information was obtained.

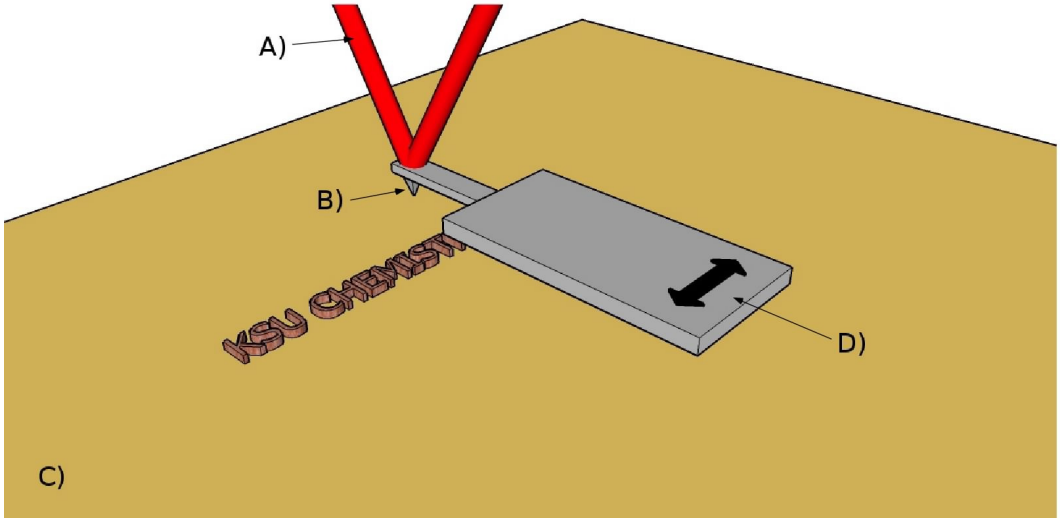

Figure 2.8 Schematic of an Atomic Force Microscope. A) Indicates the laser beam. B) AFM tip. C) Planar substrate, and D) Cantilever.

There are several different modes in which AFM may be operated; for the majority of our samples tapping mode was selected as it typically imparts less mechanical forces onto the sample, preventing the tip from damaging the sample surface. Figure 2.8 shows a cartoon drawing of a typical atomic force microscope. In this figure the sample is represented by the planar substrate, labeled C) in Figure 2.8, with "KSU CHEMISTRY" protruding from the surface. The cantilever and attached tip, labeled B) and D), in Figure 2.8 are shown with an arrow indicating the scan direction. At the tip of the cantilever, a "V" is located; this large V represents the laser, labeled A) in the Figure 2.8, that is directed onto and reflected off of the back side of the cantilever and focused to a position sensitive detector (not shown). When operated in tapping mode, the cantilever and tip oscillate at a specific resonate frequency with a given magnitude. As the dithering cantilever approaches and touches the sample surface, a change in the oscillating magnitude is detected and the instrument quickly changes the sample's vertical position in an attempt to maintain the original oscillation magnitude. Thus, by monitoring the change in vertical position and mapping it on a pixel by pixel basis, a microscopic view of the surface features is obtained.

Image Analysis

Determination of directionality of fiber orientations from AFM or optical microscopes is not trivial. To date, many studies have utilized methods that rely heavily

on human image interpretation; this undoubtedly introduces a substantive amount of bias in their image analysis results.[6] In an attempt to make quantitative assessments of nanofiber alignment two automated procedures were used for AFM image analysis, Hessian analysis and image autocorrelation.

Hessian analysis

The Hessian analysis routine has been reported by Elbischger et. al. for the determination of collagen fiber orientation.[7] For our purpose, their procedure was modified slightly; it involved calculating the image hessian from the original image, followed by the determination of the eigenvalues and eigenvectors of the hessian image, which gives the magnitudes and direction of the second directional derivative respectively for an image. By plotting the eigenvector on a pixel by pixel basis, an eigenvector map was made. A histogram of the eigenvector map shows the angle distribution (in degrees) for all pixels within the image. Ideally, all pixels within a nanofiber would have a similar eigenvector, yielding a measure of fiber alignment.

Although it seems like an ideal analysis procedure, some problems were encountered; namely, large features and extremely small features caused the program to give skewed data, and not report an accurate average angle for nanofiber alignment. For example, in large fibers minor deviations in the fiber height would cause the eigenvector to point in a wrong direction. To correct this, complicated masking would have been necessary, this in turn would have introduced a degree of human bias into the results, thus a second image analysis routine was developed.

Image autocorrelation analysis

The second image analysis technique used is based on 2D image autocorrelation. Image autocorrelation is the cross correlation of an image with itself. The data from autocorrelation processes such as this typically are used to find populations of features of a given size within a signal. For our purpose, we used it to quantify nanofiber orientation.

Using ImageJ, an AFM image or optical image was first loaded, the image was then analyzed using the autocorrelation routine. The resultant autocorrelated images look nothing like the original; they have a large bright circular or oval central region that

quickly decays to black along the edges. As with most autocorrelated data, only a small fraction is used in making statistical measurements, for us this meant using only a small 30 X 30 pixel region around the image center. After selecting this central region and constructing a new image from the 30 x 30 pixel area, the azimuthal distribution is determined. This function plots the average autocorrelated pixel value as a function of the azimuthal angle (around the bright singularity within the autocorrelation image). By plotting the data in this manner slight variation in the decay rate become evident The data was then copied and pasted into Igor Pro (scientific data analysis program), where it was subsequently normalized and fit to a $\cos^2$ function. From the fit data the phase angle (theta, nanofiber alignment direction) and amplitude (degree of alignment) were recovered.

Polarized Absorbance Imaging

In order to determine the degree of nanofiber alignment within thin film samples (as in Chapter 5) an inverted light microscope fitted with a polarizer and a narrow band pass filter was used to record polarized absorbance images. The microscope setup is shown in Figure 2.9.

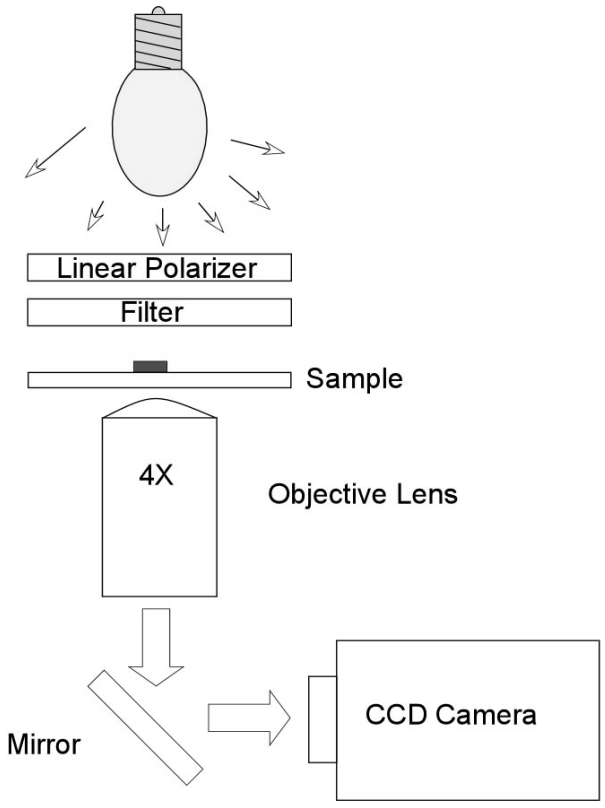

Figure 2.9 Inverted light microscope w/filter and polarizer

Absorbance images were obtained by first recording a dark image followed by two transmission images of a clean bare substrate with the incident polarization set to 0 and 90 degrees. By recording two sample transmission images with incident polarization set to 0 and 90 degrees (with respect to sample flow direction) polarization dependent absorbance images could then be calculated by:

$$A = -Log\left(\frac{I_{sample} - I_{dark}}{I_{blank} - I_{dark}}\right)$$

Where I_{sample} is the sample transmission image, I_{dark} is the dark transmission image, and I_{blank} is the transmission image obtained from the clean glass coverslip. This calculation was repeated for both 0 and 90 degree incident polarizations.

REFERENCES

(1) Ye, F.; Higgins, D. A.; Collinson, M. M. *J.Phys.Chem.C.* **2007**, *111*, 6772-6780.

(2) Decher, G. *Science.* **1997**, *277*, 1232-1237.

(3) Ariga, K.; Hill, J. P.; Ji, Q. *Phys.Chem.Chem.Phys.* **2007**, *9*, 2319-2340.

(4) Hammond, P. T. *Adv Mater.* **2004**, *16*, 1271-1293.

(5) Hou, Y.; Bardo, A. M.; Martinez, C.; Higgins, D. A. *J Phys Chem B.* **2000**, *104*, 212-219.

(6) Lee, P.; Lin, R.; Moon, J.; Lee, L. P. *Biomed.Microdev.* **2006**, *8*, 35-41.

(7) Elbischger, P. J.; Bischof, H.; Regitnig, P.; Holzapfel, G. A. *Pattern Anal.Applic.* **2004**, *7*, 269-284.

CHAPTER 3 - Preparation and Characterization of Nanofibrous Perylene-Diimide-Polyelectrolyte Composite Thin Films

Introduction

Perylenetetracarboxylic diimides (PDIs) have numerous potential applications in Xerography,[1] organic electronics[2] and solar energy conversion.[3] Contemporary research on PDIs usually involves the design and synthesis of new derivatives having enhanced solubility and/or unique modes of self-assembly. An important recent trend has been the development and implementation of water-soluble PDIs.[4] Water-soluble PDIs have been shown to exhibit lyotropic (chromonic) and thermotropic liquid crystallinity.[5-7] PDIs substituted at the "bay" positions have also been prepared and used in the self-assembly of novel composites that take advantage of both hydrogen bonding[8-10] and ionic intermolecular interactions.[7,8,11] Ionic interactions between oppositely charged PDIs have also been employed in the layer-by-layer (LBL) self-assembly of "pure" PDI thin films[11] and composites.[12,13] The main purpose behind much of this work has been the optimization and control of materials organization. Improved organization may lead to the development of organic thin film solar cells with enhanced energy conversion efficiencies and/or other unique properties, such as materials flexibility and the ability for self-repair.

Our group has recently undertaken the development and characterization of new PDI-based composite films formed by complexation of charged, water-soluble, asymmetrically-substituted PDIs and oppositely charged polyelectrolytes.[14] The PDI-PE composites obtained are reminiscent of common PE-surfactant composites,[15] and previously-reported PDI-surfactant composites.[6,7] As in these other systems, self-

assembly of the PDI-PE composites is a highly cooperative process and relies on electrostatic interactions between the polyelectrolyte and PDI, along with π–π interactions and hydrophobic interactions of the PDIs themselves.

In an initial publication on these materials, the Higgins group showed that composite films comprised of an asymmetrically-substituted PDI ($C_{12}PDI^+$) and poly(acrylate) could be prepared by simply drop casting them from a single homogeneous solution of the two precursors.[14] The films obtained were comprised of semi-ordered, sub-micrometer sized clusters that incorporated "truncated" PDI-polyelectrolyte bilayers. These films exhibited diode-like behavior when included in rudimentary p-n heterojunction devices and yielded measurable photovoltages when exposed to visible light. Unfortunately, film discontinuity appeared to limit exciton hopping and electrical conductivity. In addition, $C_{12}PDI^+$ was of limited solubility (≈ 100 μM solutions could be obtained). To overcome these limitations new PDIs that exhibit better water solubility have been developed. We have also begun to explore alternative film deposition procedures that may lead to films of better/alternative morphologies.

In this chapter, the use of sequential deposition methods as a means to prepare PDI-polyelectrolyte composite thin films comprised of intertwined nanofibers is demonstrated. The resulting materials are characterized using a number of spectroscopic and microscopic methods. A new asymmetrically-substituted PDI (designated $C_{11}OPDI^+$) is employed, while poly(acrylate) (PA^-) is used as the polyelectrolyte. The structures of $C_{11}OPDI^+$ and PA^- are given in Figure 3.1and Figure 3.2.

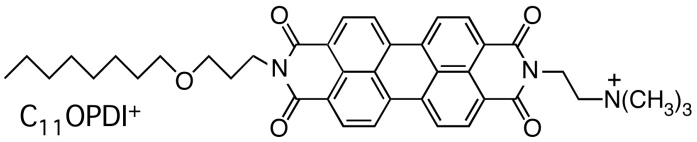

Figure 3.1 Structure of the Perylene Diimide Employed ($C_{11}OPDI^+$)

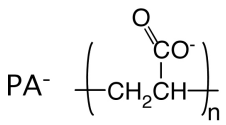

Figure 3.2 Structure of Poly(acrylate) Monomer (PA^-)

A long-chain ether was incorporated as one of the imide substituents in $C_{11}OPDI^+$ to help improve solubility.[16] Sequential deposition was chosen on the expectation that

repeatedly dipping the films into separate solutions of the two components would result in effective "solvent annealing" of the materials as they were deposited. In addition, relatively slow growth of the composites during sequential deposition was expected to yield films comprised of larger domains of ordered structures.

While the sequential deposition process employed herein is similar to well-known LBL deposition,[11-13] the film structures obtained differ dramatically from the usual "layered" architectures (i.e. nanofibers are formed). While nanofiberous PDI-based structures have been reported previously for both pure PDI systems[8,11,17-21] and other composites,[6-8] formation and deposition of the fibers described herein is dramatically enhanced by incorporation of the polyelectrolyte. Nanofiber formation in these materials results from binding and aggregation of $C_{11}OPDI^{+}$ along the polyelectrolyte "backbone". In the future, these nanofibers may find applications as semiconducting "wires" [10,18,19] in organic electronics and photovoltaics. Important advantages of these materials over existing alternatives include the ability to cast them on arbitrary substrates from aqueous solution, and the potential for increased material strength, due to binding of $C_{11}OPDI^{+}$ to the polyelectrolyte.

Experimental Considerations

Deposition of $C_{11}OPDI^{+}$•PA^{-} Composite Films

$C_{11}OPDI^{+}$ and PA^{-} were deposited on clean glass microscope coverslips by sequentially dipping them into 1) a 270 μM aqueous solution of $C_{11}OPDI^{+}$ (1 min dip), 2) deionized water (30 s dip), 3) a 2.43 mM (pH = 7, unbuffered) aqueous solution of sodium PA^{-} (concentration based on monomer, 1 min dip) and 4) deionized water (30 s dip). A withdrawal rate of 2 mm/s was used in each case. This sequence was repeated up to 55 times during deposition of thin film samples. Prior to use, the microscope coverslips had been cleaned by exposing them to an air plasma for 5 min.

All solutions were prepared using 18 MΩ·cm water. $C_{11}OPDI^{+}$ solutions were prepared by first dissolving the compound in methanol. An equal volume of water was then added and the solution brought to a boil. After evaporation of the methanol, the remaining aqueous solution was transferred to a volumetric flask, allowed to cool, and subsequently diluted to the mark with water.

Characterization of $C_{11}OPDI^{+}$•PA^{-} Composite Films

Thin film and solution phase fluorescence spectra of $C_{11}OPDI^{+}$ and its complex with PA^{-} were obtained using a SPEX Fluoromax-2 fluorimeter. Absorption spectra were obtained on an HP-8453 diode array spectrometer. A clean coverslip was used as the reference in thin film absorption spectra.

Composite thin film morphology was characterized by tapping mode AFM, using a Digital Instruments Multimode AFM. Molecular organization in the films was characterized using polarization-dependent confocal fluorescence microscopy. A home-built sample scanning confocal microscope that has been described previously was used.[22] Briefly, the sample being imaged sits on top of a closed loop piezoelectric scanning stage (±3 nm reproducibility) that is mounted on an inverted epi-illumination microscope (Nikon). Light at 514 nm from an argon ion laser (Coherent) was used to excite the sample. This light was delivered to the microscope via a single-mode optical fiber. Prior to entering the microscope, the laser light was first directed through polarization optics for control of both the incident power and polarization state. The light was then directed into the back aperture of a high numerical aperture (NA = 1.3) oil immersion objective, by reflection from a dichroic mirror. The objective produced a diffraction-limited focused spot of light in the sample. Typical average incident powers used were ≈ 200 nW. Fluorescence from the sample was collected using the same objective, and was subsequently directed into the detection path. Residual excitation light was removed with appropriate notch (Kaiser Optical) and bandpass (Chroma Technologies) filters. A single-photon-counting avalanche photodiode (Perkin Elmer) was employed as the detector. In polarization dependent studies, the incident polarization was alternately set parallel and perpendicular to the scan direction by use of a 514 nm halfwave plate (Special Optics). Total fluorescence (i.e. all polarizations) was detected.

Results and Discussion

Bulk Solution-Phase Spectroscopy

Solution phase spectroscopic studies were performed to determine the form (i.e. monomer or aggregate) of $C_{11}OPDI^{+}$ present in aqueous solution, and hence, to better understand its deposition. $C_{11}OPDI^{+}$•I^{-} is reasonably soluble in water, with

concentrations as high as 0.3 mM readily prepared in the absence of electrolytes. Figure 3.3

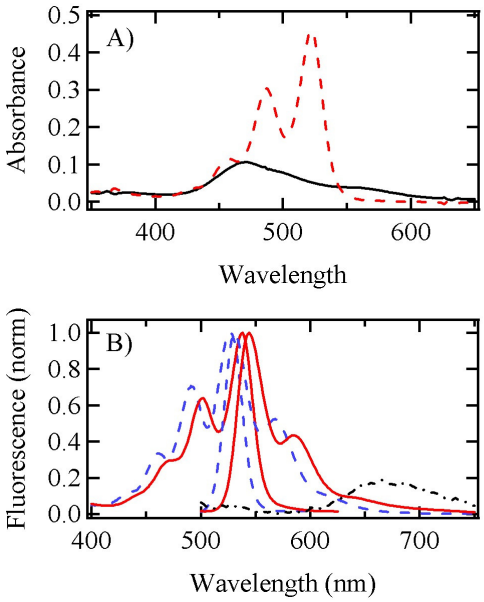

Figure 3.3 (A) UV-vis spectra of 10 μM $C_{11}OPDI^+$ in aqueous solution (solid line) and in methanol (dashed line). (B) Normalized fluorescence excitation (monitoring 650 nm) and emission spectra (exciting at 488 nm) of 10 μM $C_{11}OPDI^+$ in aqueous solution (solid line) and in methanol (dashed line). Also shown is the emission spectrum of 10 μM $C_{11}OPDI^+$ in the presence of 20 μM PA- (dotted and dashed line). Fluorescence emission from $C_{11}OPDI^+$ in water is about 21 times weaker than in methanol. Emission from the $C_{11}OPDI^+$• PA^- complex is about 100 times weaker than from $C_{11}OPDI^+$ in methanol. Aqueous $C_{11}OPDI^+$ and $C_{11}OPDI^+$• PA^- emission spectra are plotted on the same scale.

depicts several absorption and fluorescence spectra obtained from dilute (i.e. 10 μM) solutions. Absorption spectra recorded for aqueous solutions (see Figure 3.3A) are significantly broadened and blue shifted from the monomer spectrum, indicating $C_{11}OPDI^+$ is present in an aggregated form. The monomeric form of $C_{11}OPDI^+$ is observed in methanolic solution at this same concentration. The monomer spectrum in methanol appears as a simple vibronic progression, with an origin at 522 nm (Figure 3.3A).

In contrast to the absorption spectrum of aqueous $C_{11}OPDI^+$, the fluorescence excitation and emission spectra obtained at the same 10 μM concentration are clearly those of the monomer. Figure 3.3B shows representative fluorescence spectra obtained in water and methanol. Aside from a slight solvent-dependent shift, and a change in emission intensity, both aqueous and methanolic solutions yield mirror-image spectra that appear as simple vibronic progressions. These results indicate that essentially all fluorescence from aqueous solutions comes from a small amount of monomeric $C_{11}OPDI^+$ The fact that the fluorescence excitation and absorption spectra are so dramatically different indicates that the aggregates formed by $C_{11}OPDI^+$ alone are nonfluorescent.

While the $C_{11}OPDI^+$ fluorescence spectra in water and methanol are qualitatively similar in appearance, the difference in emission intensities from these two solutions is profound (as are the molar absorptivities; in water at 470 nm it is10643 $L/mol^{-1} \cdot cm^{-1}$, in methanol at 522 nm it is 45902 $L/mol^{-1} \cdot cm^{-1}$) The fluorescence obtained from an aqueous 10 μM solution of $C_{11}OPDI^+$ is ≈ 5% of that from an equivalent methanolic solution. Neglecting any difference in fluorescence quantum yields for monomeric $C_{11}OPDI^+$ in methanol and water, the monomer likely comprises < 10% of the species present in 10 μM aqueous solutions. It is therefore concluded that $C_{11}OPDI^+$ is present predominantly in an aggregated form at the much higher concentrations used in thin film deposition, as described below.

Also shown in Figure 3.3B is the emission spectrum for a $C_{11}OPDI^+ \bullet PA^-$ complex in aqueous solution. Unlike the aggregates formed in the absence of polyelectrolyte, the $C_{11}OPDI^+ \bullet PA^-$ complex is somewhat fluorescent. Emission from this sample falls predominantly in a broad, featureless, excimer-like emission band centered at ≈ 670 nm. Emission in this region is observed only for superstoichiometric complexes and is approximately five fold weaker than the monomer emission obtained in the absence of PA^-. These observations suggest the PDI chromophores take on a tightly π-stacked structure in the absence of polyelectrolyte and in substoichiometric complexes. In superstoichiometric complexes, the $C_{11}OPDI^+$ clearly forms a different type of aggregate, perhaps with greater chromophore spacing and mobility, as controlled by the polyelectrolyte. In this latter case, the chromophores assume a geometry that allows for

excimer formation. In the former, emission must be forbidden by the symmetry properties of the aggregate. Subtle changes in the π-stacking of PDI chromophores have been shown previously to lead to dramatic changes in their spectroscopic properties.[23, 24]

Sequential Deposition of Composite Films

Deposition of $C_{11}OPDI^{+}$•PA^{-} composite thin films was accomplished by sequentially dipping a clean microscope coverslip into four separate solutions (aqueous $C_{11}OPDI^{+}$, water, aqueous PA^{-}, and water) as defined in Experimental Considerations. The same strong polyelectrolyte binding and aggregation processes active in the solution phase studies described above are also expected to occur during sequential deposition.

Figure 3.4A presents representative thin-film absorption spectra obtained after different numbers of deposition cycles. Here, a single "deposition cycle" involves dipping a coverslip sequentially into all four solutions listed above. Figure 3.4B depicts a representative bulk fluorescence spectrum obtained from these same films. Both the peak absorbance and emission intensity from the films increase with the number of deposition cycles. However, the shapes and positions of the spectra show only very subtle changes over the full range of deposition cycles employed (from one to 55). Hence, it may be concluded that while the amount of material deposited increases with the number of deposition cycles, the structure of the aggregated composite materials remains relatively unchanged.

The aggregates formed in the composite thin films are similar to, but somewhat different from those found in 10 μM aqueous solution. Notably, the thin film absorption spectra have a slightly more pronounced shoulder at 560 nm. Likewise, the excimer-like emission observed from the thin films is slightly blue-shifted from that observed in solution (660 nm vs 670 nm). Although the exact structural differences in the film and solution aggregates are not known, subtle changes in PDI packing are likely involved.[23, 24]

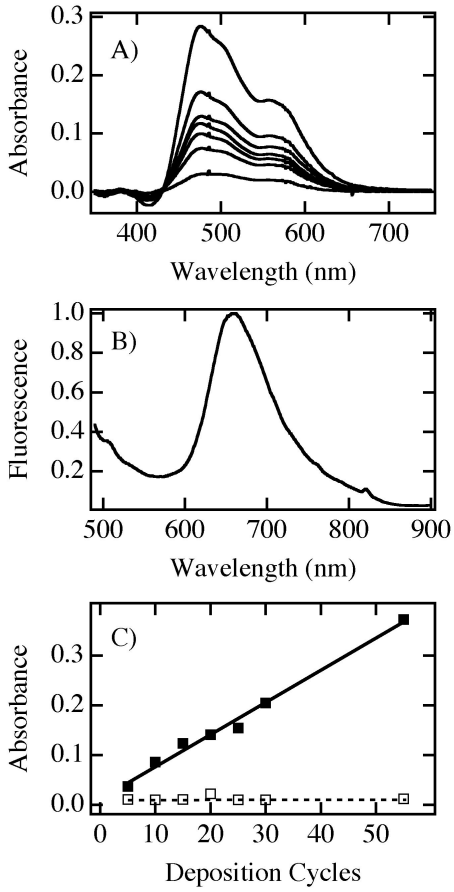

Figure 3.4 (A) UV-vis spectra (corrected for scattering) from $C_{11}OPDI^{+}$•PA^{-} composite films as a function of the number of deposition cycles. The spectra shown are for 5, 10, 15, 20, 25, 30 and 55 cycles (increasing absorbance). (B) Fluorescence spectrum from a composite film deposited in 20 cycles. (C) Peak absorbance at 480 nm taken from (A) as a function of the number of deposition cycles. Data obtained for both the composite (filled squares) and in the absence of PA^{-} (open squares) are shown.

The thin-film absorption spectra (Figure 3.4A) show a monotonic increase in absorbance with the number of deposition cycles. Figure 3.4C plots the peak absorbance (at 480 nm) observed. This plot is surprisingly linear, given the film morphology depicted below. A slope of 0.005 absorbance units per dipping cycle is obtained, indicating facile deposition of $C_{11}OPDI^{+}$occurs in the presence of PA^{-}. In contrast, relatively little material is deposited in the absence of the polyelectrolyte. Absorbance data obtained as a function of the number of dipping cycles in this case are also plotted in Figure 3.4C. As

is readily apparent, the slope of the plot obtained in the absence of PA^- is dramatically smaller than for the composite. It is concluded that PA^- is necessary for efficient deposition of the thin films prepared herein and that PA^- is an integral component of the nanofibrous structures described below.

Composite Film Morphology

Tapping mode AFM images of the sequentially deposited films show that they are highly nonuniform and are comprised of novel intertwined nanofibers. Representative images of films obtained after 5, 10, 20 and 30 deposition cycles are shown in Figure 3.5. While related nanofibers have been observed previously in films deposited from pure PDIs,[8, 11, 17-21] and in PDI-surfactant composites,[6, 7] to the authors knowledge, nanofiberous PDI-polyelectrolyte composites have never before been reported.

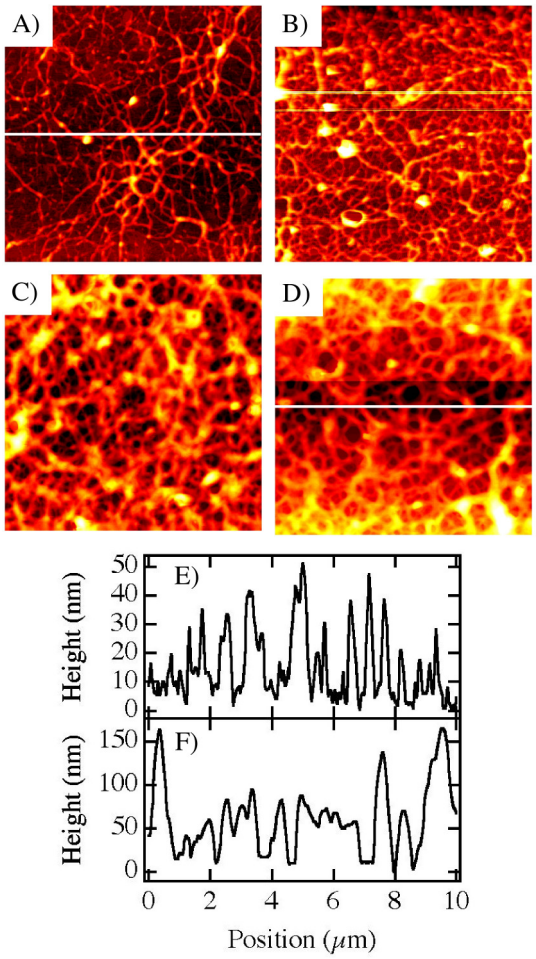

Figure 3.5 Tapping-mode AFM images of films prepared using (A) 5, (B) 10, (C) 20, and (D) 30 deposition cycles. Each image is of a 10 x 10 um^2 region. (E) and (F)

Line profiles taken across the images in (A) and (D), providing information on feature height and width.

The nanofibers of the $C_{11}OPDI^{+}$•PA^{-} composite films are generally observed to be several micrometers to tens of micrometers in length. Their cross-sectional dimensions increase with the number of deposition cycles employed. Qualitative data on this trend may be found in the line profiles plotted in Figure 3.5E,F in which both fiber height and width are shown to increase. Observation of the nanofiberous morphology is independent of the amount of material deposited, however, up to the maximum number of deposition cycles studied (i.e., 55).

As with $C_{11}OPDI^{+}$ deposition, formation of the nanofibers is greatly enhanced in the presence of PA^{-}. Figure 3.6 shows an AFM image acquired for $C_{11}OPDI^{+}$ deposited in 30 cycles, without PA^{-}. Similar images are obtained after only a single deposition of $C_{11}OPDI^{+}$. The amount of material deposited (after more than one cycle) is clearly much smaller than is observed for the composite (as is consistent with the UV-vis data presented above). More importantly, very few nanofibers are observed in AFM images of films deposited without PA^{-}. This result provides direct support for the conclusion that PA^{-} is an integral component of the fibers and that it plays a central role in determining the nanofibrous morphology of these composites.

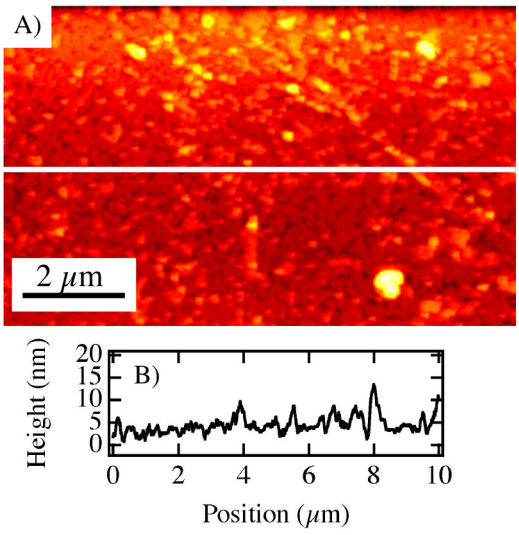

Figure 3.6 (A) Tapping-mode AFM image of $C_{11}OPDI^{+}$ prepared without PA^{-} in 30 deposition cycles. (B) Line profile taken across this image, showing feature height and width.

The observation of nanofibers also depends on the exact method employed for materials deposition. $C_{11}OPDI^{+}•PA^{-}$ composites drop cast from a single, homogeneous solution of the two precursors yield films of nanoclusters, not nanofibers. Film morphology in this case is identical to that observed in our previous studies of related drop cast $C_{12}PDI^{+}•PA^{-}$ composites.[14] Nanofiber size and film morphology is believed to depend on rate of fiber growth and therefore varies with concentration, temperature, ionic strength, and solution pH.

Nanofiber Size

As noted above, the size of the $C_{11}OPDI^{+}•PA^{-}$ nanofibers increases with the number of deposition cycles. Quantitative data on nanofiber size were obtained by performing autocorrelations of the AFM images[25, 26] along two dimensions, as defined in by

$$C(\xi) = \frac{\langle h(x+\xi)h(x)\rangle}{\langle h(x)^2\rangle}$$

Here, h(x) represents the topographic height (i.e. a line profile) along either the horizontal or vertical directions and C(ξ) is the resulting autocorrelation. The brackets in Eqn. 1 indicate that a spatial average is taken. Figure 3.7 depicts a subsection of a tapping mode AFM image obtained from a film deposited in five cycles. Figure 3.7B depicts the autocorrelations obtained from this image. These autocorrelations actually represent the average autocorrelations obtained from all 512 vertical and horizontal line profiles comprising the image.

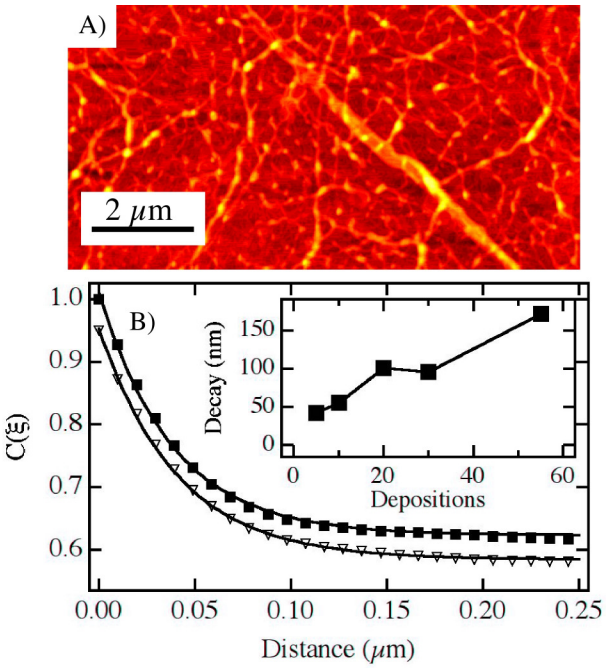

Figure 3.7 (A) Tapping mode AFM image of a sample prepared using five deposition cycles. (B) Autocorrelation functions derived from the image in (A) along the horizontal (solid squares) and vertical (open triangles) directions in the image. The vertical autocorrelation data has been offset along the y-direction to aid in visualization. Inset: characteristic nanofiber size as a function of deposition cycles.

The distance over which each autocorrelation function decays provides a measure of nominal nanofiber size. Since only short-range information can be extracted from such autocorrelations (i.e. insufficient information on sample features that are large relative to the image size exists), the information obtained is actually proportional to the average nanofiber cross-sectional size. Both height and width information are included in this data in part due to convolution of the AFM probe shape with sample features of different heights. The autocorrelation decays are also broadened by the random orientations of the nanofibers. While it is not possible to present an exact model for the mathematical form of the autocorrelation decays under these circumstances, they are observed to fit well to single exponentials (see Figure 3.7B). The inset shown in Figure 3.7B plots the average feature size (i.e. the exponential decay constant) observed for

different numbers of deposition cycles. As is clearly apparent from these data, nanofiber size increases with the number of cycles.

The rate at which the fibers grow with the number of deposition cycles is also important. Initially, fiber size increases rapidly from zero to an average of 40 nm when as few as five deposition cycles are employed. The fiber growth rate appears to decrease as more material is deposited, although film thickness continues to increase. This can be readily explained by noting that as the fibers grow, the gaps between individual fibers fill in to form a continuous film. At the same time, new fibers also nucleate and grow, leading to a sort of "steady state" nanofiber size for relatively thick films.

Chromophore Alignment and Fiber Structure

Chromophore organization within the composite nanofibers was probed by polarization-dependent confocal fluorescence microscopy. Figure 3.8 depicts two representative fluorescence images of the same sample region, excited with polarized 514 nm light. The two images shown were recorded under orthogonal incident polarization conditions, as designated by the appended double-ended arrows. Total fluorescence was detected (i.e. no analyzer was used). As is apparent from these data, most efficient fluorescence excitation occurs when the incident polarization is oriented approximately perpendicular to the (local) long axis of the individual nanofibers. Since the lowest energy electronic transition in PDI-based chromophores is known to be polarized along the long axis of the molecule (i.e. along the axis running between the imide moieties),[24, 27, 28] it may be concluded that the PDI chromophores are stacked with their conjugated ring planes oriented approximately perpendicular to the local nanofiber axis. This same alignment has been observed previously in other PDI-based nanofibrous materials.[20]

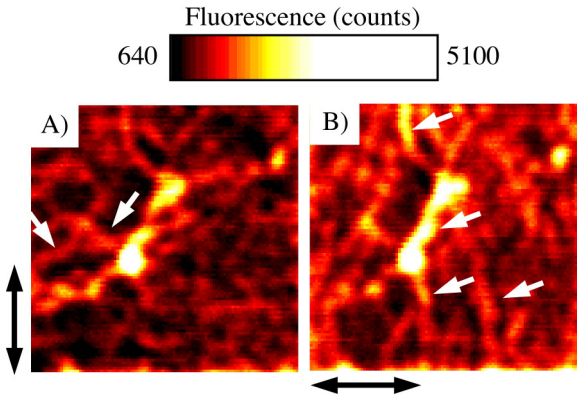

Figure 3.8 Polarization-dependent confocal fluorescence microscopy images (10 x 10 um^2) of $C_{11}OPDI^+/PA^-$ composite films recorded under the incident polarizations designated by the appended black arrows. The white arrows point to representative polarization-dependent features in the images. This sample was prepared in 10 deposition cycles.

Figure 3.9 shows a model for the proposed organization of the composite nanofibers. In this model, the fibers are comprised of parallel rows of $C_{11}OPDI^+$ π-stacks. The $C_{11}OPDI^+$ rows are separated by their interdigitated ether tails, forming a nonpolar region sandwiched between aromatic domains. The charged headgroups of $C_{11}OPDI^+$ and the polyelectrolyte then form highly ionic regions on the outsides of the fibers. The highly intertwined fibers are actually believed to incorporate short segments of the structures depicted in Figure 3.9. Disruption of this structure allows for the fibers to "bend", as observed in images of these materials.

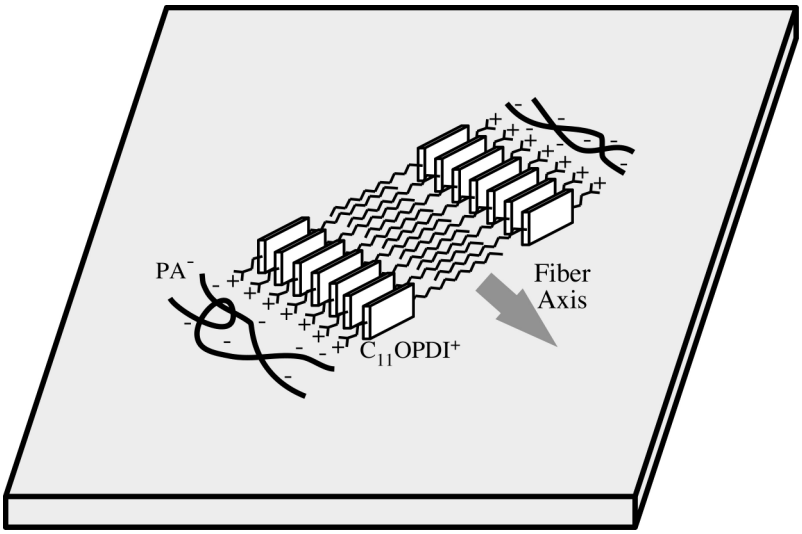

Figure 3.9 Model for $C_{11}OPDI^{+}/PA^{-}$ composite organization in short segments of the composite nanofibers.

Alternative organizational models for the fibers may also be proposed. For example, they may also result from formation of columnar stacks of $C_{11}OPDI^{+}$ surrounded by polyelectrolyte.[17] At the present time, the available data do not allow for a distinction to be made between these two models and either may be correct. The parallel π-stack organization proposed here was selected as being most likely because it allows for most parallel stacking of the PDI chromophores.

Fiber Growth Mechanism

The differences in film morphology observed for the materials deposited sequentially and from homogeneous mixtures provide important clues as to the fiber growth mechanism. Again, sequential deposition of $C_{11}OPDI^{+}$ and PA^{-} from separate aqueous solutions appears to greatly enhance nanofiber formation. Fiber growth in sequentially-deposited composites is attributed in part to the "solvent annealing" that likely occurs during deposition. The mostly-insoluble surface-bound composites may slowly rearrange to form fibrous structures as they are repeatedly dipped into the various solutions. It is also very likely that slow growth of the composites aids fiber formation. During sequential deposition, only a small amount of material is deposited in each dipping step. Some material is also removed during subsequent rinsing. As a result, composite formation is relatively slow, and somewhat like a slow crystallization in which

larger more uniformly organized structures can grow. Fibers are not prevalent in films drop cast from homogeneous aqueous solution because the complexes form extremely rapidly. Short aggregated structures result in this case. Finally, it is also very clear that different aggregate morphologies and polymer conformations exist in the aqueous solutions used in sequential deposition. The polymer in homogeneous aqueous solution (in the presence of $C_{11}OPDI^{+}$) likely takes on a collapsed conformation, surrounding short segments of $C_{11}OPDI^{+}$ aggregates. By itself, PA^{-} would take on a relatively more extended conformation. The binding of extended (rather than collapsed) PA^{-} strands could also aid in nanofiber growth. For its part, the $C_{11}OPDI^{+}$ likely forms short "fibers" in solution with or without the polyelectrolyte. During sequential deposition, these short fibers likely bind to the pre-existing PA^{-} film and behave as templates or nucleation sites for continued fiber growth in future deposition cycles.

Conclusions

In summary, sequential deposition of nanofibrous perylene-diimide-polyelectrolyte composites from aqueous solutions has been demonstrated. The films prepared incorporate long, intertwined, composite nanofibers, as observed by AFM and optical microscopy. Film growth and nanofiber formation is greatly enhanced by incorporation of the polyelectrolyte. Such fibers are not readily observed in drop-cast films of the same materials, indicating that sequential deposition also enhances fiber formation. It is believed that nanofiber formation results from solvent-annealing and slow-growth effects that occur when short aggregated PDI segments and extended polyelectrolyte strands are sequentially deposited. Polarization-dependent fluorescence imaging indicates that the chromophores in the fibers are oriented perpendicular to the long fiber axis. It is concluded that the fibers are comprised of parallel π-stacked $C_{11}OPDI^{+}$ assemblies sandwiched between polyelectrolyte regions. These composites have several advantages over existing alternatives, including the fact that they are deposited from aqueous solutions and that incorporation of the polyelectrolyte is expected to increase the mechanical strength of the resulting materials. The nanofibers obtained are expected to behave as semiconducting "wires" with possible applications in large-area, flexible, organic photovoltaic thin films.

REFERENCES

(1) Law, K.-Y. Chem. Rev. 1993, 93, 449.

(2) Witte, G.; Woell, C. J. Mater. Res. 2004, 19, 1889.

(3) Gregg, B. A. J. Phys. Chem. B 2003, 107, 4688.

(4) Kohl, C.; Weil, T.; Qu, J.; Mullen, K. Chem. Eur. J. 2004, 10, 5297.

(5) Tam-Chang, S.-W.; Iverson, I. K.; Helbley, J. Langmuir 2004, 20, 342.

(6) Zakrevskyy, Y.; Faul, C. F. J.; Guan, Y.; Stumpe, J. Adv. Func. Mater. 2004, 14, 835.

(7) Guan, Y.; Zakrevskyy, Y.; Stumpe, J.; Antonietti, M.; Faul, C. F. J. Chem. Comm. 2003, 894.

(8) Würthner, F. Chem. Comm. 2004, 2004, 1564.

(9) Würthner, F.; Thalacker, C.; Sautter, A. Adv. Mater. 1999, 11, 754.

(10) Schenning, A. P. H. J.; Herrikhuyzen, J. V.; Jonkheijm, P.; Chen, Z.; Würthner, F.; Meijer, E. W. J. Am. Chem. Soc. 2002, 124, 10252.

(11) Tang, T.; Qu, J.; Mullen, K.; Webber, S. E. Langmuir 2006, 22, 26.

(12) Martinson, A. B. F.; Massari, A. M.; Lee, S. J.; Gurney, R. W.; Splan, K. E.; Hupp, J. T.; Nguyen, S. T. J. Echem. Soc. 2006, 153, A527.

(13) Marcon, R. O.; dos Santos, J. G.; Figueiredo, K. M.; Brochsztain, S. Langmuir 2006, 22, 1680.

(14) Xie, A.; Liu, B.; Hall, J. E.; Barron, S. L.; Higgins, D. A. Langmuir 2005, 21, 4149.

(15) Zhou, S.; Chu, B. Adv. Mater. 2000, 12, 545.

(16) Cormier, R. A.; Gregg, B. A. Chem. Mater. 1998, 10, 1309.

(17) Würthner, F.; Chen, Z.; Dehm, V.; Stepanenko, V. Chem. Comm. 2006, 1188.

(18) Balakrishnan, K.; Datar, A.; Oitker, R.; Chen, H.; Zuo, J.; Zang, L. J. Am. Chem. Soc. 2005, 127, 10496.

(19) Balakrishnan, K.; Datar, A.; Naddo, T.; Huang, J.; Oitker, R.; Yen, M.; Zhao, J.; Zang, L. J. Am. Chem. Soc. 2006, 128, 7390.

(20) Datar, A.; Balakrishnan, K.; Yang, X.; Zuo, X.; Huang, J.; Oitker, R.; Yen, M.; Zhao, J.; Tiede, D. M.; Zang, L. J. Phys. Chem. B 2006, 110, 12327.

(21) Herrikhuyzen, J. V.; Syamakumari, A.; Schenning, A. P. H. J.; Meijer, E. W. J. Am. Chem. Soc. 2004, 126, 10021.

(22) Hou, Y.; Bardo, A. M.; Martinez, C.; Higgins, D. A. J. Phys. Chem. B 2000, 104, 212.

(23) Klebe, G.; Graser, F.; Hädicke, E.; Berndt, J. Acta Cryst. 1989, B45, 69.

(24) Kazmaier, P. M.; Hoffmann, R. J. Am. Chem. Soc. 1994, 116, 9684.

(25) Petersen, N. O.; Höddelius, P. L.; Wiseman, P. W.; Seger, O.; Magnusson, K.-E. Biophys. J. 1993, 65, 1135.

(26) Suzuki, A.; Yamazaki, M.; Kobiki, Y.; Suzuki, H. Macromolecules 1997, 30, 2350.

(27) Adachi, M.; Murata, Y.; Nakamura, S. J. Phys. Chem. 1995, 99, 14240.

(28) Struijk, C. W.; Sieval, A. B.; Dakhorst, J. E. J.; van Dijk, M.; Kimkes, P.; Koehorst, R. B. M.; Donker, H.; Schaafsma, T. J.; Picken, S. J.; van de Craats, A. M.; Warman, J. M.; Zuilhof, H.; Sudhölter, E. J. R. J. Am. Chem. Soc. 2000, 122, 11057.

CHAPTER 4 - Aggregation and its Influence on Macroscopic In-Plane Organization in Thin Films of Electrostatically Self-Assembled Perylene-Diimide/Polyelectrolyte Nanofibers

Introduction

Layer-by-layer (LbL) deposition is now widely employed for the preparation of thin films.[1-3] LbL methods most commonly involve the repeated dipping of a substrate into ionic solutions of suitable, oppositely-charged precursors. Precursor binding to the growing film is generally accepted to arise from both electrostatic and hydrophobic effects, leading to a reversal of the surface charge with each deposition.[4,5] The resulting materials most commonly take on a layered architecture.[6] LbL methods were first introduced for the electrostatic self-assembly (ESA) of polyelectrolytes (PEs).[3,7-10] Since that time, the same dip-coating procedures have also been found useful in ESA of a variety of materials,[1] including oppositely-charged pairs of small molecules[11-14] and charged small molecules with oppositely-charged PEs.[15-21] The latter are the subject of this chapter. While ESA of PE pairs is very common and widely studied, deposition of small molecules (frequently dyes) with PEs is less well understood. Importantly, the mechanisms for film growth during deposition of dye/PE composites may differ significantly from those involved in ESA of PEs alone. In some cases, these mechanistic differences may result in the growth of films having unique morphological and organizational characteristics.[21] While fundamentally interesting in their own right, dye/PE films also find potential applications in optical coatings and devices,[16,17,20,22-24] catalysts,[13] and chemical sensors.[1,19]

Many of the same factors known to control ESA of PE pairs are also important in the deposition of dye/PE composites. As is the case for PEs alone, deposition of dyes

with PEs is known to depend upon the concentration, pH and ionic strength of the precursor solutions.[15,25-28] The nature of the substrate has also been shown to play a significant role in the process.[15,29] One of the most important differences that arises in the deposition of dyes with PEs stems from the tendency of some dye molecules to form aggregates. Dye aggregation can occur both in solution (i.e. prior to deposition)[28,30] and upon adsorption to the growing film.[18,20] The appearance of such aggregates is a clear indication that hydrophobic effects play an important role in governing the deposition process. Furthermore, aggregate formation, whether in solution or in the film itself, is expected to yield materials that differ from the usual layered architectures. Most interesting, however, is the possibility that aggregation may lead to the growth of materials exhibiting macroscopic in-plane organization of the dyes.

Dye aggregation and its impact on dye/PE ESA have been studied previously by a number of research groups. In an early study, Kunitake and coworkers[18] employed quartz crystal microbalance methods and UV-vis absorbance to investigate the self-assembly of several different anionic low molecular weight dyes with a cationic PE. It was concluded that film growth was independent of aggregation in the precursor solution, but that adsorption to the coated substrate induced dye aggregation. The latter process had a significant impact on both the efficiency of dye deposition and molecular orientation within the films. Later, Hong, et al.[28] investigated the aggregation of bolaform amphiphiles and its impact on LbL deposition. They used UV-vis spectroscopy and spectroscopic ellipsometry to monitor film growth and the orientation of the dyes deposited. While the amount of material deposited was found to depend upon solution ionic strength (and hence the nature of the aggregates formed), no clear trend in dye orientation was observed. While these and other studies provide a good initial view of the influence of aggregation on dye/PE ESA, only a limited number of systems have been studied to date and knowledge in this area remains incomplete. For example, the role played by precursor aggregation in governing overall film morphology and in-plane dye organization have been largely unexplored in the range of available materials.

Previously, we have demonstrated ESA of an amphiphilic perylene diimide (PDI) with an oppositely charged PE.[21] It was observed that this unique material was efficiently deposited, even though individual dye molecules carried only a single

charge.[16] Interestingly, the materials formed were found to be comprised of serpentine nanofibers, rather than the usual planar layers. It was concluded that nanofiber formation resulted from the assembly of preformed rod-like PDI aggregates that were present in the precursor solution. Polarized fluorescence images showed that the dye molecules were oriented in the film plane, with their long axes perpendicular to the long axis of the nanofibers, but no evidence for macroscopic alignment of the nanofibers and component dyes was observed.

The possibility that macroscopic in-plane alignment can occur in ESA materials was demonstrated in earlier work by Cooper and coworkers.[15] In their studies, Congo Red and copper phthalocyanine dyes deposited in an LbL fashion with poly(lysine) were found to yield microscopic birefringent regions and a nonzero order parameter, S,[15] in bulk absorbance dichroism experiments, indicating the dyes were modestly oriented parallel and perpendicular, respectively, to the dipping direction. While no discussion of the possible orientation mechanisms was given, it very likely resulted as a simple consequence of dip coating. More recently, Lavrentovich and coworkers[21,32] have reported the preparation of macroscopically-aligned ESA films, using a lyotropic chromonic liquid crystalline dye that is structurally similar to the PDI molecules mentioned above. These researchers employed both optical imaging[31] and X-ray photoelectron spectroscopy[32] to characterize film order. Macroscopic alignment in these samples was induced by mechanically rubbing the films.

In this chapter we employ three different charged PDI dyes and oppositely charged PEs for ESA of three different PDI/PE thin films. A singly charged dye, C_7OPDI^+, and two doubly charged dyes, $PDISO_3^{2-}$ and $TAPDI^{2+}$ are employed along with $PDDA^+$ and PA^- as the polycation and polyanion, respectively. Figure 4.1 shows the chemical structures of the dyes and PEs.

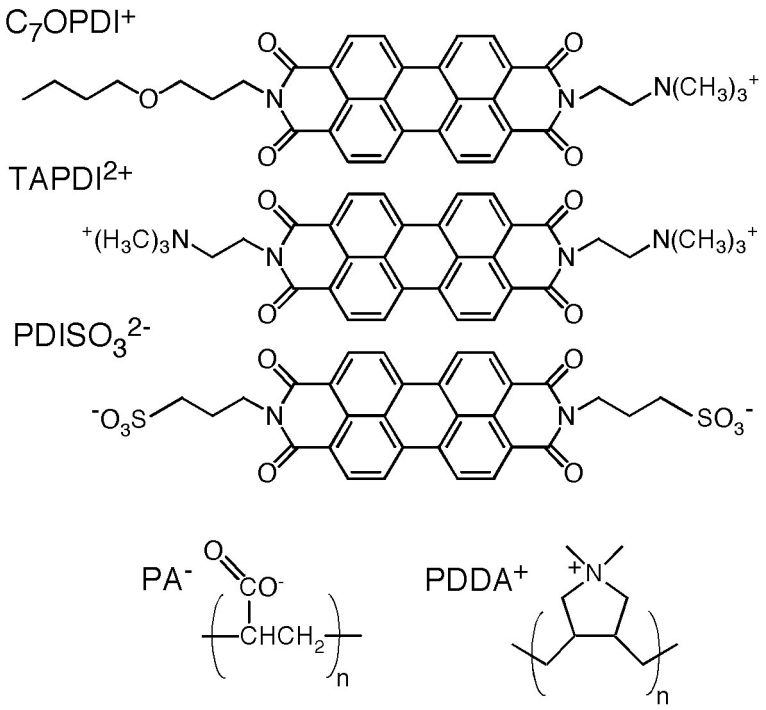

Figure 4.1 Structures for C_7OPDI^+, $TAPDI^{2+}$, $PDISO_3^{2-}$, PA^- & $PDDA^+$

The dyes were chosen specifically as a means to investigate the role played by dye aggregation in governing materials deposition, film morphology and in-plane molecular organization. Aqueous solutions of all three dyes were found to be optically clear and isotropic throughout the range of concentrations employed (up to ~250 μM). UV-vis absorbance and fluorescence spectroscopy were used to detect aggregation of the three dyes in their respective precursor solutions. The results show that C_7OPDI^+ is the most heavily aggregated of the three dyes. UV-vis absorbance studies of film growth demonstrate that C_7OPDI^+ is also the most efficiently deposited. Absorbance dichroism studies performed on the same films show that the C_7OPDI^+ molecules are macroscopically aligned perpendicular to the dipping direction, while similar materials prepared using the other two dyes exhibit no evidence for macroscopic alignment. Atomic force microscopy (AFM) images show that while all three films incorporate serpentine dye/PE nanofibers, only C_7OPDI^+/PA^- films exhibit clear evidence for 'nematic-like' nanofiber organization, with the nanofibers aligned along the dipping direction. It is concluded that relatively large, rod-like aggregates formed by C_7OPDI^+ in

the precursor solution are aligned during deposition by draining of the solution from the substrate, leading to the growth of materials exhibiting macroscopic in-plane order.

Experimental Section

Preparation of Precursor Solutions

Perylene diimide dyes (PDIs) were synthesized using previously reported procedures. The chemical structures of these dyes are shown in Figure 4.1. Solutions of N,N'-bis(2-(trimethylammonio)ethyl)-perylene-3,4,9,10-tetracarboxylic diimide ($TAPDI^{2+}$) and N-(3-(butoxypropyl)-N'-(2-(trimethylammonio)ethyl)-perylene-3,4,9,10-tetracarboxylic diimide (C_7OPDI^{+}) were prepared by first dissolving each dye in methanol. Water (18 MΩ•cm) was subsequently added to yield 1:1 water:methanol mixtures. These solutions were then heated to drive off the alcohol. Water was added a second time and heating of the solution was continued to ensure complete removal of the alcohol. Afterwards, the solutions were allowed to cool and subsequently diluted to volume with water. Solutions of N,N'-bis(3-sulfonatopropyl)perylene-3,4,9,10-tetracarboxylic diimide ($PDISO_3^{2-}$) were prepared by directly dissolving the solid into 18 MΩ•cm water.

Poly(diallyldimethylammonium) ($PDDA^{+}$) chloride (MW = 100,000-200,000 g/mol) and poly(acrylate) (PA^{-}), sodium salt (M_W = 5100 g/mol), were used as the polyelectrolytes (PEs, Mw values are as reported by the supplier). Their chemical structures are shown in Figure 4.1. They were obtained from Aldrich as an aqueous solution and as a solid, respectively, and were used without further purification. Solutions for use in thin film deposition were prepared by diluting aqueous PE stock solutions with 0.1 M, pH 7 phosphate buffer.

Deposition of Composite Films

The procedure used for deposition of PDI/PE composite films has been described previously,[21] and involves dipping a glass substrate sequentially into 1) an aqueous solution of the cationic precursor, 2) a rinse solution (18 MΩ•cm water), 3) an aqueous solution of the anionic precursor and 4) a second rinse solution. The substrate was held in each precursor solution for 60 s and in each rinse solution for 30 s. This four-step

process produces one bilayer and may be repeated any number of times to obtain a film of the desired optical density and thickness. To aid in reproducibility, the dip-coating procedure was automated using a home built dip coater that was controlled by Labview software written in-house. The insertion and extraction rate for all samples was set to 1.8 mm/s.

Sample Characterization

Thin-film and bulk solution phase UV-vis absorbance data were collected using a HP 8453 diode array spectrometer. A clean glass coverslip was used as the reference in all thin-film absorbance experiments. Thin film dichroism data were obtained by inserting a sheet polarizer just prior to the sample in the optical path of this instrument. Fluorescence spectra of the precursor solutions were acquired using a SPEX Fluoromax-2 fluorimeter. Temperature dependent fluorescence spectra were obtained with a temperature controlled sample holder that allowed the temperature to be set and maintained with ±1 ^{o}C precision. Filtration studies were carried out by passing the PDI precursor solutions through 0.45 μm teflon and 0.8 μm cellulose acetate syringe filters. Solution absorbance spectra were recorded both before and after filtration. The morphology of the PDI/PE composite films was visualized using a Digital Instruments Multimode atomic force microscopy (AFM, Veeco Metrology). All AFM images were recorded in tapping mode, under an atmosphere of dry nitrogen. Image analysis was performed using the Image SXM software (NIH Image).

Results

Aggregation in Perylene-Diimide Precursor Solutions

The level and strength of PDI aggregation in both dilute aqueous solution and in the solutions used for film deposition were investigated in a number of different experiments. Figure 4.2A plots absorbance spectra obtained from all three dyes at ~ 250 μM concentrations in aqueous solution (2 mm pathlength). Similar spectra were also obtained in aqueous solution at ~ 10 μM concentrations (not shown). For comparison purposes, Figure 4.2B plots the normalized absorbance spectra obtained from ~ 10 μM methanolic solutions of the same dyes. The spectra obtained in methanol are

predominantly those of the monomeric dyes, although some evidence for aggregation is also present in these spectra. The dramatic differences observed between the spectra recorded in aqueous and methanolic solutions indicate that all three dyes are strongly aggregated in aqueous solution. Furthermore, the aqueous spectra show that the three dyes are likely aggregated to different extents and/or form aggregates of different structures. The latter conclusion is drawn from the differences in spectral shapes and peak absorbance values observed for the three dyes. From these results, it is concluded that $TAPDI^{2+}$ is least aggregated, while $PDISO_3^{2-}$ is more strongly aggregated and C_7OPDI^{+} is most heavily aggregated.

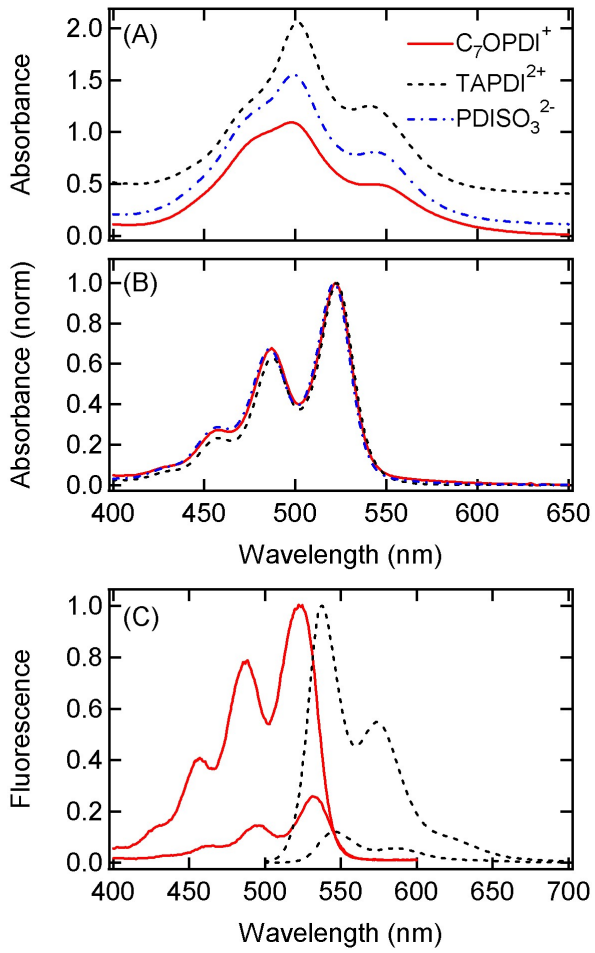

Figure 4.2 (A) Absorption spectra of $TAPDI^{2+}$, $PDISO_3^{2-}$, and C_7OPDI^{+} in aqueous solution at concentration of 250, 262, and 267 μM, respectively, recorded in a 2 mm pathlength cuvette. $TAPDI^{2+}$ and $PDISO_3^{2-}$ spectra have been offset by 0.4, and 0.1 absorbance units, respectively. (B) Normalized absorption spectra of 10 μM

methanolic solutions of the same three dyes. (C) Normalized fluorescence excitation (solid lines) and emission (dashed lines) spectra obtained from 10 μM methanolic (upper curves) and aqueous (lower curves) solutions of $TAPDI^{2+}$

Figure 4.2C plots representative fluorescence excitation and emission spectra obtained from $TAPDI^{2+}$ in dilute (~ 10 μM) methanolic and aqueous solutions. Similar excitation and emission spectra were also obtained from C_7OPDI^{+} and $PDISO_3^{2-}$. The distinct differences observed in the absorption (Figure 4.2A) and fluorescence excitation spectra indicate that nonfluorescent aggregates dominate the absorption spectra in each case, while the fluorescence is dominated by excitation and emission of monomer-like species.

To further assess the relative strengths of aggregation for each of the dyes, fluorescence spectra of their dilute aqueous solutions were also recorded as a function of temperature. These data demonstrate that the emission from each dye increases monotonically with increasing solution temperature. This observation is consistent with the temperature-dependent dissociation of monomer-like species from the aggregates and may be modeled by the following equilibrium process:

$$PDI_n \longleftrightarrow PDI_{n-1} + PDI^*$$

Here, PDI_n represents a PDI aggregate comprised of n monomers, while PDI* designates a fluorescent monomer-like species. Assuming the nonfluorescent aggregates are present in relatively high (and approximately constant) concentrations, the fluorescence intensity is directly proportional to the dissociation constant. Thus, Van't Hoff plots may then be constructed from the fluorescence and absolute temperature data. These plots are shown in Figure 4.3

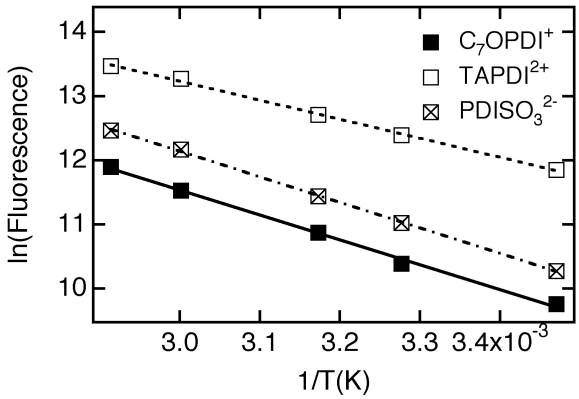

Figure 4.3 Van't Hoff plots depicting the natural log of the fluorescence intensity obtained from 10 μM aqueous solutions of each dye as a function of 1/T(K). The fluorescence intensity is proportional to the equilibrium constant for the process shown in equation 1. Data shown represent the average values obtained from three replicate measurements.

and provide a measure of the relative aggregation strengths for each dye, as reflected by their associated equilibrium constants. The equilibrium constant for dissociation is found to be largest for $TAPDI^{2+}$, smaller for $PDISO_3^{2-}$ and smallest for C_7OPDI^+. It is therefore concluded that C_7OPDI^+ is most strongly aggregated, while $TAPDI^{2+}$ is most weakly aggregated at room temperature. It is also noteworthy that the three Van't Hoff plots all have similar slopes, but are shifted vertically from each other. This observation suggests that the differences in aggregation strength likely result from entropic factors associated with solvation of the monomer-like species.

Aggregate size was found to correlate with aggregation strength. Relative aggregate size was assessed by passing high concentration (~ 250 μM) aqueous PDI solutions through filters of different porosity (0.45 μm teflon filter and 0.8 μm cellulose acetate filters were employed) and comparing the absorbance spectra obtained before and after filtration. The absorbance of the 0.4 μm filtered C_7OPDI^+ solution decreased appreciably (by 89%) after filtration, while the $TAPDI^{2+}$ solution absorbance decreased by only 1% and that of $PDISO_3^{2-}$ increased by 1%. The absorbance decreased by only 11% for C_7OPDI^+ when passed through the 0.8 μm filter, while $TAPDI^{2+}$ and $PDISO_3^{2-}$ absorbance values decreased by 2% and 1%, respectively. The values obtained for $TAPDI^{2+}$ and $PDISO_3^{2-}$ in both cases are near the estimated experimental error. These

results conclusively demonstrate that C_7OPDI^+ forms larger aggregates in aqueous solution than the other two PDIs.

Sequential Deposition of Perylene-Diimide/Polyelectrolyte Composites

The impact of precursor aggregation on ESA of the three perylene-diimide/polyelectrolyte (PDI/PE) composites was initially assessed by UV-vis absorbance studies of their respective thin films. ESA films were all prepared as previously described, using a sequential dip-coating procedure that is functionally equivalent to LbL deposition. Previous studies describing the sequential deposition of related materials have shown that precursor concentration and the ionic strength and pH of the precursor solutions are all important in determining the rate of materials deposition.[15,25-28] The impacts of these parameters were explored in preparation of the present samples. After extensive experimentation, it was concluded that deposition of the PDIs from otherwise pure aqueous solution and PEs from 0.1 M phosphate buffer (pH = 7) produced the best results. PDI and PE concentrations of ~ 250 μM and ~ 3 mM (monomer), respectively were found to yield efficient deposition while largely avoiding PDI precipitation in bulk solution. These conditions were employed throughout the studies described below.

Normalized UV-vis absorption spectra obtained from thin films of all three PDI/PE composites are shown in Figure 4.4A. All yielded qualitatively similar spectra that are distinctly different from those of the monomeric dyes (compare Figure 4.2 and Figure 4.4A). The differences observed between the thin-film and solution-phase spectra prove that all three dyes are heavily aggregated in their respective films. Both red- and blue-shifted (relative to the monomer) absorption peaks are found in these spectra. The appearance of these peaks could be due to polymorphism in the aggregate structures or they could reflect the appearance of different electronic transitions in the aggregates.[35,36]

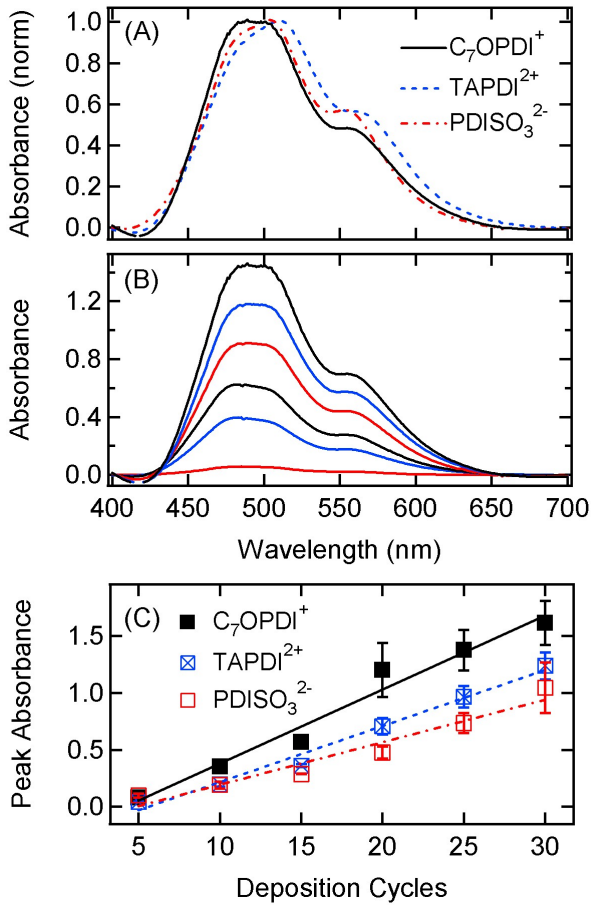

Figure 4.4 (A) Absorbance spectra (normalized) obtained from 30 bilayer films of C_7OPDI^+/PA^-, $TAPDI^{2+}/PA^-$, and $PDISO_3^{2-}/PDDA^+$. (B) Representative absorbance spectra obtained from C_7OPDI^+/PA^- composite films incorporating, in order of increasing absorbance, 5, 10, 15, 20, 25, and 30 bilayers. (C) Peak absorbance of all three composited as a function of the number of deposition cycles. Results depict the average of three experiments. Error bars depict the 80% confidence intervals.

Absorption spectra obtained from the three composite films are also different from the solution phase spectra of the aggregated precursors (compare Figure 4.2A and Figure 4.4A). It is noteworthy that the composite film spectra are qualitatively most similar to the aqueous C_7OPDI^+ spectrum (the most heavily aggregated of the three), suggesting that complexation to the PE results in much tighter packing of all PDI chromophores. Subtle differences in the absorption spectra obtained from the three composite films are also apparent (see Figure 4.4A). The C_7OPDI^+/PA^- film absorbs

broadly around a peak at 493 nm, while the $TAPDI^{2+}/PA^{-}$ and $PDISO_3^{2-}/PDDA^{+}$ composites exhibit somewhat sharper, red-shifted absorption peaks at 510 and 503 nm, respectively. The latter two composites also possess relatively more pronounced shoulders on the red edge of their spectra. These results indicate that the aggregates formed by the three composites are somewhat different, as will be addressed further, below. However, the overall similarities in the film spectra suggest that film absorbance should be useful as a means to track and compare the quantities of dye incorporated in each of the films.

Absorbance spectra were obtained as a function of the number of deposition cycles employed (i.e. bilayers deposited) in preparation of each composite film. These data were used as a means to uncover any changes that might occur in aggregate structure as the films thicken. Again, all three composites were deposited under similar conditions (i.e., PDI concentrations of ~ 250 μM and PE monomer concentrations of 3 mM in 0.1 M, pH 7 phosphate buffer). Figure 4.4B plots representative absorbance spectra obtained from C_7OPDI^{+}/PA^{-} thin films against the number of deposition cycles. As is readily apparent, only very subtle changes appear in the spectra over the range studied, indicating aggregate structure changes little as the film grows. The other two composites yielded similar results.

The peak absorbance value was also obtained from the above spectra and used as a measure of the amount of PDI incorporated into each film. These values are plotted in Figure 4.4C for each of the three composites. The data shown depict the average values obtained from three replicate experiments on three sets of samples. All three composite films exhibit an approximately linear increase in absorbance with increasing deposition cycles. Appended to Figure 4.4C are lines fitted to each data set to better depict the trends observed. While all three show a linear increase in absorbance for five or more bilayers, they reflect only a very small increase over the first few (approximately four) deposition cycles, indicating that the rate of composite formation is initially much lower. The use of a primer layer may enhance the deposition rate in these earlier cycles,[15] but no such layer was employed here. Nevertheless, the results for five or more bilayers show that these materials can be efficiently and reproducibly deposited by sequential deposition methods.

It is most noteworthy from the data shown in Figure 4.4C that the three composites exhibit different PDI deposition rates, as manifested by the different slopes found in each of the film absorbance plots. Again, all PDIs and PEs were present in the precursor solutions at nearly identical concentrations. The data show that C_7OPDI^+ deposits at the greatest rate, followed by $TAPDI^{2+}$, with $PDISO_3^{2-}$ deposited least efficiently. PDI deposition was also strongly correlated with the presence of larger aggregates in the precursor solutions. For example, a C_7OPDI^+ solution that had been passed through a 0.45 μm filter yielded a dramatically reduced deposition rate.

Film Morphology

In spite of the differences in PDI precursor aggregation and film deposition efficiencies discussed above, the composite films produced were all remarkably similar in morphology. Topographic images recorded by tapping mode AFM were used to investigate film morphology in each case. Figure 4.5 depicts representative results obtained for the three composites. These images were acquired from films incorporating 10 and 30 bilayers. Films incorporating relatively few bilayers (i.e., < 15) were all found to be comprised of serpentine nanofibers. We have previously shown in studies of related composites that formation of these nanofibers requires both PDI and PE.[21] It was concluded that the nanofibers were produced by complexation of small, preformed, rod-like PDI aggregates with the PE. Taken together, the evidence for aggregation of all three PDIs, and the formation of the same serpentine nanofibers in all three composites suggests this same mechanism is active here.

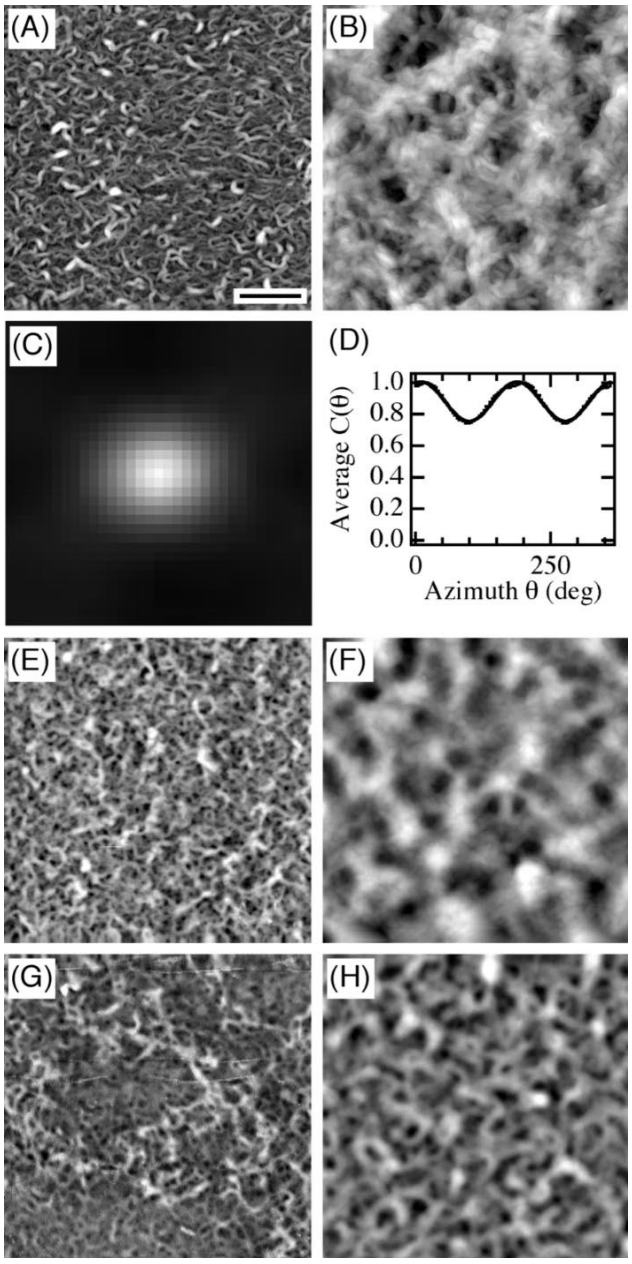

Figure 4.5 AFM images of (A, B) C_7OPDI^+/PA^-, (E, F) $TAPDI^{2+}/PA^-$, and (G, H) $PDISO_3^{2-}/PDDA^+$ composite thin films. Also shown are image autocorrelation data (C) and the normalized average azimuthal correlation coefficient, C(θ) (D), derived from the image shown in (A). (A), (E), and (G) depict films comprised of 10 bilayers, while (B), (F), and (H) depict films comprised of 30 bilayers. Full grayscales values in (A, B) and (E-H) depict height variations of 104, 608, 41, 176, 85, and 202 nm, respectively. Scale bar is 2 μm in length.

Film morphology was observed to change as the number of deposition cycles employed increased (see Figure 4.5). Specifically, the nanofiber morphology changed from films of continuous nanofibers to films incorporating large round or oblong protruding structures that appeared to grow on top of nanofibrous underlayers. Simultaneously, the films got noticeably rougher. Increased film roughness is reflected in the increased range of topographic heights for the 30 bilayer films depicted in Figure 4.5.

Nanofiber Alignment – Dichroism Studies

While overall film morphology was found to be similar for all three composites, important differences were observed in the macroscopic alignment of nanofibers comprising the films. Specifically, the C_7OPDI^+/PA^- composites were found to produce partially aligned nanofibers, while the other two composites yielded no clear evidence for such organization. It is important to note that, unlike in previous studies,[31,32] all composites produced were obtained from dilute (~ 250 μM), optically clear and isotropic dye solutions.

Evidence for nanofiber alignment (or lack thereof) was obtained from both bulk UV-vis dichroism measurements and by AFM imaging. In the former, the absorbance of each film was measured using light polarized parallel and perpendicular to the dipping direction (i.e., $A_{\parallel}$ and $A_{\perp}$). The dipping direction in these experiments was aligned to within $\pm 5^{o}$ of the incident polarization. The dichroism was determined from these measurements as follows:

$$D = \frac{A_{\parallel} - A_{\perp}}{A_{\parallel} + A_{\perp}}$$

Equation 1: Dichroism formula relating polarized absorbance to molecular order.

Dichroism data obtained from the C_7OPDI^+/PA^- and $PDISO_3^{2-}/PDDA^+$ complexes are plotted in Figure 4.6 as a function of the number of dipping cycles employed. The $TAPDI^{2+}/PA^-$ complexes yielded dichroism data (not shown) that were statistically indistinguishable from the $PDISO_3^{2-}/PDDA^+$ results. The data shown (Figure 4.6) depict

the average values obtained from three replicate measurements, while the error bars give the estimated 80% confidence intervals.

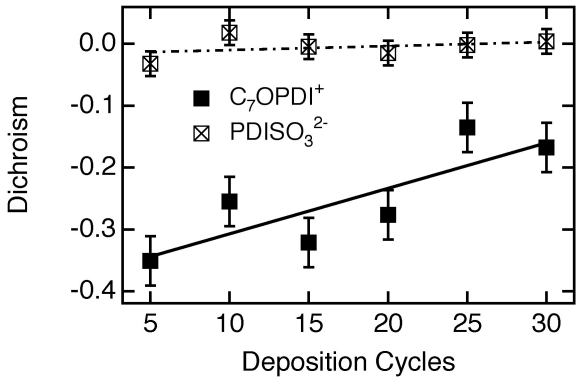

Figure 4.6 Absorption dichroism data obtained for C_7OPDI^+/PA^- and $PDISO_3^{2-}/PDDA^+$ composites as a function fo number of bilayers deposited. Data points depict the mean value obtained from three replicate measurements. Error bars depict the estimated 80% confidence intervals. Lines plotted through the data are meant only to highlight the trends exhibited in the data.

As shown in Figure 4.6, the C_7OPDI^+/PA^- composites all yielded dichroism values that were significantly smaller than zero. It is known that the lowest energy electronic transition in these PDIs is polarized along the long axis of the chromophore.[35,37,38] Therefore, the negative dichroism values obtained indicate that the chromophores tend to align perpendicular to the dipping direction, in the plane of the sample. At its greatest (5 bilayers), a dichroism value of ~ –0.35±0.06 was measured. A value of -1.0 would indicate perfect order, with all chromophores aligned perpendicular to the dipping direction, while a value of +1.0 would indicate perfect parallel alignment. In contrast to the results obtained from the C_7OPDI^+/PA^- films, results from the other two composites prove that, on average, their chromophores were significantly more disordered. The $TAPDI^{2+}/PA^-$ and $PDISO_3^{2-}/PDDA^+$ composites yielding average dichroism values of 0.02±0.06 and 0.00±0.02, respectively.

The in-plane ordering of dyes in different dye/PE composites prepared by simple dip-coating procedures has been observed previously by Cooper, et al.[15] Their results yielded smaller dichroism values of ~ -0.04 for a perpendicularly-aligned dye.

Unfortunately, they did not explore the mechanism of alignment in detail; nor did they explore methods for enhancing the order observed. Lavrentovich, et al., have also produced aligned Dye/PE composites by sequential deposition methods.[31,32] Alignment in these materials was induced by shearing the films, resulting in dichroism values of ~ -0.67. Taken together, these prior results and the present results obtained from aligned C_7OPDI^+/PA^- composites suggest the chromophores in these composites are reasonably well ordered.

Interestingly, the data presented in Figure 4.6 also show that the most highly ordered films are obtained in only the first few deposition cycles. As the number of deposition cycles is increased, the dye molecules incorporated into the films become more disordered, as reflected in the trend of the dichroism data towards zero. Future studies will explore alternative methods for further enhancing the observed alignment.

Nanofiber Alignment – AFM Imaging Studies

Topographic images obtained by tapping mode AFM provide a complementary view of order in the PDI/PE composite films. While AFM provides no direct information on chromophore alignment in the present studies, it does allow for local alignment of the nanofibers to be directly visualized. Nanofiber alignment is evidenced in the AFM images of the ten-bilayer C_7OPDI^+/PA^- film shown in Figure 4.5. Alignment in this case is reflected by the predominant orientation of the nanofibers along the horizontal direction, lending a 'nematic-like' appearance to the films. In contrast, images of the other two composites show no such organization. This general trend towards 'nematic-like' order in the C_7OPDI^+/PA^- films and disorder in the other two composites was observed in many different images of several different samples.

These experiments were also carefully repeated to prove that nanofiber alignment is predominantly along the dipping direction in the C_7OPDI^+/PA^- films. Figure 4.7 shows representative examples of the images obtained. The dipping direction in each is aligned to within $\pm 5^o$ of vertical on these images. Again, 'nematic-like' order is observed with predominant nanofiber alignment occurring along the vertical direction, especially for the thinner film. As is consistent with the dichroism data presented above, organization in the thicker film is less apparent.

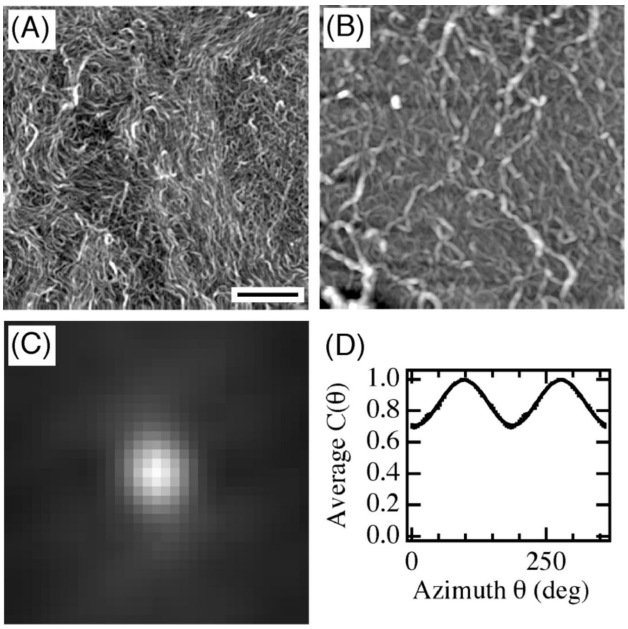

Figure 4.7 AFM images of (A) 10 bilayer and (B) 20 bilayer C_7OPDI^+/PA^- composite thin films. Also shown are image autocorrelation data (C) and normalized average azimuthal correlation coefficient, C(θ) (D), derived from the image shown in (A). The dipping direction in these two images are within ±5° of vertical. Full grayscales in (A) and (B) depict height variations of 44 and 350 nm, respectively. Scale bar is 2 μm in length.

Quantitative assessment of nanofiber alignment in the images shown in Figure 4.5 and Figure 4.7 is made difficult by the serpentine appearance and variable lengths of the nanofibers. Future work will include development of automated image analysis procedures[39] for making quantitative measurements of fiber alignment and persistence lengths. In the present study, autocorrelation methods were used to provide a simple and semiquantitive view of nanofiber order. For this purpose, the two dimensional autocorrelation of each image was first calculated. Figure 4.5C depicts a representative example derived from the image in Figure 4.5A. Only the central portion of the autocorrelation function is useful, due to insufficient averaging for the larger features that dominate the autocorrelation data in outer regions. Therefore, only the central 33 X 33 pixel region of each autocorrelation was employed (see Figure 4.5C). The average correlation coefficient was calculated as a function of azimuthal angle about the center of each of the autocorrelations. Figure 4.5D shows normalized average correlation

coefficient data obtained from Figure 4.5C. Similar data are shown in Figure 4.7C, D for the image shown in Figure 4.7A. These data were fit to a cosine-squared function (empirical) in order to determine both the amplitude and phase of the azimuthal variations in each case. The latter provides quantitative data on the average fiber alignment direction while the former yield semiquantitative results on the degree of alignment (i.e. larger amplitudes correspond to greater order). Each peak and valley in the autocorrelation data indicates the presence of longer and shorter features, respectively, oriented along those azimuthal directions. This analysis was only performed on images of samples incorporating 10 PDI/PE bilayers as noise due to insufficient averaging appeared to be a limitation in materials incorporating larger features.

The peak-to-peak amplitudes and phase angles (i.e., alignment directions) obtained by analysis of the images shown in Figure 4.5A, E and G and Figure 4.7A are given in Table 1.

Table 1 Image analysis summery. The amplitude gives a semi-quantitative measure of nanofiber order, and the phase angle a measure of the average alignment direction. A phase angle of 0° corresponds to horizontal alignment on the AFM images.

Figure:Composite	Amplitude (peak—peak)	Phase (deg)
Figure 4.5A: C_7OPDI^{+}/PA^{-}	0.250 ± 0.004	-10 ± 1
Figure 4.5E: $TAPDI^{2+}/PA^{-}$	0.117 ± 0.003	95 ± 1
Figure 4.5G: $PDISO_3^{2-}$ /PDDA+	0.104 ± 0.002	61 ± 1
Figure 4.7A: C_7OPDI^{+}/PA^{-}	0.288 ± 0.004	83 ± 1

The results are consistent with nanofiber alignment along the horizontal direction in Figure 4.5A, and vertical alignment in Figure 4.7. The weak alignment implied by the

results obtained from Figure 4.5E, G are believed to result from insufficient averaging of truly random features in these images. Random alignment in these materials is evidenced by the UV-vis dichroism data discussed above.

Discussion

The data presented above show that all three dyes were strongly aggregated in the aqueous precursor solutions employed for PDI/PE deposition. $TAPDI^{2+}$ was found to be most weakly aggregated, with $PDISO_3^{2-}$ more strongly aggregated and C_7OPDI^{+} most strongly aggregated. Aggregate size was also found to correlate with aggregation strength, with C_7OPDI^{+} forming the largest aggregates in solution. Thin films of all three PDIs could be produced by sequential deposition with oppositely charged PEs. However, at approximately equal concentrations, C_7OPDI^{+} was found to be most efficiently deposited, while $TAPDI^{2+}$ was deposited at a lower rate and $PDISO_3^{2-}$ was least efficiently deposited. All three composite films were found to exhibit similar morphologies, incorporating serpentine PDI/PE nanofibers. However, it was shown that C_7OPDI^{+} was deposited in PDI/PE composite films in an aligned state, while $TAPDI^{2+}$ and $PDISO_3^{2-}$ produced much more disordered films. The serpentine nanofibers found in C_7OPDI^{+}/PA^{-} films were also observed to align with 'nematic-like' order along the dipping direction.

The above observations provide strong supporting evidence for our previously-reported model of PDI/PE film growth.[21] Specifically, these materials are believed to grow by complexation of small, preformed rod-like aggregates found in the PDI precursor solutions with strands of oppositely charged PE. They are subsequently bound together like links in a chain by further deposition of PE and PDI in subsequent cycles. The observations presented above show that the level of dye aggregation, among other factors, plays a very important role in governing the deposition efficiency of each dye within the PDI/PE composite films. Taken together, the dramatic differences in molecular weight for PA^{-} and $PDDA^{+}$ and the similar film morphologies observed in all cases suggest that PE chain length and dynamics are of lesser importance in governing film properties. The specific impacts of PE properties on PDI/PE composite formation will be explored in future studies.

While strong aggregation correlates well with efficient deposition in the case of C_7OPDI^+, the other two dyes do not follow this trend, with $TAPDI^{2+}$ depositing more rapidly than the more heavily aggregated $PDISO_3^{2-}$. Here, this observation is attributed to differences in the strengths of the interactions between these dyes and their associated PEs. $PDISO_3^{2-}$ clearly binds more weakly to $PDDA^+$ than the other two bind to PA^-. As supporting evidence of this conclusion, it is noteworthy that the rinse solution following $PDISO_3^{2-}$ deposition exhibited a light red color for 20 or more dipping cycles, while for the other two PDIs, the rinse solution color was significantly less intense. Furthermore, this effect does not appear to result from differences in the PE, since the $PDDA^+$ used had a much larger molecular weight than PA^-. Weaker PDI/PE interactions in this case are believed to result from delocalization of the negative charge on the sulfonate groups of $PDISO_3^{2-}$, preventing strong interactions with the PE. This also reduces electrostatic repulsion between $PDISO_3^{2-}$ species, allowing them to aggregate more strongly than $TAPDI^{2+}$.

Macroscopic in-plane alignment of the chromophores in the C_7OPDI^+/PA^- composites may also be explained by our model for nanofiber growth. Such alignment appears to depend entirely on the nature of the PDI precursor aggregates, with the most heavily aggregated precursor (C_7OPDI^+) yielding aligned materials. The lack of alignment observed in $TAPDI^{2+}/PA^-$ composites suggests alignment is determined primarily by the properties of the dye, while the PE is of lesser importance. It is believed that the rod-like aggregates formed in the former are sufficiently long that they can be aligned by solution flow during deposition (i.e. by the solution draining from the substrate) from dilute isotropic aqueous solutions. Such alignment should occur parallel to the dipping direction, exactly as is observed in the experimental data. In contrast to C_7OPDI^+, the other two PDIs are believed to deposit from much shorter aggregates that are not well aligned. Figure 4.8 presents a pictorial view of this

model.

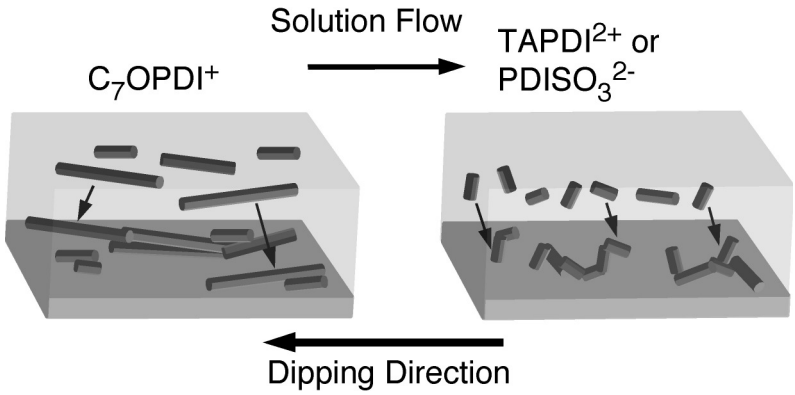

Figure 4.8 Model for flow-induced deposition of aligned nanofibrous materials in the case of C_7OPDI^+/PA^- composites and deposition of disordered materials for the cases of $TAPDI^{2+}/PA^-$ and $PDISO_3^{2-}/PDDA^+$. The model shows the deposition of preformed PDI aggregates, and the presence of PE in the films is implied.

Once again, it should be noted that C_7OPDI^+ dichroism (and in-plane alignment) decrease with increasing deposition cycles (see Figure 4.6). This contrasts with previous studies by Lavrentovich, et al, for shear-aligned films, in which an increase in order for up to several bilayers was observed. The present result may be taken as further evidence for the role played by solution flow in governing alignment. In the very early phases of film growth, the solution flow should be substantially uniform and lamellar, allowing for alignment of the aggregates along the dipping direction. As the serpentine fibers grow in size and the film surface roughens, the flow of liquid draining from the slide will become more turbulent, resulting in a more disordered deposition of aggregates.

Conclusion

In summary, it has been shown that aggregation of the precursor species in PDI/PE composites prepared by ESA methods plays an important role in governing the rate of materials deposition, the morphology of the films obtained, and in some cases may lead to the growth of macroscopically-aligned materials, exhibiting in-plane organization of the dye. While such organization has been observed previously in liquid crystalline materials that have been purposefully aligned by mechanical means,[31,32] it has seldom been reported to occur in more conventional ESA materials.[15] The present studies provide strong evidence that alignment in materials deposited by dip coating can arise from flow-induced orientation of preformed aggregates found in the precursor solutions.

It is believed this represents a general mechanism that could be used for alignment of a wide range of materials. The films obtained are certain to find important applications in organic optical and electronic devices that require such organization.[40] Importantly, alignment in this case is achieved as a consequence of the deposition method employed and requires no additional steps, thereby simplifying materials preparation.

REFERENCES

(1) Ariga, K.; Hill, J. P.; Ji, Q. Phys. *Chem. Chem. Phys*. **2007**, 9, 2319-2340.

(2) Hammond, P.T. *Adv. Mater.* **2004**, 16, 1271-1293

(3) Decher, G. *Science* **1997**, 277, 1232-1237.

(4) Berndt, P.; Kurihara, K.; Kunitake, T. *Langmuir* **1992**, 8, 2486-2490.

(5) Schlenoff, J. B.; Ly, H.; Li, M. *J. Am. Chem. Soc.* **1998**, 120, 7626-7634.

(6) Decher, G.; Lvov, Y.; Schmitt, J. *Thin Solid Films* **1994**, 244, 772-777.

(7) Decher, G.; Hong, J. D. Ber. Bunsenges. *Phys. Chem.* **1991**, 95, 1430.

(8) Decher, G.; Hong, J. D.; Schmitt, J. *Thin Solid Films* **1992**, 210/211, 831-835.

(9) Ferreira, M.; Cheung, J. H.; Rubner, M. F. *Thin Solid Films* **1994**, 244, 806-809.

(10) Ferreira, M.; Rubner, M. F. *Macromol.* **1995**, 28, 7107-7114.

(11) Zhang, X.; Gao, M.; Kong, X.; Sun, Y.; Shen, J. *J. Chem. Soc. Chem. Commun.* **1994**, 1055-1056.

(12) Araki, K.; Wagner, M. J.; Wrighton, M. S. *Langmuir* **1996**, 12, 5393-5398.

(13) Tang, T.; Qu, J.; Mullen, K.; Webber, S. E. *Langmuir* **2006**, 22, 26-28.

(14) Doherty, W. J.; Friedlein, R.; Salaneck, W. R. *J. Phys. Chem. C* **2007**, 111, 2724-2729.

(15) Cooper, T. M.; Campbell, A. L.; Crane, R. L. *Langmuir* **1995**, 11, 2713-2718.

(16) Yoo, D.; Lee, J.-K.; Rubner, M. F. *Mat. Res. Soc. Symp. Proc.* **1996**, 413, 395-399.

(17) Yoo, D.; Wu, A.; Lee, J.-K.; Rubner, M. F. *Synth. Metals* **1997**, 85, 1425-1426.

(18) Ariga, K.; Lvov, Y.; Kunitake, T. *J. Am. Chem. Soc.* **1997**, 119, 2224-2231.

(19) Chang-Yen, D. A.; Lvov, Y.; McShane, M. J.; Gale, B. K. *Sensors and Actuators B* **2002**, 87, 336-345.

(20) Bradley, M. S.; Tischler, J. R.; Bulovic, V. *Adv. Mater*. **2005**, 17, 1881-1886.

(21) Everett, T. A.; Twite, A. A.; Xie, A.; Battina, S. K.; Hua, D. H.; Higgins, D. A. *Chem. Mater*. **2006**, 18, 5937-5943.

(22) Lee, J.-K.; Yoo, D. S.; Handy, E. S.; Rubner, M. F. *Appl. Phys. Lett.* **1996**, 69, 1686-1688.

(23) Durstock, M. F.; Spry, R. J.; Baur, J. W.; Taylor, B. E.; Chiang, L. Y. J. *Appl. Phys.* **2003**, 94, 3253-3259.

(24) Clark, S. L.; Handy, E. S.; Rubner, M. F.; Hammond, P. T. *Adv. Mater.* **1999**, 11, 1031-1035.

(25) Lvov, Y.; Decher, G.; Möhwald, H. *Langmuir* **1993**, 9, 481-486.

(26) Yoo, D.; Shiratori, S. S.; Rubner, M. F. *Macromol.* **1998**, 21, 4309-4318.

(27) Shiratori, S. S.; Rubner, M. F. *Macromol.* **2000**, 33, 4213-4219.

(28) Hong, J.-D.; Park, E.-S.; Park, A.-L. *Langmuir* **1999**, 15, 6515-6521.

(29) Naber, A.; Fischer, U. C.; Kirchner, S.; Dziomba, T.; Kollar, G.; Chi, L. F.; Fuchs, H. *J. Phys. Chem. B* **1999**, 103, 2709-2717.

(30) Mao, G.; Tsao, Y.; Tirrell, M.; Davis, H. T.; Hessel, V.; Ringsdorf, H. *Langmuir* **1993**, 9, 3461-3470.

(31) Schneider, T.; Lavrentovich, O. D. *Langmuir* **2000**, 16, 5227-5230.

(32) Schnieder, T.; Artyushkova, K.; Fulghum, J. E.; Broadwater, L.; Smith, A.; Lavrentovich, O. D. *Langmuir* **2005**, 21, 2300-2307.

(33) Xie, A.; Liu, B.; Hall, J. E.; Barron, S. L.; Higgins, D. A. *Langmuir* **2005**, 21, 4149-4155.

(34) Ye, F.; Higgins, D. A.; Collinson, M. M. *J. Phys. Chem. C* **2007**, 111, 6772-6780.

(35) Kazmaier, P. M.; Hoffmann, R. *J. Am. Chem. Soc*. **1994**, 116, 9684-9691.

(36) Gregg, B. A.; Kose, M. E. *Chem. Mater*. **2008**, 20, 5235-5239.

(37) Adachi, M.; Murata, Y.; Nakamura, S. *J. Phys. Chem.* **1995**, 99, 14240-14246.

(38) Struijk, C. W.; Sieval, A. B.; Dakhorst, J. E. J.; van Dijk, M.; Kimkes, P.; Koehorst, R. B. M.; Donker, H.; Schaafsma, T. J.; Picken, S. J.; van de Craats, A. M.; Warman, J. M.; Zuilhof, H.; Sudhölter, E. J. R. *J. Am. Chem. Soc.* **2000**, 122, 11057-11066.

(39) Elbischger, P.J.; Bischof, H.; Regitnig, P.; Holzapfel, G.A. *Pattern Anal. Appl.* **2004**, 7, 269-284.

(40) Chen, X. L.; Lovinger, A. J.; Bao, Z.; Sapjeta, *J. Chem. Mater*. **2001**, 13, 1341-1348.

CHAPTER 5 - Electrostatic Self-Assembly of Ordered Perylene-Diimide/Polyelectrolyte Nanofibers in Fluidic Devices: from Nematic Domains to Macroscopic Alignment

Introduction

Layer-by-layer (LbL) deposition is a widely utilized, versatile process whereby functional multilayer films of tailored composition and controlled thickness can readily be prepared.[1-3] In its most common form, LbL deposition involves sequentially exposing a substrate to aqueous solutions of oppositely charged ionic precursors. Films incorporating polyelectrolyte pairs,[1,4-7] polyelectrolytes with charged small molecules,[8-15] and pairs of charged small molecules[16-19] have all been prepared.

A multitude of methods for LbL deposition have been reported in the literature. Dip-coating methods are the most common. Along with spray-coating,[20,21] dip-coating procedures can be employed to produce uniform, continuous films on substrates of arbitrary size and geometry. Although best suited to coating of planar substrates, spin-casting methods[22,23] have also been shown to be useful for preparation of large-area films. When pre-patterned substrates are employed to direct electrostatic self-assembly (ESA) of the precursors, these same methods can be used to prepare *patterned* LbL films.[24,25] Importantly, patterned films have also been produced on native, unpatterned substrates by ESA[26] within the channels of microfluidic devices.[27-31]

LbL assembly within microfluidic channels is now being used in the development of unique materials for biosensors[28,32] and electronic circuit components.[27] In early work by Lefaux and Mather, poly(styrene sulfonate) and poly(allylamine hydrochloride) were deposited in a microfluidic device to form patterned polyelectrolyte films that were otherwise similar to those obtained using more conventional LbL procedures.[27] The formation of novel polyelectrolyte/polyelectrolyte and polyelectrolyte/protein microstrips

at the confluence of microfluidic channels was reported at about the same time by Lvov and coworkers.[28] These authors demonstrated the deposition of patterned composite materials of different geometries and compositions with micrometer-scale spatial resolution. More recently, Kim et al. demonstrated patterned deposition of an azobenzene side-chain polymer with poly(diallyldimethylammonium chloride).[30] These authors found that deposition from flowing solution yielded films of reduced roughness, compared to those obtained by dip coating. They also showed that substrate exposure time is important in governing materials deposition and surface roughness. Finally, the LbL assembly of insulin monomers into amyloid fibers has also been demonstrated in fluidic devices.[33] Use of microfluidic procedures in this case facilitated studies of protein aggregation by limiting consumption of reagents.

Many of the above studies note that LbL deposition in fluidic devices may allow for films of flow-aligned composites to be produced. Unfortunately, none provide clear evidence for the assembly of patterned materials exhibiting in-plane anisotropic order. In a previous publication from our group, we demonstrated the deposition of nanofibrous perylene-diimide/polyelectrolyte (PDI/PE) composite films by sequential dip-coating procedures.[14] It was determined in these studies that nanofiber formation resulted from deposition of preformed π-stacked PDI aggregates present in the precursor solutions. The degree and strength of aggregation ultimately determined the observed film morphology. More recently, we showed that anisotropic in-plane nanofiber and chromophore alignment could be achieved in dip-coated films of similar materials.[15] Such ordering was observed for composites prepared from a singly-charged, amphiphilic PDI precursor (C_7OPDI^+) but not when symmetric, doubly-charged PDIs (e.g., $TAPDI^{2+}$) were employed. In-plane order was concluded to occur by flow-induced alignment of the aggregated PDI nanorods found in the precursor solution. Alignment has been observed previously in very few LbL systems.[8,34,35]

In this chapter, the deposition of flow-aligned ESA materials in a fluidic device is conclusively demonstrated for the first time. Specifically, ESA of patterned nanofibrous PDI/PE composite films is reported. The results obtained serve to expand upon the knowledge gained in our earlier studies of PDI/PE self-assembly.[14,15] Structures of the PDIs and PE employed in the present investigations are shown in Figure 5.1. The

influence of the solution flow profile, PE molecular weight (MW) and PDI structure on deposition efficiency, macroscopic and microscopic morphology and the potential for nanofiber alignment are investigated. The composite films were found to take on drastically different morphologies, ranging from highly serpentine, entangled fibers to nematic-like mats, depending on the PDI precursor used and the MW of the PE employed. The observed film morphologies are concluded to result from competitive "solution" and "surface" growth processes that depend on the degree of PDI precursor aggregation and the MW of the PE. Films exhibiting in-plane order were observed for composites prepared from C_7OPDI^+. In-plane organization is attributed to the presence of relatively large, rod-like PDI aggregates in the precursor solutions, and is aided by fluid shear present within the fluidic channel during deposition.

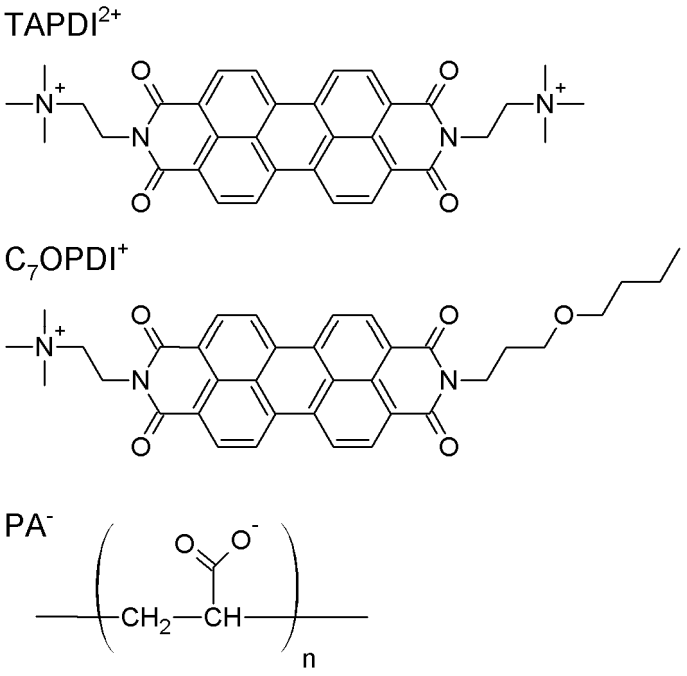

Figure 5.1 Structures for $TAPDI^{2+}$, C_7OPDI^+, and PA^-

Experimental Section

Preparation of Precursor Solutions

Perylene diimide dyes (PDIs) were synthesized using previously reported procedures.[14,36] Solutions of 250 μM PDI were prepared by first dissolving the solid dye in methanol. High purity (18 MΩ·cm) deionized water was subsequently added to give a

1:1 water:methanol mixture. The solutions were then heated on a hotplate to drive off the alcohol. Once the total solution volume reached ~ 25% of the original volume, a second volume of water was added. After further heating, to again reduce solution volume to ~ 25% of its original value, the dye solution was removed from the hotplate and allowed to cool. Finally, the solution was diluted to volume with water.

Poly(acrylate) (PA^-), sodium salt (M_W = 5100) and poly(acrylic) acid (M_W = 250K) were obtained from Aldrich as a solid and aqueous solution (35 wt%), respectively, and were used without further purification. Solutions of 4.4 mM PA^- (monomer) were prepared by either dissolving or diluting the PEs with 0.1 M, pH 7 phosphate buffer.

Fluidic Deposition of Composite films

Thin film deposition was performed using a home-built, computer-driven flow-control apparatus operated by software written in the National Instruments Labview programming environment. The flow control apparatus consisted of three solution reservoirs, computer-controlled solenoid pinch valves, a variable-rate peristaltic pump and a flow cell. Diagrams of the entire apparatus are shown in Figure 5.2.

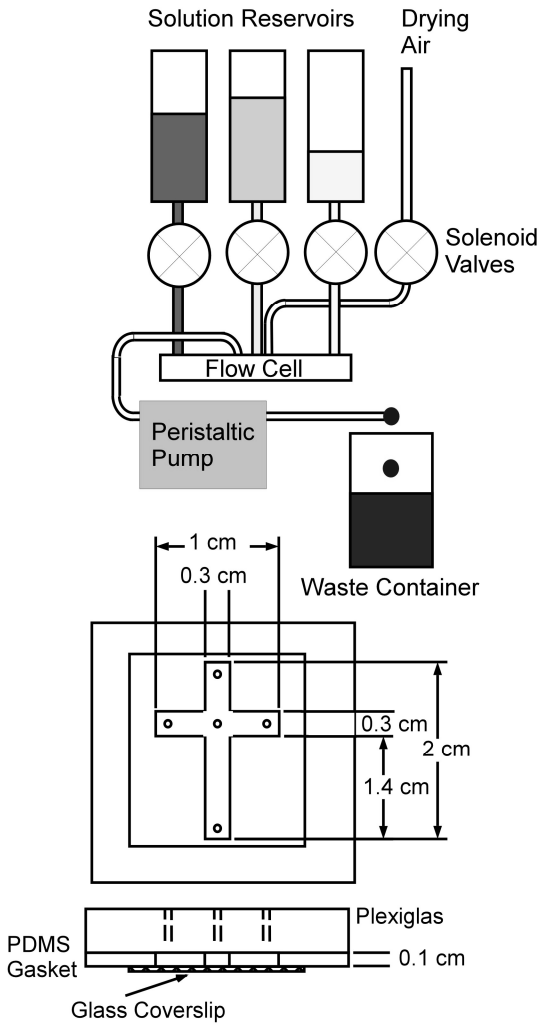

Figure 5.2 Flow Apparatus and Cell Dimensions. (Top) detailed view of flow control apparatus. (Bottom) schematic of complete flow cell showing Plexiglas chip, PDMS gasket and glass coverslip with relevant dimensions.

The flow cell incorporated channels in a cross-configuration and was constructed from a glass substrate, a custom-molded 1-mm thick polydimethylsiloxane (PDMS, Sylgard 184) gasket and a Plexiglas cover. The main deposition channel, defined by the PDMS gasket, was 14 mm long and 3 mm wide. Four inlet ports and one outlet port were machined through the Plexiglas cover to allow for solution infusion and withdrawal. Three of the four inlet ports were connected to reservoirs holding the PDI and PE precursor solutions and high purity rinse water. The fourth was left open to air to allow for drying of the film. The outlet port was connected to the peristaltic pump, which

served to pull the solutions through the flow cell. The entire apparatus allowed precise control of precursor sequence, flow rate and deposition time.

The general procedure for film deposition involved pumping solutions through the fluidic device in a six-step process. In order of execution, these steps were: 1) PDI deposition, 2) water rinse, 3) air dry, 4) PE deposition, 5) water rinse, and 6) air dry. The duration of each step was varied from 30 to 120 s, but was most commonly held at 30 s. All samples were prepared using a linear flow velocity of 1.4 mm/s, a value determined to closely approximate the substrate withdrawal rate in our previous studies of dip-coated films, and expected to result in lamellar flow (Reynold's number of 270).[15] One deposition cycle (i.e., the full six-step process) produces a sample consisting of one PDI/PE "bilayer". The deposition process was repeated as necessary to produce films of the desired thickness and optical density. All films were deposited on freshly plasma cleaned glass coverslips.

Sample Characterization

Polarized transmittance images of all samples were collected using a Nikon TE2000 inverted light microscope. This microscope was fitted with a 100 W tungsten-halogen illuminator, a 488 nm bandpass filter (10 nm passband), a calibrated dichroic glass polarizer, a condenser, and a 4X objective (Nikon, 0.13 numerical aperture). The polarizer and filter were mounted between the illuminator and condenser. All images were recorded in transmission, using a Roper Scientific CCD camera (CoolSNAP ES). Prior to collecting images, the condenser was adjusted to optimize sample contrast. Polarized transmittance images were collected for both clean coverslip "blanks" and for PDI/PE composite thin films. All images were corrected for dark current offset by subtracting the average camera signal obtained in dark images. The exposure time was held constant and was identical for all samples, blank, and dark images. The transmittance images were subsequently used to calculate absorbance and dichroism images (see below). Macroscale film morphology was assessed by inspection of these images. Average film absorbance and dichroism values were obtained by averaging the data over a region of interest (ROI) corresponding to the approximate center of the deposition channel in each case. The ROI had a width of 400 pixels and a height of 1040

pixels (1.6 μm/pixel) and was selected to ensure that any effects caused by the gasket-substrate and gasket-solution interfaces were excluded from the analysis. Localized microscopic film morphology was visualized using a Digital Instruments Multimode atomic force microscope (AFM, Veeco Metrology). All AFM images were recorded in tapping mode (TM-AFM) under dry nitrogen and utilizing silicon nitride tips.

Results

Fluidic Deposition

To demonstrate ESA of PDI/PE composites in fluidic devices, four general classes of thin films were prepared and characterized. These were derived from the four possible combinations of the C_7OPDI^+, $TAPDI^{2+}$, 5100 M_W PA^- and 250K M_W PA^- precursors. All such films were prepared in 5, 10, 15, 20 and 30 deposition cycles, at a linear solution flow rate of 1.4 mm/s with a 30 s step duration (see Experimental Section). Average film absorbance was employed to assess the rate of deposition for each of the composites. Absorbance images were obtained using a procedure described by Broadwell, et. al.[37] and a custom macro written in-house for ImageJ (open source image editing software). Separately-recorded dark, background, and sample transmission images were converted to absorbance images as defined in by:

$$A = -\log\left(\frac{I_{sample} - I_{dark}}{I_{blank} - I_{dark}}\right)$$

Here, I_{sample} and I_{blank} represent the sample and blank transmission images, respectively, and I_{dark} the average camera dark current. The average absorbance was obtained from central channel regions in each image using the ROI described above (Experimental Section). Figure 5.3 plots the average absorbance (unpolarized) obtained from each film as a function of the number of deposition cycles. These data depict a clear linear relationship between film absorbance and number of bilayers deposited for all four composites.

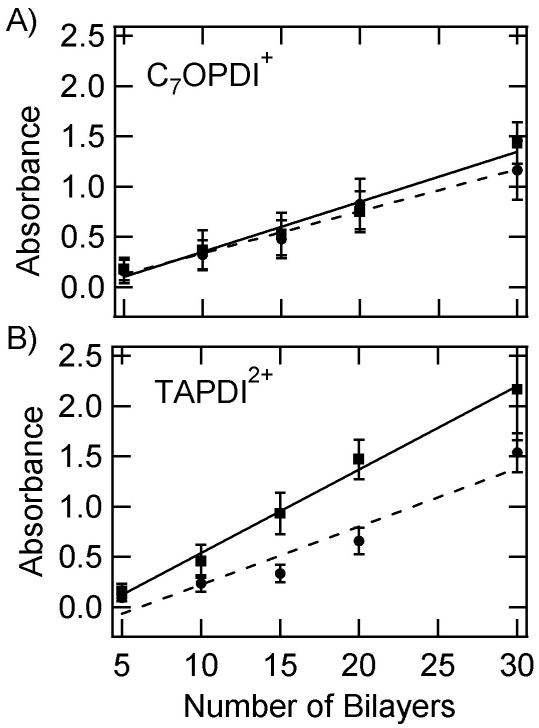

Figure 5.3 Absorbance vs. number of bilayer for A) C_7OPDI^+/PA^- and B) $TAPDI^{2+}/PA^-$ samples showing a linear increase in absorbance with increasing deposition cycles. Filled circles in each depict samples prepared from 5100 MW PA^-, while filled squares reflect samples prepared from 250K MW PA^-. The solid and dashed lines depict linear fits to the individual data sets.

Importantly, there are clear differences observed in the efficiencies of deposition for each composite, as reflected by the slopes and intercepts of each plot in Figure 3. These data show that PA^- MW has little impact on the deposition efficiency for C_7OPDI^+/PA^- composites. Both composites yield curves with nearly identical slopes (0.041±0.003 absorbance units (AU)/bilayer and 0.049±0.005 AU/bilayer for 5100 and 250K MW PA^-, respectively). In contrast, $TAPDI^{2+}/PA^-$ materials exhibited much greater sensitivity to PA^- MW. The slope of the plot obtained from $TAPDI^{2+}/PA^-$ composites grown from high MW PA^- is found to be 0.083±0.004 AU/bilayer, while 0.06±0.01 AU/bilayer is obtained from those grown with low MW PA^-. It is concluded that PA^- MW has little influence on the growth of C_7OPDI^+/PA^- composites but plays an important role in governing deposition of $TAPDI^{2+}/PA^-$ films.

Deposition efficiency was also found to depend upon the duration of substrate exposure to each precursor solution. Film absorbance was observed to increase with increasing exposure time and saturated at ~60 s duration for the flow rate employed in these studies (1.4 mm/s). The saturated absorbance was determined to be approximately twice that shown in Figure 5.3 (e.g., for 5 bilayers). A step duration of 30 s was employed here as a compromise that helped to conserve precursor solution.

Film Morphology

The macroscopic morphology of the PDI/PE films was assessed by inspection of the optical absorbance images obtained from each sample. Figure 5.4 depicts representative absorbance images of 15 bilayer $TAPDI^{2+}/PA^-$ and C_7OPDI^+/PA^- films (left and right columns, respectively). Images recorded for films of different thicknesses incorporate qualitatively similar features.

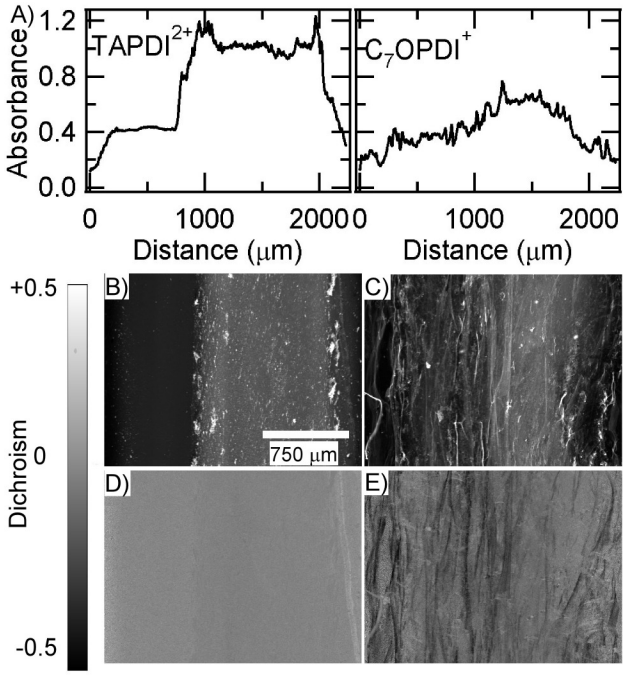

Figure 5.4 A) Average absorbance profiles, B) and C) perpendicularly-polarized absorbance images, and D) and E) dichroism images for 15 bilayer $TAPDI^{2+}/PA^-$ (250k M_W) sample and a 15 bilayer C_7OPDI^+/PA^- (250k M_W) sample (left and right respectively). These data show non-uniform absorbance across the channel width in both cases. The absorbance profiles plot average absorbance as a function of

position across the images shown in B) and C). The minimum and maximum absorbance values depicted by the grayscale in panels B) and C) are 0.09, 2.64 and 0.06, 1.44, respectively. The dichroism scale bar is for panels D) and E) only.

As shown in Figure 5.4, PDI/PE composite deposition is found to be nonuniform across the channel width (horizontal on the images shown). Film absorbance is greatest (on average) in central channel regions and smaller near the channel edges, as depicted in the absorbance profiles plotted in Figure 5.4A (data derived from Figure 5.4B,C). The channel center in the images shown lies just to the right of center on each. The observed nonuniformity is readily explained by the parabolic nature of the solution flow velocity profile within the channel. Exposure of the substrate to PDI and PE precursors is clearly greatest in the center of the channel, where the flow rate is also greatest. In the outer channel regions, due to the lower local flow rate, the film is exposed to significantly less precursor and the observed absorbance is greatly reduced.

The images shown in Figure 5.4 also depict differences in film uniformity for composites derived from the different PDI precursors. $TAPDI^{2+}/PA^{-}$ samples most often appear to be much more uniform than C_7OPDI^{+}/PA^{-} films. In addition, the large features observed in images of $TAPDI^{2+}/PA^{-}$ samples appear to be predominantly round or oblong in shape, while those in C_7OPDI^{+}/PA^{-} films take on a distinct fiber-like appearance. While large fiber-like features are also observed in $TAPDI^{2+}/PA^{-}$, they are noticeably less common. The fiber-like structures in C_7OPDI^{+}/PA^{-} are also extremely long, sometimes extending millimeters in length. Importantly, they are frequently oriented along the solution flow direction (vertical on the images shown). Finally, the largest features observed in the optical images of both composites tend to be found in outer channel regions, again reflecting the influence of the flow profile on deposition of large aggregates. Although the macroscopic morphology of sequentially deposited PDI/PE composites has not previously been assessed in this manner, the observation of flow-aligned fibrous structures in C_7OPDI^{+}/PA^{-} samples is consistent with our previous results.[15]

The microscopic morphology of the PDI/PE composites was characterized by TM-AFM imaging. Figure 5.5 shows representative images of $TAPDI^{2+}/PA^{-}$ composites

prepared with 5100 M_W and 250K M_W PA^-. Similarly, Figure 5.6 depicts images of C_7OPDI^+/PA^- samples.

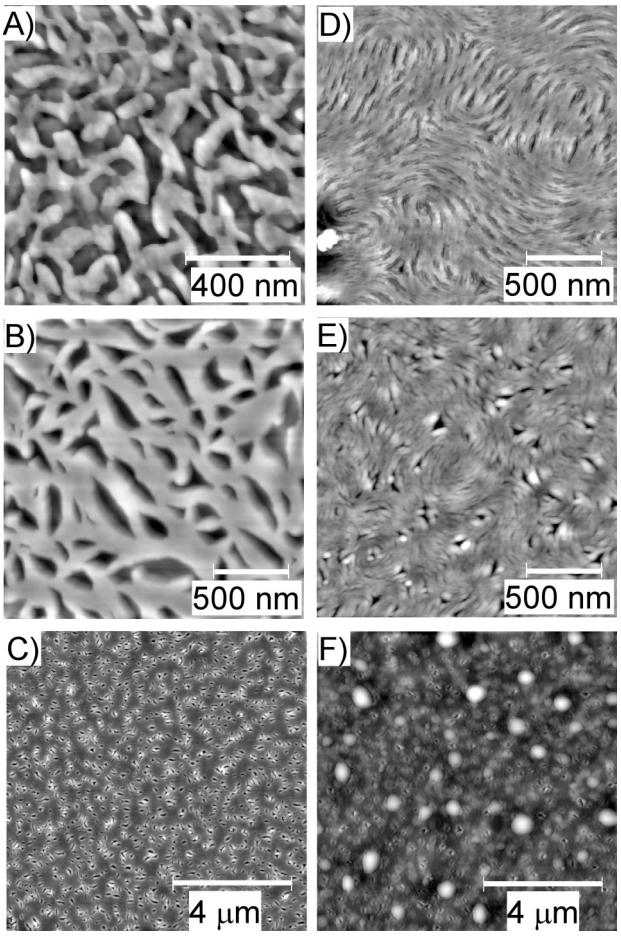

Figure 5.5 TM-AFM images of $TAPDI^{2+}/PA^-$ films. A)-C) images of 5, 10 and 15 bilayer samples respectively, prepared using 5100 MW PA^-. D)-F) images of 5, 10, and 15 bilayer samples, respectively, prepared using 250K MW PA^-. The full grayscale in each of these images depicts the following topographic heights: A) 9.3 nm, B) 53.3 nm, C) 32.5 nm, D) 18.3 nm, E) 18.1 nm and F) 127.5 nm.

As expected from the optical images, the TM-AFM data show that the C_7OPDI^+/PA^- films are generally rougher and less uniform than the $TAPDI^{2+}/PA^-$ composites. Multiple images recorded from these samples (data not shown) also depict clear variations in morphology across the channel width in each case. As reported previously,[14,15] images obtained from relatively thinner films depict features that are more readily distinguished and classified. Relatively thicker films tend to exhibit extreme

roughness and the presence of nondescript round or oblong topographic protrusions.[14,15] The images in Figure 5.5 were acquired from central channel regions and reflect the relatively smaller roughness of the $TAPDI^{2+}/PA^{-}$ films. The images in Figure 5.6 were acquired from regions displaced from the channel center, as central regions were frequently too rough to yield useful images.

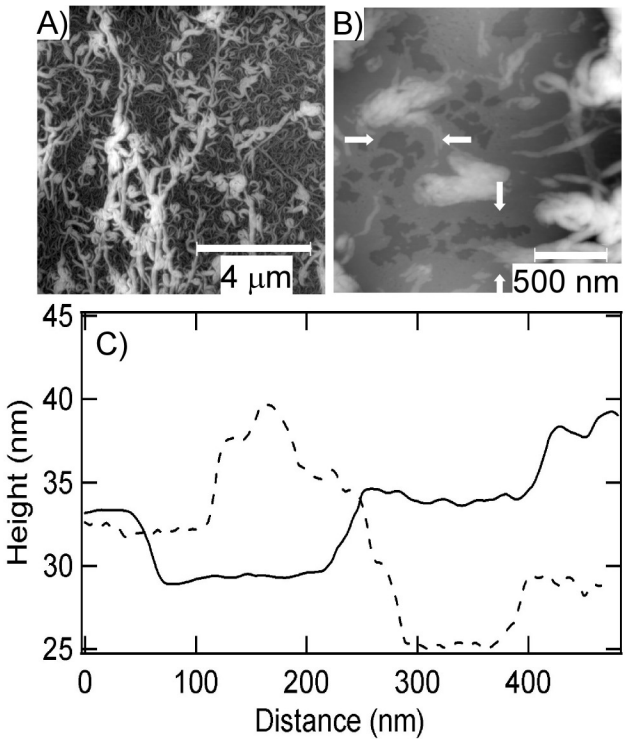

Figure 5.6 TM-AFM image of C_7OPDI^{+}/PA^{-} composites. A) 5 bilayers film prepaed from 250k M_W PA^{-} showing fibrous structures. B) Ten bilayer film prepared from 250k M_W PA^{-} showing fibers and planar structures. C) line profiles (between arrows in panel B) showing planar structures of ~4-5 nm heights. The planar structures are believed to form by "surface growth" mechanism described in the text.

The images obtained from $TAPDI^{2+}/PA^{-}$ films show clear evidence for the growth of oblong PDI/PE composite aggregates. The 5 bilayer film prepared using low MW PA^{-} (Figure 5.5A) incorporates short (~300 nm long), narrow (~100 nm wide) aggregates. As the number of bilayers deposited increases, these oblong features become interconnected, forming what look like random interconnected nanofibers, as shown in Figure 5.5B. Finally, as even more material is deposited (Figure 5.5C), a relatively uniform film

incorporating small "pinholes" is obtained. The pinholes form between the individual nanofibers.

When high MW PA^- ($M_W = 250K$) is employed in formation of $TAPDI^{2+}/PA^-$, the aggregates formed take on a noticeably different appearance. Namely, they appear as distinct nanofibers (see Figure 5.5D). These nanofibers are much longer and narrower than those observed when low MW PA^- ($M_W = 5100$) is employed. Interestingly, the nanofibers comprising the films prepared from high MW PA^- also form small nematic-like domains. The appearance of these domains suggests the fibers more readily form fluid nematic-like phases during film deposition, unlike those obtained from low MW PA^-. It may also indicate they are more readily annealed when exposed to aqueous solution. The observation of nematic-like order in these films is consistent with previous results on symmetric, doubly charged PDIs reported by Tam-Chang and coworkers,[39,40] and other so-called chromonic liquid crystals.[41] Once again, as the amount of material deposited increases, the nanofibers tend to grow together (Figure 5.5E), ultimately forming a relatively uniform film (Figure 5.5F) incorporating well-separated pinholes. The pinholes clearly form at intersections and domain boundaries between the nanofibers. In both sets of films (high and low MW PA^-), the pinholes are also observed to be associated with features of increased topographic height. It is likely the topographic protrusions apparent in Figure 5F form at these pinhole sites (see Figure 5.5E). Such protrusions may form due to increased reactivity of the films at these pinhole sites, or they may simply result from delamination and reorganization of the composites around the pinholes.

AFM images of the C_7OPDI^+/PA^- samples show much less variability with PA^- MW. Highly fibrous C_7OPDI^+/PA^- films are formed in both cases (see Figure 5.6). As more material is deposited, the films become increasingly rough and incorporate round or oblong protrusions. We have previously shown that the fibers in C_7OPDI^+/PA^- samples tend to align parallel to the flow direction. Such alignment is clearly apparent in Figure 6A, for which the flow direction corresponds to vertical on the image. Most interesting in the present study, however, is the observation of apparently "planar" domains in thinner regions of some C_7OPDI^+/PA^- films (see Figure 5.6B). The line profiles plotted in Figure 6C (taken from Figure 6B) show that these domains have heights of ~4-5 nm.

Such regions have not been previously described and are tentatively assigned the same origins as the relatively smooth nematic-like nanofibrous domains found in $TAPDI^{2+}/PA^-$ films. Specifically, it is believed they are comprised of small, well-packed nanofibrous mats in which the individual nanofibers are too small to be distinguished at the available resolution. Alternatively, they may reflect the presence of planar PDI/PE bilayers.[36]

Chromophore Alignment—Dichroism studies

Chromophore alignment was assessed by microscopic dichroism measurements. The lowest energy electronic transition of PDI dyes is aligned parallel to the molecular long axis.[42-44] Dichroism images were calculated directly from the absorbance images described above. In this case, the light employed in absorbance imaging was polarized alternately parallel and perpendicular to the solution flow direction. The dichroism, D, in each case was determined by:

$$D = \frac{A_{\parallel} - A_{\perp}}{A_{\parallel} + A_{\perp}}$$

Where $A_{\parallel}$ represents the absorbance image obtained with light polarized parallel to the solution flow direction and $A_{\perp}$ the absorbance image acquired with light polarized perpendicular to solution flow. A dichroism of -1 corresponds to perfect perpendicular alignment of the PDI long axis with respect to the flow direction, while a value of +1 represents perfect alignment parallel to solution flow. Figure 5.4D,E depict representative dichroism images. Average dichroism values were obtained from each such image by averaging the local dichroism data over the ROI described in the Experimental Section.

Figure 5.7 plots average dichroism results obtained from C_7OPDI^+/PA^- and $TAPDI^{2+}/PA^-$ composites.

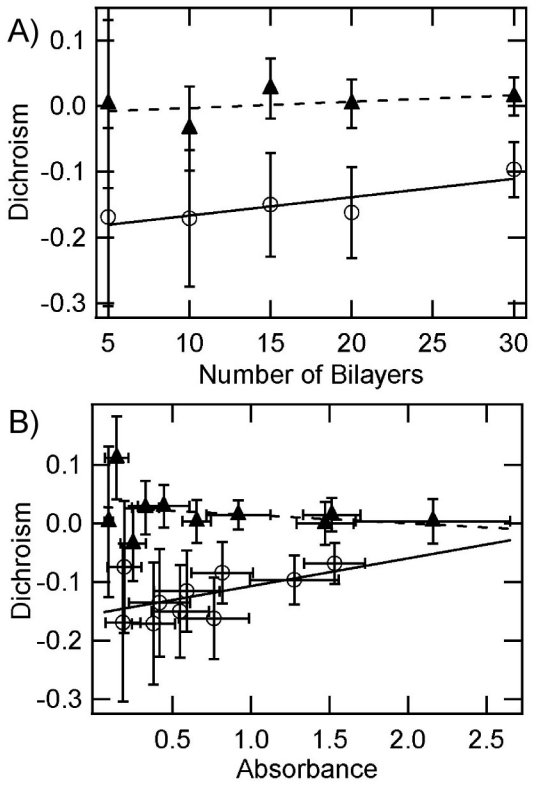

Figure 5.7 Dichroism Data from $TAPDI^{2+}/PA^-$ and C_7OPDI^+/PA^- films. A) plot of dichroism vs. number of bilayers (film prepared using low MW PA^-). The C_7OPDI^+/PA^- (open circles, solid line) exhibit clear evidence for alignment of the PDI chromophores perpendicular to the flow direction. The samples become less well organized at higher deposition cycles. No such trend is observed for $TAPDI^{2+}/PA^-$ composites (filled triangles, dashed line), which also depict no evidence of macroscopic alignment. B) Dichroism as a function of film absorbance, further demonstrating the difference in organization for $TAPDI^{2+}/PA^-$ (filled triangle, dashed line) and C_7OPDI^+/PA^- films (open circles, solid line) and the reduction in alignment observed with increasing film thickness for the latter. Data for films prepared from low and hight MW PA^- have been combined. Error bars represent the standard deviation of each measurement.

The $TAPDI^{2+}/PA^-$ samples showed no net chromophore alignment (see Figure 7A), regardless of film thickness and PA^- MW. Mean dichroism values for $TAPDI^{2+}/PA^-$ formed from low and high MW PA^- were 0.00±0.05 and 0.03±0.03, respectively (error

bars give the 90% confidence intervals, (CI). In contrast, all C_7OPDI^+/PA^- films yielded dichroism values that differed significantly from zero (see Figure 5.7A), indicating the presence of significant molecular alignment within the films. The negative dichroism values obtained indicate the C_7OPDI^+ chromophores align predominantly perpendicular to the solution flow direction.

In contrast to $TAPDI^{2+}/PA^-$ films, alignment in the C_7OPDI^+/PA^- samples exhibited a detectable dependence upon PA^- MW and was statistically significant at the 66% confidence level. The average dichroism value obtained from samples prepared with high MW PA^- was -0.10 ± 0.05 (90% CI), while the dichroism obtained from low MW PA^- samples was -0.15 ± 0.06 (90% CI), demonstrating that PDI alignment is better in films derived from low molecular weight PA^-.

As previously observed for dip-coated samples,[15] the C_7OPDI^+ chromophores became more disordered in thicker films, as reflected by the trend in the dichroism data towards zero with increased deposition cycles (see Figure 5.7A). Further evidence of this trend is drawn from Figure 5.7B, which plots average dichroism as a function of average film absorbance. As shown in these data, C_7OPDI^+/PA^- films exhibiting smaller absorbance tend to yield more negative dichroism values. Again, no such trend is observed for $TAPDI^{2+}/PA^-$.

It is important to stress that the dichroism values only measure PDI chromophore alignment within the films, and do not, *a priori*, represent measurements of nanofiber alignment. Nevertheless, as we have shown previously,[14] the PDI chromophores in PDI/PE composites tend to align perpendicular to the long axis of the nanofibers. Thus, the dichroism results are also consistent with nanofiber alignment along the solution flow direction for C_7OPDI^+/PA^- composites.

The dichroism images shown in Figure 5.4D,E also provide evidence in support of the above conclusions on PDI chromophore and fiber alignment (or lack thereof) in the PDI/PE composite films. Notably, the $TAPDI^{2+}/PA^-$ films show no clear contrast in the dichroism images. Dichroism values that differ significantly from zero are neither observed in "uniform" film regions (as deduced from the absorbance images) nor for the relatively large aggregated structures, suggestive of a distinct lack of order in these materials. While the nematic domains depicted in the AFM images are too small to

distinguish with the resolution afforded by the optical microscope (i.e. ~ 2.5 μm), the larger aggregates should yield detectable nonzero dichroism values, if they contain aligned dye. The dichroism images collected from these samples therefore suggest that the dye is much less well ordered in the $TAPDI^{2+}/PA^-$ aggregates than in the C_7OPDI^+/PA^- composites.

On the other hand, the dichroism images obtained from C_7OPDI^+/PA^- films show clear contrast (see Figure 5.4E). Such images depict relatively darker regions (i.e., more negative dichroism values) associated with the large fibrous features observed in the corresponding absorbance images. Importantly, these fibers are aligned primarily along the solution flow direction (vertical on the images). The negative dichroism values observed from the large fibers provides strong evidence for PDI alignment within the fibers, with the predominant alignment being perpendicular to the long fiber axis. The dichroism values observed in relatively uniform film regions devoid of large fibers are also observed to be statistically different from zero (i.e. more negative). As a result, it is concluded these regions incorporate smaller (unresolved) nanofibers (such as those shown in the AFM images) that are also aligned predominantly along the solution flow direction.

Discussion

To our knowledge, the results presented above represent the first demonstration of electrostatic self-assembly of aligned dye/PE composites from flowing solutions within a fluidic device. In characterizing these materials, we explored the impacts of position with the fluidic channel, PDI structure and PE MW on materials deposition efficiency, macroscopic and microscopic film morphology and nanofiber alignment. The results showed that $TAPDI^{2+}/PA^-$ films were most efficiently deposited when high MW PA^- was employed and were least efficiently deposited in the presence of low MW PA^-. In contrast, C_7OPDI^+/PA^- deposition was found to be virtually independent of PA^- MW. In our previous report, we showed that both $TAPDI^{2+}$ and C_7OPDI^+ were aggregated in their respective precursor solutions, but that C_7OPDI^+ was much more strongly aggregated, forming relatively large, rod-like aggregates in the absence of PE. The apparent independence of C_7OPDI^+/PA^- deposition on PA^- MW is consistent with our previous

conclusion that precursor aggregation is an important factor in governing growth of these materials. In the case of C_7OPDI^+, preformed PDI aggregates clearly dominate the mechanism of composite formation. For $TAPDI^{2+}/PA^-$, it is clear that the PE plays a more significant role in the deposition process, while the more weakly aggregated $TAPDI^{2+}$ plays a lesser role. Higher MW PA^- leads to formation of larger aggregated structures, increasing the efficiency of deposition and reducing the potential for dissolution of the composite.

The optical and AFM imaging results also show that $TAPDI^{2+}/PA^-$ films are much more uniform than C_7OPDI^+/PA^- films. This observation is again consistent with the dominant role played by preformed C_7OPDI^+ aggregates in C_7OPDI^+/PA^- composite formation. The deposition of large, preformed aggregates on the substrate surface leads to enhanced film roughness. The much smaller preformed aggregates present in the $TAPDI^{2+}$ solution yield more tightly packed aggregates and smoother films.

Finally, the dichroism results show that nanofibrous C_7OPDI^+/PA^- aggregates are readily aligned by solution flow, while similar $TAPDI^{2+}/PA^-$ composites appear to be unaligned. These observations may again be attributed to the importance of preformed C_7OPDI^+ aggregates in the former. The rod-like aggregates formed from C_7OPDI^+ align along the solution flow direction during deposition and are subsequently deposited on and bound to the growing film in an aligned state. The $TAPDI^{2+}$ aggregates are concluded to be too small to be aligned by solution flow, and are thus deposited in an unaligned state.

The discussion above has led to the development of two distinct models for the mechanisms of nanofiber growth and alignment within sequentially deposited PDI/PE composite films. Here, these are referred to as the "solution growth" and "surface growth" mechanisms, the former having been described in our previous work. It is believed that all four classes of PDI/PE composite grow by both of these mechanisms, but that one of the two dominates in each case, depending on PDI structure. In the "solution growth" mechanism, preformed π-stacked rod-like PDI aggregates present in the precursor solution serve to template the growth of nanofibers (and larger structures). The rod-like aggregates are bound to the surface in their preexisting form by the PA^-. Because C_7OPDI^+ is known to be most heavily aggregated, formation of C_7OPDI^+/PA^- composite nanofibers is dominated by this mechanism and little dependence on PE

characteristics are observed. The observation of the "planar" structures in some C_7OPDI^+/PA^- films (see Figure 5.6B) is taken as evidence for the minor role played by "surface growth" in these films (see below).

In contrast, growth of the $TAPDI^{2+}/PA^-$ composites is believed to occur primarily by the "surface growth" mechanism, with minor contributions from "solution growth". The "surface growth" mechanism involves the self-assembly of PDI monomers or small π-stacked aggregates along the PA^- backbone, on the surface of the growing composite. In this case, it is the PA^- that governs templated growth of the nanofibers, as evidenced by the morphological differences observed for films prepared from low and high MW PA^-. The high concentration of small polymer-bound aggregates produced during the drying step may lead to formation of a lyotropic liquid crystalline phase. These materials may also be further modified by solvent annealing during later deposition cycles. In the case of $TAPDI^{2+}/PA^-$, the nematic nanofibrous films shown in Figure 5.5D,E are taken as strong evidence for participation of the "surface growth" mechanism, while the larger features observed in Figure 5.4B provide evidence for the minor involvement of "solution growth" processes.

Conclusions

In summary, this chapter describes the deposition of aligned, electrostatically self-assembled dye/PE composites from flowing solutions within fluidic devices. Optical absorbance and dichroism imaging along with AFM imaging were used to characterize the composite materials obtained. Materials deposition efficiency, macroscopic and microscopic film morphology and nanofiber alignment were investigated as a function of position within the fluidic channel, PDI structure and PE MW. The composite films formed all showed linear relationships between film absorbance and the number of bilayers deposited, with the efficiency of deposition governed by PE MW in the case of $TAPDI^{2+}/PA^-$ and by precursor aggregate size in C_7OPDI^+/PA^- composites. The films formed took on distinctly different morphologies, incorporating relatively large, serpentine fibers in the case of C_7OPDI^+/PA^- and relatively uniform nanofibers that formed nematic-like domains in the case of the $TAPDI^{2+}/PA^-$ films (high MW PA^-). Film morphology was also observed to be sensitive to PE MW in the $TAPDI^{2+}/PA^-$

composites. Nanofibers formed in the C_7OPDI^+/PA^- composites were shown to align along the solution flow direction, while the PDI chromophores from which they were assembled aligned perpendicular to the flow direction. No such alignment was observed in $TAPDI^{2+}/PA^-$ films. Two distinct mechanisms were proposed to describe the different deposition, morphological and alignment characteristics of these materials. C_7OPDI^+/PA^- composites were concluded to grow primarily via a "solution growth" mechanism that relies on the formation of preaggregated π-stacked PDI nanorods in the precursor solution. In contrast, $TAPDI^{2+}/PA^-$ films were concluded to grow primarily by a "surface growth" mechanism in which small PDI aggregates or monomers self-assemble along PE chains previously deposited on the film surface. The materials and alignment methods described above are likely to play a role in the development of anisotropic organic thin films for use as one-dimensional conductors, Polaroid films and/or polarized electroluminescent devices.

REFERENCES

(1) Decher, G. *Science* **1997**, 277, 1232-1237.

(2) Hammond, P. T. *Adv. Mater.* **2004**, 16, 1271-1293.

(3) Ariga, K.; Hill, J. P.; Ji, Q. *Phys. Chem. Chem. Phys.* **2007**, 9, 2319-2340.

(4) Decher, G.; Hong, J. D. *Ber. Bunsenges. Phys. Chem.* **1991**, 95, 1430-1434.

(5) Decher, G.; Hong, J. D.; Schmitt, J. *Thin Solid Films* **1992**, 210/211, 831-835.

(6) Ferreira, M.; Cheung, J. H.; Rubner, M. F. *Thin Solid Films* **1994**, 244, 806-809.

(7) Ferreira, M.; Rubner, M. F. *Macromolecules* **1995**, 28, 7107-7114.

(8) Cooper, T. M.; Campbell, A. L.; Crane, R. L. *Langmuir* **1995**, 11, 2713-2718.

(9) Yoo, D.; Wu, A.; Lee, J.-K.; Rubner, M. F. *Synth. Metals* **1997**, 85, 1425-1426.

(10) Yoo, D.; Lee, J.-K.; Rubner, M. F. *Mat. Res. Soc. Symp. Proc.* **1996**, 413, 395-399.

(11) Ariga, K.; Lvov, Y.; Kunitake, T. *J. Am. Chem. Soc.* **1997**, 119, 2224-2231.

(12) Chang-Yen, D. A.; Lvov, Y.; McShane, M. J.; Gale, B. K. *Sensors and Actuators B* **2002**, 87, 336-345.

(13) Bradley, M. S.; Tischler, J. R.; Bulovic, V. *Adv. Mater.* **2005**, 17, 1881-1886.

(14) Everett, T. A.; Twite, A. A.; Xie, A.; Battina, S. K.; Hua, D. H.; Higgins, D. A. *Chem. Mater.* **2006**, 18, 5937-5943.

(15) Weitzel, C. R.; Everett, T. A.; Higgins, D. A. *Langmuir* **2009**, 25, 1188-1195.

(16) Zhang, X.; Gao, M.; Kong, X.; Sun, Y.; Shen, J. *J. Chem. Soc. Chem. Commun.* **1994**, 1055-1056.

(17) Araki, K.; Wagner, M. J.; Wrighton, M. S. *Langmuir* **1996**, 12, 5393-5398.

(18) Tang, T.; Qu, J.; Mullen, K.; Webber, S. E. *Langmuir* **2006**, 22, 26-28.

(19) Doherty, W. J.; Friedlein, R.; Salaneck, W. R. *J. Phys. Chem. C* **2007**, 111, 2724-2729.

(20) Schlenoff, J. B.; Dubas, S. T.; Farhat, T. *Langmuir* **2000**, 16, 9968-9969.

(21) Izquierdo, A.; Ono, S. S.; Voegel, J.-C.; Schaaf, P.; Decher, G. *Langmuir* **2005**, 21, 7558-7567.

(22) Lee, S.-S.; Hong, J.-D.; Kim, C. H.; Kim, K.; Koo, J. P.; Lee, K.-B. *Macromolecules* **2001**, 34, 5358-5360.

(23) Lee, S.-S.; Lee, K.-B.; Hong, J.-D. *Langmuir* **2003**, 19, 7592-7596.

(24) Hammond, P. T.; Whitesides, G. M. *Macromolecules* **1995**, 28, 7569-7571.

(25) Clark, S. L.; Montague, M. F.; Hammond, P. T. *Macromolecules* **1997**, 30, 7237-7244.

(26) Barker, S. L. R.; Tarlov, M. J.; Canavan, H.; Hickman, J. J.; Locascio, L. E. *Anal. Chem*. **2000**, 72, 4899-4903.

(27) Lefaux, C. J.; Mather, P. T. *Mat. Res. Soc. Symp. Proc.* **2004**, EXS-2, 47-49.

(28) Shchukin, D.; Kommireddy, D. S.; Zhao, Y.; Cui, T.; Sukhorukov, G. B.; Lvov, Y. *Adv. Mater*. **2004**, 16, 389-393.

(29) Jang, H.; Kim, S.; Char, K. *Langmuir* **2003**, 19, 3094-3097.

(30) Kim, H.-J.; Lee, K.-B.; Kumar, S.; Kim, J. *Langmuir* **2005**, 21, 8532-8538.

(31) Krishnan, M.; Petrasek, Z.; Monch, I.; Schwille, P. *Small* **2008**, 4, 1900-1906.

(32) Sivagnanam, V.; Sayah, A.; Vandevyver, C.; Gijs, M. A. M. *Sensors and Actuators B* **2008**, 132, 361-367.

(33) Lee, J. S.; Um, E.; Park, J.-K.; Park, C. B. *Langmuir* **2008**, 24, 7068-7071.

(34) Schnieder, T.; Artyushkova, K.; Fulghum, J. E.; Broadwater, L.; Smith, A.; Lavrentovich, O. D. *Langmuir* **2005**, 21, 2300-2307.

(35) Schneider, T.; Lavrentovich, O. D. *Langmuir* **2000**, 16, 5227-5230.

(36) Xie, A.; Liu, B.; Hall, J. E.; Barron, S. L.; Higgins, D. A. *Langmuir* **2005**, 21, 4149-4155.

(37) Broadwell, I.; Fletcher, P. D. I.; Haswell, S. J.; McCreedy, T.; Zhang, X. *Lab Chip* **2001**, 1, 66-71.

(38) Rasband, W. Image J. http://rsbweb.nih.gov/ij/index.html.

(39) Iverson, I. K.; Casey, S. M.; Seo, W.; Tam-Chang, S.-W. *Langmuir* **2002**, 18, 3510-3516.

(40) Tam-Chang, S.-W.; Iverson, I. K.; Helbley, J. *Langmuir* **2004**, 20, 342-347.

(41) Tam-Chang, S.-W.; Huang, L. *Chem. Comm.* **2008**, 1957-1967.

(42) Kazmaier, P. M.; Hoffmann, R. *J. Am. Chem. Soc.* **1994**, 116, 9684-9691.

(43) Adachi, M.; Murata, Y.; Nakamura, S. *J. Phys. Chem*. **1995**, 99, 14240-14246.

(44) Struijk, C. W.; Sieval, A. B.; Dakhorst, J. E. J.; van Dijk, M.; Kimkes, P.; Koehorst, R. B. M.; Donker, H.; Schaafsma, T. J.; Picken, S. J.; van de Craats, A. M.; Warman, J. M.; Zuilhof, H.; Sudhölter, E. J. R. *J. Am. Chem. Soc.* **2000**, 122, 11057-1106

CHAPTER 6 - Conclusion and Future Directions

Conclusion

Layer-by-layer electrostatic self-assembly was used for the controlled deposition of a nanofibrous perylene diimide/polyelectrolyte composite material. A total of 4 new composite materials were prepared, ($C_{11}OPDI^{+}/PA^{-}$, C_7OPDI^{+}/PA-, $TAPDI^{2+}/PA^{-}$, and $PDISO_3^{2-}/PDDA^{+}$). All composites were deposited from aqueous precursor solutions in a sequential fashion using an automated dip-coater or fluidic device. Briefly, the deposition process involved exposing a clean glass substrate to the cationic precursor, a rinse with distilled water, exposure to the anionic precursor, followed by a second rinse with distilled water. Between each deposition and rinsing step the substrate was allowed to dry briefly in ambient air. By using a computer controlled dip-coater, substrate exposure time, insertion rate and extraction rate were defined. The resultant composite films were composed of insoluble, PDI/PE fibers, supported by the glass substrates. TM-AFM indicated that individual fibers typically had a length of tens to hundreds of micrometers and widths that were proportional to the number of deposition cycles. In all cases, a linear relationship between film absorbance and number of deposition cycles was observed. Polarization dependant fluorescence microscopy indicated that the PDI chromophore aligned perpendicular to the fiber's local long axis, which is indicative of extended π-stacks of the PDI molecules. This organization was confirmed through polarization dependent absorbance measurements, where negative dichroism values were obtained. Bulk solution phase studies of the precursor solutions indicate that the PDIs exist in a preformed aggregated state. The relative strength and size of the PDI aggregates was probed through temperature dependent fluorescence and filtration studies. It was found that of the C_7OPDI^{+}, $TAPDI^{2+}$, and $PDISO_3^{2-}$ derivatives, the C_7OPDI^{+} formed the most strongly associated and largest aggregates. It was also noted that the C_7OPDI^{+}/PA^{-} composite had a tendency to form fibrous structures that exhibited a degree of in-plane organization.

In a related study, nanofibrous PDI/PE composite materials were deposited from continuously flowing solution within a fluidic device, conclusively demonstrating the

patterned deposition of aligned nanofibrous composites from aqueous precursor solutions. For these studies, $TAPDI^{2+}$ and C_7OPDI^{+} were again used in conjunction with 5100 MW and 250K MW poly(acrylic) acid. The impact PE MW and pressure driven flow had on the resultant film morphology was explored. PDI/PE composite deposition was achieved through the sequential exposure of a glass substrate to flowing anionic precursor, water, cationic precursor and a final water rinse. Through electrostatic interactions of the cationic PDIs and the anionic polyelectrolyte, the composite material was formed. The influence of solution flow rate, PE molecular weight, and PDI structure on the resultant composite macroscopic and microscopic film morphology was examined. The composite films formed all showed linear relationships between film absorbance and the number of bilayers deposited. The efficiency of deposition was governed by PE MW in the case of $TAPDI^{2+}/PA^{-}$, and by precursor aggregate size in C_7OPDI^{+}/PA^{-} composites. The film morphologies formed from $TAPDI^{2+}/PA^{-}$ and C_7OPDI^{+}/PA^{-} showed distinct differences. Composites formed from C_7OPDI^{+}/PA^{-} took on more fibrous morphologies regardless of the MW of the PE, while the $TAPDI^{2+}/PA^{-}$ composites had morphologies that were more uniform, with large nematic-like domains whose structures was highly dependent on the MW of the PE. For the case of C_7OPDI^{+}/PA^{-} nanofibers were aligned parallel to the solution flow direction, no such organization was observed for the $TAPDI^{2+}/PA^{-}$ composite, and the chromophore long axis was oriented perpendicular to the nanofibers long axis. This organization is consistent with the presences of extended π-stacks of PDI nanorods. Based on the data a two part, competitive mechanisms was developed to explain the observed film morphologies. The two mechanisms were coined the "surface growth" and "solution growth" mechanisms. For the C_7OPDI^{+}/PA^{-} composites the "solution growth" mechanism was determined to be the dominant mechanism. The solution growth mechanism relies on the aggregation of the C_7OPDI^{+} chromophore into extended π-stacked nanorods in the precursor solution prior to being deposited on the substrate surface, while the "surface growth" mechanism is dependent on small PDI aggregates and monomers self-assembling along previously deposited PE polymer chains.

Future Direction

The future of this work may go in two distinct directions, a fundamental route and a practical application route. The fundamental route would further study the PDI aggregates structure and physical characteristics and the role the physical structure plays in film morphology while the practical application route would attempt to use these fibrous materials in useful applications. Below are some of the experiments and applications that I see as being most beneficial from a scientific perspective.

Fundamental Studies

Determination of Aggregate Size and Structure

As we have shown in this work, aggregate size and aggregation strength play an important role in determining the resultant film morphology. In chapter 4 of this dissertation, determination of aggregate size was completed. This work utilized UV-Vis absorbance spectroscopy to quantify the amount of dye that was passed through a filter having a known pore size. This rudimentary experiment was able to give a very rough estimate on aggregate size although no information on aggregate size distribution or shape was obtained. The first proposed experiment would attempt to determine not only the size but also the distribution of sizes of the aggregated PDI in the precursor solution. This would be done through capillary electrophoresis (CE). CE has been show to be a useful technique for the separation of small molecules and recently started being used for the separation of nanoparticles.[(1)] The structure of the nanoparticles could be studied by small angle x-ray scattering. These techniques would allow the determination of PDI aggregate size and PDI order within the aggregates.

Impact of Molecular Moieties

A logical experimental off-shoot of the size/structure study would be to look at how the molecular structure can be used to tune the aggregates and give films of desired morphology. Again in Chapter 4, I was able to link film morphology to aggregation strength, charge and structure, this should be expanded to examine other PDI derivatives

having longer or shorter tail lengths and then expanding to other, similar, molecular species which are known to aggregate in solution.

Resistivity/Electronic studies of single PDI "Wires"

The most difficult of the fundamental studies from an execution standpoint is the measurement of the electronic properties of the PDI aggregates. As the work in chapter 5 demonstrated, it is possible to control both the location of film deposition but also the orientation of the fibers within the films. This degree of control should facilitate the study of conductivity along a fiber. Careful lithographic and microfabrication techniques could be used to assemble an array of electrodes that are separated by only a couple of microns. Then by depositing a flow aligned film across the electrode array electrical contacts between adjacent electrodes could be made through the fibrous material. A study of this type would allow further optimization of the composite material by experimentally observing the role molecular structure plays in the resultant conductivity, thus allowing better semiconducting material to be synthesized.

Alternatively, experiments similar to break-junction measurements could be made utilizing scanning probe microscopy techniques.[(2)]

Quantitative Image Analysis

Although not perfect, the image analysis procedures used to quantify fiber alignment did a reasonable job at giving a semi-quantitative measure of nanofiber alignment. In the future, more work needs be completed to develop a more quantitative means of determining fiber orientation that does not rely on human judgment or intervention.

Practical Applications

The semiconducting properties of the perylene diimides make them good candidates for electronic applications. Three of many possible venues to explore from a practical application standpoint, some of the more interesting include solar cells, OLED's, and various chemical/physical sensors.

Solar Cells

It has been shown from early on that PDIs are highly fluorescent, light stable and robust molecules. These attributes, in addition to the semiconducting properties, make PDIs an ideal candidate for active components in photovoltaic devices. To advance this field working PVs should be made using fibrous PDIs as the n-type, electron transporting component. From what I observed good starting point would to be construct bulk heterojunciton devices with a good hole conducting material (such as PEDOT:PSS) cast onto a indium tin oxide coated glass slide and indium or silver as the back electrode. To better the chances of making a functional device this ideally should be done under a nitrogen atmosphere, and the entire device should be embedded in optical adhesive. Additionally, the working area of these devices should be kept small as possible. The smaller the working area, the less the chance of localized "shorting". Ideally, the extended π-stacks of the PDI aggregates would enhance the external conversion efficiency of the device, and result in more efficient solar cells.

Polarized LEDs

Similarly to PVs, layered devices could be constructed and tested, exploring the light emitting properties of the PDI/PE composites. In the case of highly aligned nanofiber films, it would be interesting to see the degree of polarized light that could be emitted from a working diode. The extent of polarization could be used to quantify the level of nanofiber alignment.

Sensors

Recently, more reports of the applicably of PDIs as chemical sensors has been published.[3, 4] Works such as these suggest that active films which contain PDIs may be useful for a number of sensing applications. Further work at identifying specific chemicals and sensing conditions would be a first step at developing these fibrous materials as possible chemical specific sensors.

REFERENCES

(1) Surugau, N.; Urban, P. L. *J. Sep. Sci.* **2009**, *32*, 1889.

(2) Xu, B.; Tao, N. J. *Science.* **2003**, *301*, 1221.

(3) Yan, L. W.; Yang, L.; Lan, J. B.; You, J. S. *Science in China, Series B.* **2009**, *54*, 518.

(4) Che, Y.; Yang, X.; Zang, L. *Chemical C.* **2008**, *12*, 1413.

Appendix A - Microfluidic PDI Alignment

Electrostatic self-assembly (ESA) of organic thin films is often accomplished by sequentially dipping a substrate in a series of aqueous solutions of cationic and anionic precursors.[1] These layer-by-layer (LbL) methods afford molecular level control over film thickness and composition but little control over the in-plane orientational order of the molecules being deposited. ESA methods that provide a means to control molecular organization would be very useful in the fabrication of organic electronic, optical, and optoelectronic devices.[2,3] Such methods could be used in the production of organic thin film transistors, in which ordered materials have been shown to yield enhanced device performance.[4,5] Likewise, such methods could also be used to prepare organic electroluminescent films that emit polarized light.[6] Despite these and other benefits, few ESA methods that yield organized molecular materials have been reported to date.[7] In this appendix, we demonstrate that well-ordered nanofibrous composites of a cationic perylene diimide dye and an anionic polyelectrolyte[8] can be obtained by sequential deposition from flowing solutions in microfluidic devices.[9,10] Bulk UV-visible absorption dichroism data show that the dye molecules within the composites align perpendicular to the solution flow direction, while atomic force microscopy (AFM) images show that the composite nanofibers align predominantly parallel to the flow direction.

A photograph of the polydimethylsiloxane (PDMS) microfluidic chip used for materials deposition is shown in Figure A.1, along with the chemical structures of the dye and polyelectrolyte employed.

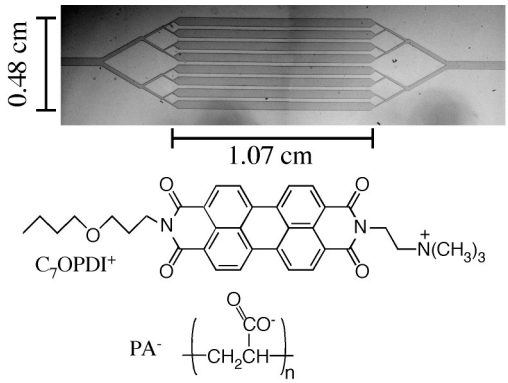

Figure A.1 Microfluidic chip and Dye and Polyelectrolyte structure

Microfluidic devices were prepared by casting uncured PDMS on a mold and curing it at 80 ^{o}C for 1 h. The resulting PDMS chip was subsequently pealed from the mold, oxidized in an air plasma and pressed onto a plasma-cleaned microscope cover glass. A single solution inlet and an outlet were then fashioned in the PDMS. Tubing from the outlet was connected via a flow regulator to a vacuum pump.

The dye used in nanofiber deposition, N-(3(butoxypropyl)-N'- (2-(trimethylammonio)ethyl) perylene-3,4,9,10-tetracarboxylic diimide iodide ($C_7OPDI^+ \bullet I^-$) was synthesized as reported previously.[8] Sodium poly(acrylate) (PA^-) was employed as the polyelectrolyte. PA^- was obtained from Aldrich and used as received. Aqueous solutions of C_7OPDI^+ and PA^- were prepared in high purity (18 MΩ•cm) water. Aqueous C_7OPDI^+ solutions were obtained by first preparing a 76.6 μM methanolic stock solution. The stock solution was subsequently concentrated to 306 μM, followed by addition of an equivalent quantity of water and evaporation of the methanol. To ensure complete removal of the methanol, an equivalent volume of water was added a second time and the excess solvent again evaporated, yielding a final C_7OPDI^+ concentration of 306 μM. PA^- was dissolved directly in water to obtain a 268 μM PA^- (monomer) aqueous solution.

Deposition of $C_7OPDI^+ \bullet PA^-$ composites was accomplished by alternately pulling 10 μL aliquots of the C_7OPDI^+ and PA^- solutions through the microfluidic chip. Pure water was used to rinse unbound material from the channels after each step. Films deposited in 5, 10 and 20 deposition cycles were prepared and characterized. Each cycle involved passage of four aqueous solutions (dye, rinse, polyelectrolyte, rinse) through the channels. Samples were prepared using solution flow velocities controlled at 2.0, 2.6 and 2.9 cm/s. After film deposition, the PDMS chip was removed and the samples were allowed to dry in air.

The dried films were characterized first by measuring their bulk UV-visible absorption dichroism. In these studies, the absorption spectrum for each sample was obtained using light polarized alternately parallel ($A_{\parallel}$) and perpendicular ($A_{\perp}$) to the solution flow direction during film deposition. Representative raw absorption spectra obtained are shown in Figure A.2A. To obtain the peak absorbance, each spectrum was fit to a double Gaussian and the amplitude of the main component centered near 480 nm was recorded. The peak absorbance values were corrected for the 32.4% open (uncoated)

area of each film. The average absorbance measured from films prepared in 5, 10, and 20 deposition cycles is shown in Figure A.2B. These data show a linear increase in film absorbance with number of deposition cycles, similar to the behavior commonly observed in other LbL depositions.[11] The rightward shift in the data reflects inefficient deposition of material during the first few cycles.[1]

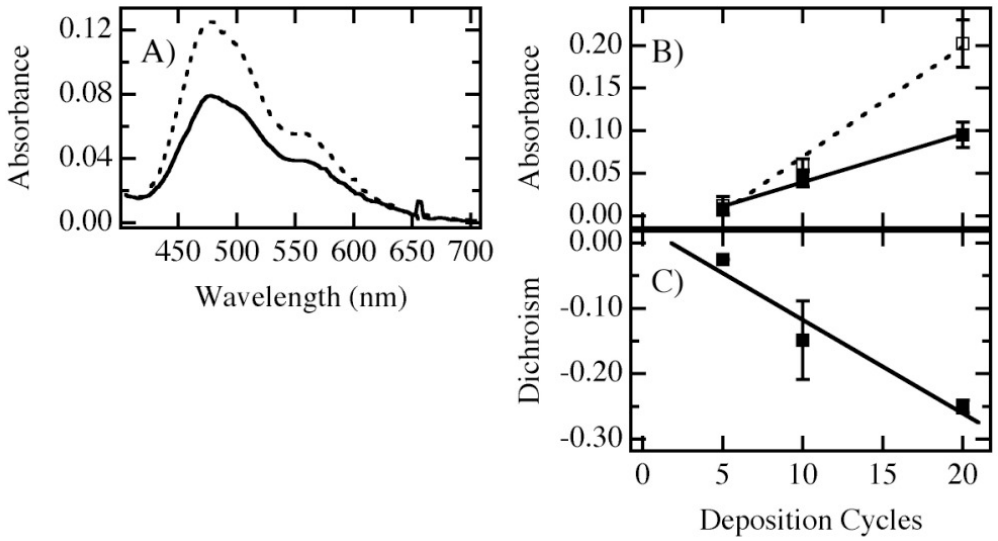

Figure A.2 A) Polarized absorbance spectra dotted spectra was obtained with light polarized perpendicular to solution flow direction, solid line spectra was obtained with light polarized parallel to the solution flow direction. B) Plot showing the absorbance dependence on number of deposition cycles. C) Dichroism data showing enhanced PDI order with larger numbers of deposition cycles.

The spectra show that the film absorbance is greater for light polarized perpendicular to the solution flow direction. Representative dichroism data, $D = (A_{\parallel} - A_{\perp})/(A_{\parallel} + A_{\perp})$, are plotted in Figure A.2C. As the electronic transition involved in C_7OPDI^+ absorption is polarized along the long molecular axis,[12] these results prove that the dye molecules align predominantly perpendicular to the solution flow direction. The absorption spectra also depict a blue shift from the monomer spectrum of the dye (peaked at 522 nm) in solution, reflective of the π-stacked C_7OPDI^+ aggregates that form in these materials.[8] From the absorption dichroism data, it may then be concluded that the π-stacks run parallel to the solution flow direction.

As has been shown previously, π-stacked perylene diimides frequently form nanofibers.[8,13] These same nanofibrous structures are formed in the present materials, as

evidenced in tapping mode AFM images. A representative example of the topographic images obtained is shown in Figure A.3A. Nanofibers 100-200 nm wide and several micrometers long are clearly visible in the image. Similar nanofibers were observed in AFM images acquired from samples prepared in 5, 10, and 20 deposition cycles. Average fiber size (cross-section) was observed to increase with the number of deposition cycles.[8]

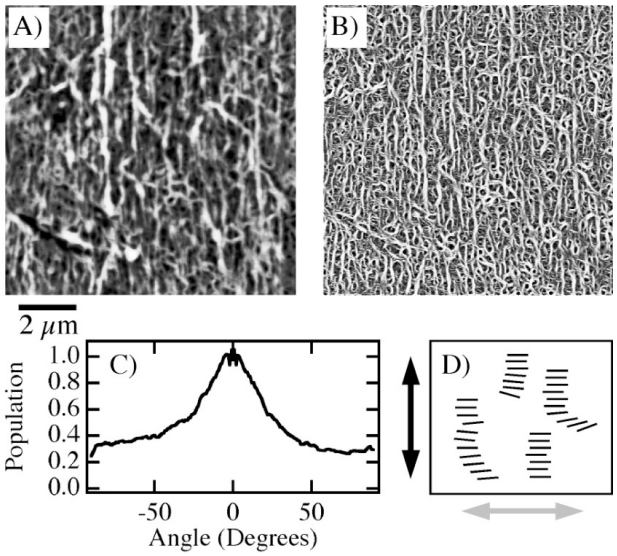

Figure A.3 A) TM-AFM image of C_7OPDI$^+$/PA$^-$ composite B) "ridges" image depicting the fiber orientation. C) Angle histogram obtained from the masked eigenvector data (not shown). D) Nanofiber model, dark arrow indicates direction of nanofiber alignment while the lighter arrow indicates the positioning of the PDI chromophore.

The AFM images obtained provide clear evidence of nanofiber alignment along the solution flow direction (vertical on the images), although not all images show significant alignment. The degree of nanofiber alignment in each image was obtained using previously-reported image analysis procedures.[14] In this process, the eigenvalues of eigenvectors of the image Hessian are first calculated. Figure A.3B shows the negative eigenvalue image obtained from Figure A.3A, depicting the image ridges.[14] The latter image better depicts the fibers. A thresholded version of Figure A.3B was used as a mask to construct a histogram of image feature alignment angles from the eigenvector data. The angle histogram obtained from Figure A.3A is given in Figure A.3C. These data provide additional proof that the predominant fiber alignment is along the flow direction

(zero degrees), although unaligned image features (fibers and other structures) are also present.

AFM and dichroism data obtained from films prepared with different numbers of deposition cycles show that film organization improves with the number of deposition cycles employed. Unfortunately, no clear dependence of alignment on flow rate was observed over the range of accessible values.

Taken together, the dichroism and AFM results indicate the fibers are comprised of aligned, π-stacked C_7OPDI^+. The molecules are oriented perpendicular to the solution flow direction, while the π- stacks and nanofibers formed align parallel to the solution flow, as depicted in Figure A.3D. Nanofiber alignment is attributed to flow induced orientation of short preformed C_7OPDI^+ aggregates in the aqueous deposition solution and/or shear-flow alignment of previously deposited nanofibers in later deposition cycles. Nanofiber alignment is not caused by mechanical contact between the AFM probe and the sample. The fast-scan direction in all images was perpendicular to the dominant fiber alignment direction. Future studies will include in depth exploration of nanofiber alignment and dye orientation as a function of deposition cycles, flow rate, electrolyte concentration and microfluidic channel parameters.

REFERENCES

(1) Decher, G. Science 1997, 277, 1232-1237.

(2) Mwaura, J. K.; Pinto, M. R.; Witker, D.; Ananthakrishnan, N.; Schanze, K. S.; Reynolds, J. R. Langmuir 2005, 21, 10119-10126.

(3) Mattoussi, H.; Rubner, M. F.; Zhou, F.; Kumar, J.; Tripathy, S. K.; Chiang, L. Y. Appl. Phys. Lett. 2000, 77, 1540-1542.

(4) Sirringhaus, H.; Wilson, R. J.; Friend, R. H.; Inbasekaran, M.; Wu, W.; Woo, E. P.; Grell, M.; Bradley, D. D. C. Appl. Phys. Lett. 2000, 77, 406-408.

(5) Chen, X. L.; Lovinger, A. J.; Bao, Z.; Sapjeta, J. Chem. Mater. 2001, 13, 1341-1348.

(6) Grell, M.; Bradley, D. D. C. Adv. Mater. 1999, 11, 895-905.

(7) Schneider, T.; Lavrentovich, O. D. Langmuir 2000, 16, 5227-5230.

(8) Everett, T. A.; Twite, A. A.; Xie, A.; Battina, S. K.; Hua, D. H.; Higgins, D. A. Chem. Mater. 2006, 18, 5937-5943.

(9) Barker, S. L. R.; Tarlov, M. J.; Canavan, H.; Hickman, J. J.; Locascio, L. E. Anal. Chem. 2000, 72, 4899-4903.

(10) Jang, H.; Kim, S.; Char, K. Langmuir 2003, 19, 3094-3097.

(11) Ferreira, M.; Rubner, M. F. Macromol. 1995, 28, 7107-7114.

(12) Kazmaier, P. M.; Hoffmann, R. J. Am. Chem. Soc. 1994, 116, 9684-9691.

(13) Balakrishnan, K.; Datar, A.; Oitker, R.; Chen, H.; Zuo, J.; Zang, L. J. Am. Chem. Soc. 2005, 127, 10496-10497.

(14) Elbischger, P. J.; Bischof, H.; Regitnig, P.; Holzapfel, G. A. Pattern

Appendix B - I-V curve Measurements

At several points in the course of this research project attempts were made at constructing rudimentary photovoltaic devices, and testing them for their photo-conversion efficiency. Although the results of these measurements were inconclusive, several new advancements were made that significantly increased sample throughput.

The two main types of samples constructed were bulk heterojunction devices and layered devices. Figure B.1 shows pictorially the difference between bulk heterojunction, right and layered devices, left.

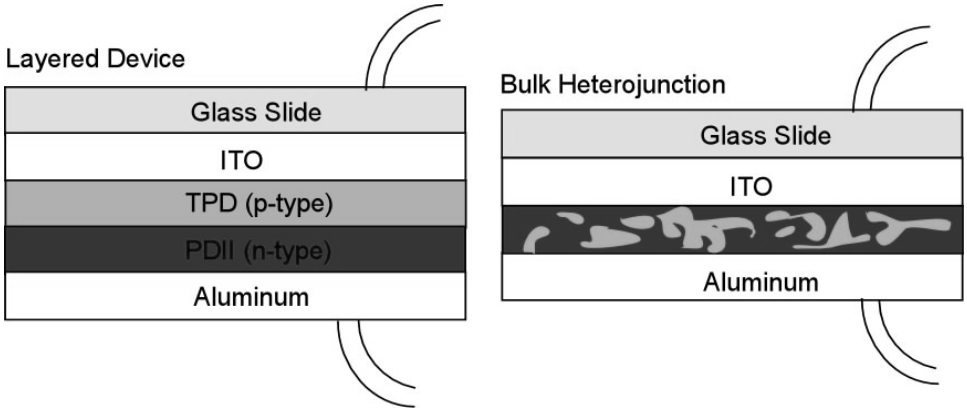

Figure B.1 Schematics of layered (left) and bulk heterojunction (right) solar cells.

For these two types of samples a perylene diimide derivative mixed with poly(acrylic) acid acts as the n-type semiconducting layer, and the p-type semiconducting layer is composed of N,N'-Bis-(3 methylphenyl)-N,N'-diphenylbenzidine (TPD) mixed with polyvinyl pyridine (PVP). External electrical contacts were made to the ITO substrate and the aluminum/silver back contacts using small copper wires and silver paint. These electrical contacts, once established were secured by either super gluing the wires to the ITO surface, or by encasing the entire device in UV curable optical adhesive. The preferred method was completely encasing the device with transparent optical adhesive as it limited the amount of oxygen and moisture that the devices were exposed to.

Testing of the devices was straightforward, the exposed sample wires were connected to the Keithly brand electrometer. The ITO lead was connected to the voltage source of the electrometer and the aluminum/silver lead was connected to the red lead (of the 3 lead bundle) for current measurement. It is important that the internal interconnect is active (this is set in the set-up menu of the electrometer) for this measurement to work correctly. Then, using the IVsweep.vi, labview program the initial voltage, final voltage and voltage steps are set. Upon execution of the program the voltage source is turned on and the current is measured, this is repeated until the program has completed the desired IV sweep. At the conclusion of the voltage sweep, the program stops and asks to save the data as a text file, that may be opened in Microsoft Excel or Igor Pro for further analysis. Characteristic IV curves are shown in Figure B.2A and Figure B.2B

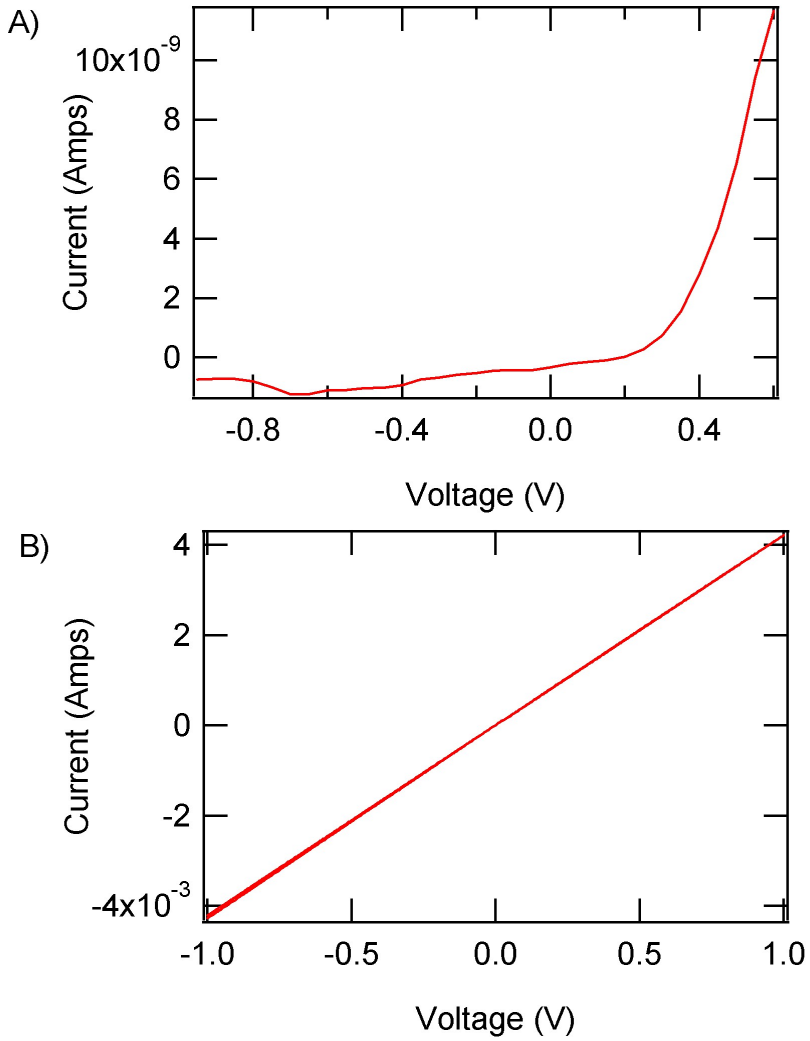

Figure B.2 Represenitive IV curves collected using the electrometer and IVsweep.vi program. A) Good IV curve demonstrating non-linear "diode-like" behavior. B) IV curve demonstrating the "ohm's law" behavior, indicative of a non-functional device.

While attempting to make working PV devices it became obvious that the previous way of making I-V curve measurements was flawed, sample throughput was low, and less than 10% of samples showed any "diode-like" behavior. This deficit was solved in two ways, first, multiple devices were constructed on a single indium tin oxide coated coverslip, and second, the development of a flexible, reusable back electrode. The following describes the procedure used to make the conductive PDMS electrodes.

Conductive PDMS

In order to make consistent, pin hole free electrical contacts to the thin films conductive polydimethylsiloxane (Sylguard 184) was made. A quick search of the literature showed that others have successively made PDMS conductive by doping in carbon black and silver nanoparticles.[1, 2] For our purposes we added 1 g silver nanoparticles of varying diameters to 0.5 g elastomer and 0.05 g curing agent. This produced a viscous slurry of nanoparticles. The 66% (w/w) slurry of nanoparticles was then transferred to a small syringe with a hypodermic needle attached. The syringe acted as a convenient dispenser of the slurry, allowing for precise control of the amount of conductive PDMS dispensed. Other weight percents of silver doped PDMS were made, however when silver levels were less than 66% by weight reliable conductivity was not achieved.

The conductive PDMS was then used to make the flexible back electrode of the photovoltaic device. The back electrode, where electrical contacts were made, was constructed by first casting a block of pure PDMS onto a smooth glass substrate mixing the monomer and hardener at the recommended 1:10 ratio. The pure PDMS block was then cured at 80 °C for 1h. After 1 h the elastomer was easily separated from the glass substrate. Then using a 1.5 mm biopsy punch six holes were cut into the PDMS block. After the holes were made the pure PDMS block was cleaned then adhered to a clean pane of glass. The holes were then filled with the conductive PDMS mixture and copper

wires were inserted into the conductive PDMS cylinders. The electrode assembly was then placed back in the oven at 80 degrees for 12 hours to insure all PDMS was completely cured. Figure B.3 shows the flexible, conductive PDMS electrode array. For clarity the wires are not shown.

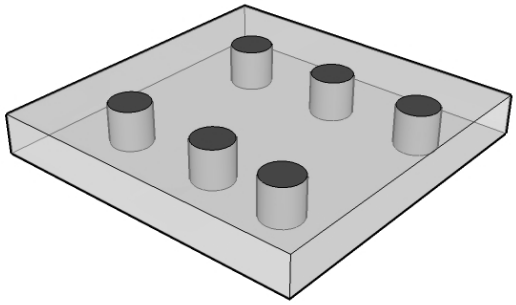

Figure B.3 Schematic of conductive PDMS electrode array. Dark areas indicate areas of conductive PDMS doped with 66% (by weight) silver nanoparticles.

Patterning of indium tin oxide electrodes

In order to achieve patterned ITO electrodes an etching procedure was employed, that allowed for arbitrary electrode structures to be made. The ITO etch solution is described at http://www.delta-technologies.com.[3] The entire procedure to produce patterned ITO electrodes is described below.

1. Plasma clean ITO coated glass.
2. Prepare appropriate photomask for use with a positive photo resist. Positive photoresist becomes liquid when exposed to light. For this work printing a mask on overhead transparency film was sufficient.
3. Spin coat positive photo resist onto the clean ITO coated glass and cure film per manufacturer's procedure.
4. Expose photoresist through the photomask, this will liquefy all areas that were exposed to the UV light.
5. Rinse ITO coated glass in appropriate developer, removing all liquefied photoresist and exposing the ITO layer that will be removed by etch solution.

6. Prepare etching solution: 20% HCl, 5% HNO_3 (by volume), plus a few drops of liquid soap to promote ITO wetting.
7. Heat acid solution to 55 °C.
8. Dip patterned slide into acid solution for 30-60 s. Alternately, if room temperature acid solution is used dip ITO slide into etch solution for 6-10 min. It may be required to experiment with etch times to obtain the best results.
9. Immediately after removal from acid solution rinse the glass slide in 10% solution of sodium bicarbonate to neutralize the acid. After acid is neutralized rinse with distilled water.
10. Last remove any photoresist using appropriate solvent, exposing the non-etched ITO electrodes. At this point the electrodes may be cleaned and used for PV device construction.
11. Note: The acid solution used for this procedure is very corrosive and should be handled with care. Once finished with the acid solution be sure to dispose of it correctly, i.e. neutralize and rinse down the sink with lots of water. In addition the etching rate of the ITO was highly dependent on the temperature and the concentration of the acid solution.

A schematic of resultant patterned electrodes is shown in Figure B.4. The ITO coated layer is indicated by the darker "T" shaped areas.

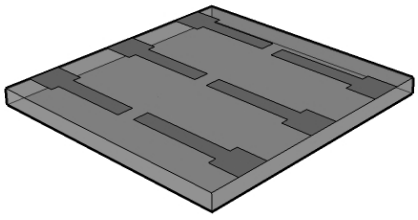

Figure B.4 Typical Patterned ITO Coated Glass Substrate

REFERENCES

(1) Liu, L.; Peng, S.; Niu, X.; Wen, W. *Applied Physics Letters.* **2006**, *89*, 223521.

(2) Chiu, H. T.; Wu, J. H. *Journal of Applied Polymer Science.* **2005**, *97*, 711.

(3) http://www.delta-technologies.com/downloads/applicationnotes.pdf?C=8

Appendix C - Multiphoton photolithography

The fabrication of structures to be used in applications ranging from microelectronic circuits to micro/nanofluidic devices may be accomplished using a wide variety of lithographic techniques.[1,2] The smallest such structures are usually prepared by X-ray or electron-beam lithography, but these methods require expensive, sophisticated instrumentation. As a result, ultraviolet (UV) photolithography is much more commonly employed in the fabrication of devices for chemical applications. In conventional photolithographic procedures, a commercial photoresist is typically exposed through an optical photomask that defines the polymer regions to be later removed using a chemical developing agent. The spatial resolution obtained is frequently limited by the chemical development step, the quality of the photomask employed and by diffraction of light from the mask. As a result, researchers have long sought alternative lithographic procedures that can produce higher resolution structures without the use of photomasks and chemical developers.

In this appendix, direct-write, high-resolution multiphoton photolithography in poly(methylmethacrylate) (PMMA) films is demonstrated using femtosecond pulses of near infrared (IR) light from a mode-locked Ti:sapphire laser. Laser-based lithography has been demonstrated previously in PMMA;[3,4] however, these studies employed pulsed UV light to drive multiphoton etching[3] or mid-IR light to drive thermal processes.[4] None of these demonstrated high-resolution lithography, instead depicting structures tens of micrometers in size. High resolution multiphoton photolithography has been demonstrated using different polymers in other reports.[5-11] These studies also demonstrated that three-dimensional structures could be fabricated using either positive-[5,8] or negative-tone[6,7,10] photoresists. Unfortunately, common commercial positive-tone resists are gradually “exposed” if used in the presence of light and may delaminate from

the substrate surface when immersed under liquids (i.e. water).[12] The photolithographic procedures demonstrated here allow for the use of robust PMMA films identical to those employed in deep-UV,[13] X-ray and electron-beam methods. Important advantages of this method include: I) the etching process does not require use of photomasks or chemical developers, II) the etched films are stable under aqueous solution, III) etching is driven by irradiation at near-infrared wavelengths and IV) high-resolution structures may be prepared.

For these studies, PMMA films were spin-cast (2000 rpm) onto glass and indium-tin-oxide (ITO) coated glass cover slips. Prior to use, each substrate was thoroughly cleaned in a plasma cleaner. PMMA and other polymers were obtained from Aldrich and used as received. The PMMA samples had molecular weights of 15,000, 120,000 and 350,000 (MW). Films were cast using solutions ranging from 1-7 wt% in PMMA. Usable films were obtained from a variety of solvents (i.e., chlorobenzene, chloroform or toluene). Equivalent-concentration solutions of the three different PMMA molecular weights yielded films of different thicknesses, but otherwise, the etching properties were indistinguishable. Prior to etching, the PMMA films were annealed in a vacuum oven at 110°C for ≈ 8 h. Final film thickness was characterized using a spectroscopic ellipsometer. Films having thicknesses from 50 nm up to 1.5 μm were prepared. Generally, films of < 350 nm thickness were found to work best for etching, while somewhat thicker films (350-650 nm) gave the best electrochemical data.

Etching of the PMMA films was performed using a confocal microscope.[14] This system is built upon an inverted light microscope and employs a sample-scanning stage that incorporates closed-loop feedback in the X and Y directions. The light source used for etching was a mode-locked Ti:sapphire laser outputting 170 fs pulses (at 76 MHz) centered at 870 nm. Light from the laser was first passed through polarization optics to control the incident laser power. It was subsequently directed through the epi-illumination port of the microscope and into the back aperture of a 1.3 numerical aperture (NA), 100X oil-immersion objective. This objective produced a focused spot of ≈ 570 nm $1/e^2$ diameter in the sample. All incident powers quoted in this appendix are estimates of the power at the objective focus and were measured outside the microscope. Etching was controlled using National Instruments Labview-based microscope control software

written in-house. An electronic shutter positioned in the laser beam path was used to control irradiation of the sample. Hence, arbitrary patterns (including text) could readily be etched into the films. Etching was verified using conventional far-field optical microscopy. Detailed characterization of the etched films, however, was performed by contact-mode imaging in air, using a Digital Instruments Multimode atomic force microscope (AFM).

Figure C.1a and Figure C.1b show AFM topography and deflection mode images of a text pattern etched into a PMMA film. This pattern was produced using 25 mW average power, with a 10 ms irradiation time at each of the 100 nm pixels in the etched region. The AFM data shown in Figure C.1a and in the line profile depicted in Figure C.1c clearly show that the vast majority of the PMMA was removed, without the use of a chemical developer. However, the increased "roughness" depicted in the deflection mode image (Figure C.1b) and in the line profile suggests that a small amount of debris remains behind.

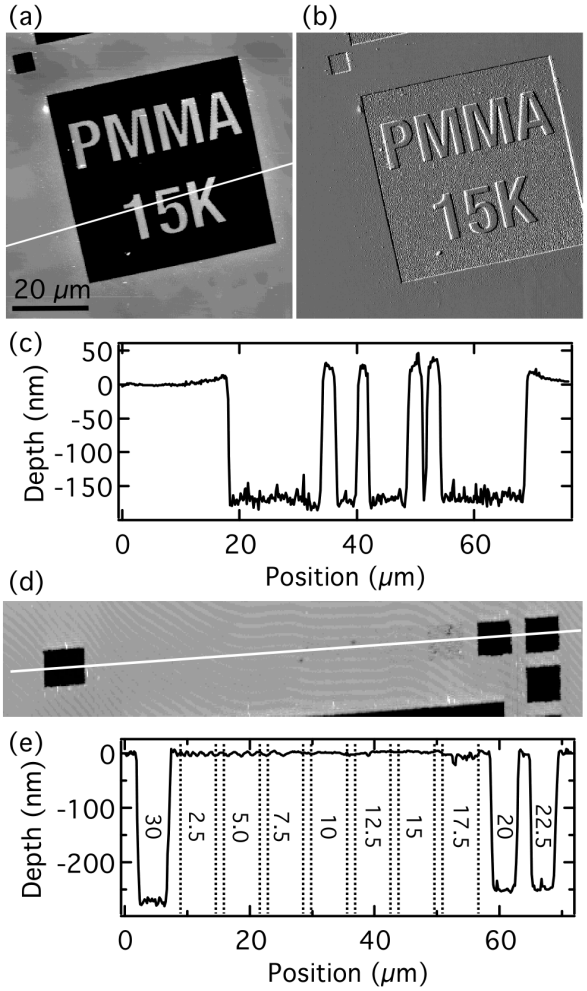

Figure C.1 Multi-photon etched films. A) and B) Topographic and deflection mode image of etched area. C) Line scan taken from the topographic image shown in frame A). D) and E) topographic image and line scan showing dependence of etch depth on incident power.

The mechanism by which etching occurs clearly involves nonlinear interaction of the PMMA with the incident laser light. The films could not be etched with the laser operating in continuous wave mode, indicating that very high peak intensities are required to drive the process. The power dependence of the etching process provides further evidence for the nonlinear nature of PMMA etching. Figure C.1d shows an AFM image depicting a series of ten 5x5 μm regions irradiated at different laser powers, while Figure C.1e depicts a line profile taken from this image. Each irradiated region is

designated in Figure C.1e by pairs of vertical dashed lines and is labeled with the power employed (in mW). Most of these regions show no detectable changes in their appearance (i.e. no etching occurred). However, at average powers above a threshold of ≈ 17.5 mW, clear etching is observed. A similar threshold was obtained for all three PMMA molecular weights. At powers above threshold (i.e., ≥ 20 mW), most of the PMMA is removed. The etch pits observed above threshold extend all the way to the glass surface. The abrupt power-dependent transition from no etching to almost total removal of the PMMA proves that the process is highly nonlinear. Future work will address both the power dependence and etching results of the lithographic process in this abrupt transition region.

At present, the detailed mechanism by which etching occurs is unknown. However, it is believed to involve simultaneous absorption of multiple photons at 870 nm by the UV chromophores (the methacrylate functional groups) in PMMA. PMMA absorbs in one-photon experiments at wavelengths shorter than 260 nm,[3,13] indicating the process may involve four photon absorption. To test this hypothesis, PMMA was substituted with poly(styrene) (PS) and poly(ethylene oxide) (PEO). PS films were easily etched at similar powers, as expected if the benzene ring acts as the chromophore in PS. In contrast, the PEO films showed no apparent etching at powers as high as 80 mW. It is noteworthy that PEO absorbs more deeply in the UV than the other two. As a result, PMMA etching likely occurs by four-photon absorption of 870 nm light, leading to depolymerization. Excess heat generated in the process then vaporizes the majority of the polymer fragments.

The nonlinear nature of etching indicates that high-resolution features should be obtainable. Sub-diffraction-limited etching is indeed observed, as depicted in Figure C.2

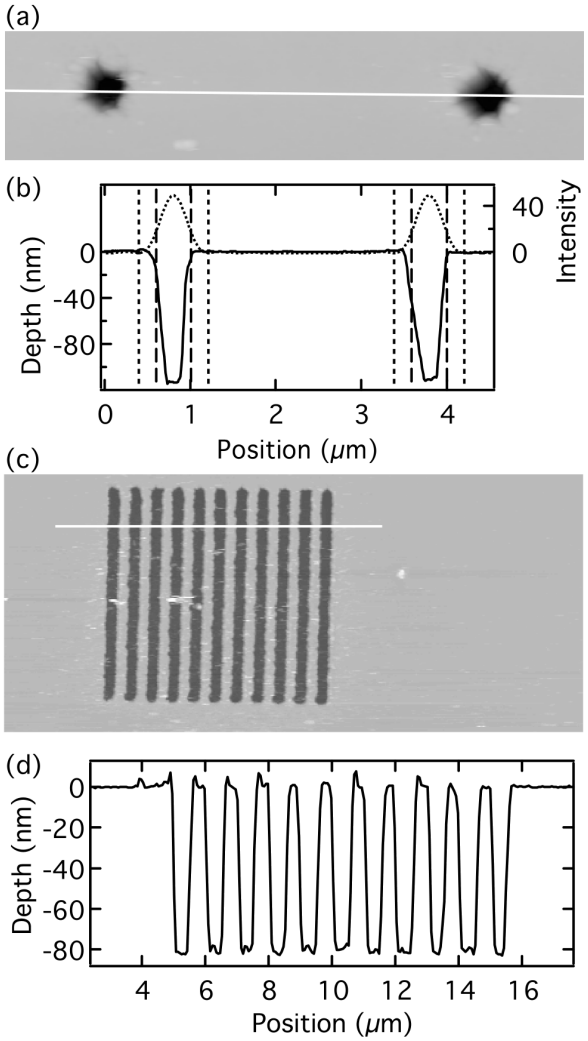

Figure C.2 High molecular weight PMMA etching. A) AFM image showing two holes etched using a laser power of 25 mW. B) line profile taken from image A showing etch depth and diffraction-limited Airy intensity profile expected at the laser focus. C) and D) image and line profile showing the remarkable edge sharpness that is possible with this multiphoton etching technique.

Figure C.2a shows two holes etched into a PMMA film of ≈ 100 nm thickness. These holes were etched using an average power of 25 mW, with each point in the sample being irradiated for ≈ 0.5 s. Similar holes could be prepared by etching at this same power for as little as 10 ms. A line profile plotted across the holes is shown in Figure C.2b. The flat bottoms on the etched holes and the close correspondence of their depths to those of nearby (larger) etched features indicate the film was etched all the way to the underlying glass surface. To define the hole diameter expected for etching by a

linear optical process, Figure C.2b also plots the diffraction-limited Airy intensity profile expected at the laser focus. Also shown are the resolution-limited hole diameters for linear and fourth-order processes (vertical dashed lines). These points correspond to distances of $\pm 0.61\lambda/(NA\sqrt{n})$, where n is the order of the process, from the center of each hole. As is readily apparent, each hole is significantly smaller than expected for a linear process. While it is broader than expected for a fourth-order process, some additional broadening may occur due to optical aberrations, optical disturbances that arise during etching and thermal diffusion into the unirradiated regions.

Additional evidence for the high-resolution capabilities of this method is presented in Figure C.2c and Figure C.2d. These data show a surface relief grating etched into an ≈ 80 nm thick PMMA film. The total width of the etched lines (≈ 670 nm at the upper PMMA surface) is again smaller than expected for an aberration-free linear process. The etched features also show remarkable edge sharpness. The lateral distance over which the transition from unetched PMMA to exposed glass occurs is ≈ 150-180 nm. Similar results have been obtained from numerous other etched patterns, such as the holes shown in Figure C.2a. Such transitions have been observed to occur over distances as small as 120 nm, although these results may be broadened by convolution with the AFM probe.

To further characterize the quality of the etched PMMA films and to demonstrate one potential application, "microelectrodes" for use in electrochemical experiments were fabricated on PMMA-covered ITO-coated cover glasses. For these experiments, single recessed disc microelectrodes of 5 μm, 10 μm and 20 μm diameters were fabricated in separate PMMA films of ≈ 600 nm thickness. Each disk was etched twice to remove any debris leftover from the first pass, as noted in the discussion of Figure C.1b. Ferricyanide solutions and cyclic voltammetric (CV) methods were then employed to determine the degree to which the unetched PMMA surface insulates the ITO-coating and to obtain a clear measurement of the size of the etched area.

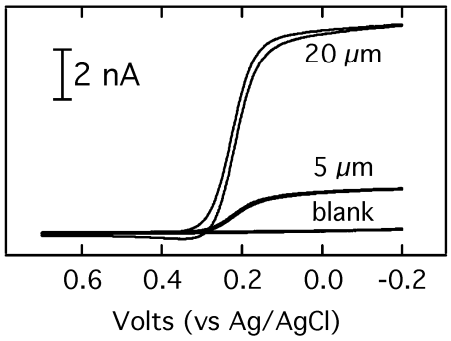

Figure C.3 Cyclic voltammetry on fabricated microelectrodes showing current dependence on electrode size.

Figure C.3 shows the results obtained for unetched and etched PMMA-coated ITO electrodes in 3.0 mM $K_3Fe(CN)_6$ solutions. Whereas the unetched electrode gave no redox current, the etched electrodes exhibited CVs of sigmoidal shape, as expected for single recessed disk microelectrodes at which semi-infinite hemispherical diffusion of the redox species into the hole occurs. The limiting current (i_{lim}) observed was found to depend on the disk radius as given by the following equation:[15]

$$i_{\lim} = \frac{4\pi nFC^b Da^2}{4L + \pi a}$$

In Eq. 1, n is number of electrons participating in the redox reaction [n = 1 for $Fe(CN)_6^{3-/4-}$], F is the Faraday Constant, C^b and D are the bulk concentration and diffusion coefficient of the redox species, and a and L are the radius and the recess depth of the disk electrode. The limiting currents observed for the 5-μm and 20-μm recessed disk electrodes in 3.0 mM $K_3Fe(CN)_6$ were 1.6 and 8.0 nA, respectively, close to the values predicted using Eq. 1 (2.0 and 8.1 nA, respectively). Similarly, i_{lim} for the 10-μm electrode (1.4 nA; data not shown) in 1.1 mM $K_3Fe(CN)_6$ was close to the theoretical value (1.5 nA). The close correspondence between observed and predicted currents indicates the PMMA has been totally removed from the etched region.

It should be noted that the PMMA-based recessed ITO microelectrodes are very stable; they can be cleaned repeatedly using H_2O_2:NH_3 = 1:3 and reused multiple times without degrading. In contrast, similar electrodes prepared using glassy carbon coated by

a conventional photoresist could only be used for 20 min prior to failure of the polymer coating.[12] The procedures for electrode fabrication are also much simpler than others reported previously.[16,17]

The potential applications for the multiphoton photolithographic process described here are broad and varied, encompassing chemistry, materials science and biosciences applications. The advantages of multiphoton photolithography over conventional photolithography include higher resolution and elimination of the need for a photomask and use of chemical developers.

REFERENCES

(1) G. M. Wallraff and W. D. Hinsberg, Chem. Rev. 99, 1801 (1999).

(2) Y. Xia, J. A. Rogers, K. E. Paul and G. M. Whitesides, Chem. Rev. 99, 1823 (1999).

(3) R. Srinivasan, E. Sutcliffe and B. Braren, Appl. Phys. Lett. 51, 1285 (1987).

(4) J.-Y. Cheng, C.-W. Wei, K.-H. Hsu and T.-H. Young, Sensors and Actuators B 99, 186 (2004).

(5) E. S. Wu, J. H. Strickler, W. R. Harrell and W. W. Webb, Proc. SPIE 1674, 776 (1992).

(6) B. H. Cumpston, S. P. Ananthavel, S. Barlow, D. L. Dyer, J. E. Ehrlich, L. L. Erskine, A. A., Heikal, S. M. Kuebler, I.-Y. S. Lee, D. McCord-Maughon, J. Qin, H. Rockel, M. Rumi, X.-L., Wu, S. R. Marder and J. W. Perry, Nature 398, 51 (1999).

(7) S. Kawata, H.-B. Sun, T. Tanaka and K. Takada, Nature 412, 697 (2001).

(8) W. Zhou, S. M. Kuebler, K. L. Braun, T. Yu, J. K. Cammack, C. K. Ober, J. W. Perry and S. R. Marder, Science 296, 1106 (2002).

(9) R. Allen, R. Nielson, D. D. Wise and J. B. Shear, Anal. Chem. 77, 5089 (2005).

(10) T. Baldacchini, C. N. LaFratta, R. A. Farrer, M. C. Teich, B. E. A. Saleh, M. J. Naughton and J. T. Fourkas, J. App. Phys. 95, 6072 (2004).

(11) X. Yin, N. Fang, X. Zhang, I. B. Martini and B. J. Schwartz, Appl. Phys. Lett. 81, 3663 (2002).

(12) K. Aoki and J. Osteryoung, J. Electroanal. Chem 125, 315 (1981).

(13) L. Myers and M. G. Spencer, J. Vac. Sci. Tech. B 4, 1259 (1986).

(14) B. J. Luther, G. H. Springer and D. A. Higgins, Chem. Mater. 13, 2281 (2001).

(15) A. M. Bond, D. Luscombe, K. B. Oldham and C. G. Zoski, J. Electroanal. Chem 249, 1 (1988).

(16) C. S. Henry and I. Fritsch, Anal. Chem. 71, 550 (1998).

(17) M. E. Sandison, N. Anicet, A. Glidle and J. M. Cooper, Anal. Chem. 74, 5717 (2002).

Tips and Tricks for using the Digital Instruments Multimode AFM

One caveat of AFM, or any scanning probe microscopy technique, is the impact the tip has on the observed images. For example, a dull tip will make all the surface features of an image appear wider than they actually are. If the tip is damaged, cracked, or has picked up a piece of debris, the image may start to show repeating features. Another example of the tip interfering with the collected image is observed when trying to image abrupt, deep features. In this case it is often the slope cantilever which is imaged and not the desired feature. In addition to the impact of the tip, it is also of utmost importance to set the feedback gain values correctly. When feedback values are set too low, the instrument is unable accurately follow the sample features; set too high, and an image artifact known "ringing" is observed. Below is the general procedure I used when setting up the AFM. Also shown are example images that demonstrate the results of damaged tips and improperly set feedback values.

Nanoscope III Operating Procedure

The Nanoscope III is a fairly easy to use AFM. This said, there are a few tricks that I have found to make setup quicker and easier. The following is the standard procedure that I followed for microscope set-up and imaging.

1. Turn on microscope at power strip.
2. Log into software and start the Nanoscope III operating software.
3. Mount cantilever into cantilever holder. (The Higgins group has their own, it should be located with the AFM supplies.)
4. Mount cantilever holder into the AFM head. Rotate the clamping screw located on the back of the AFM head to secure the cantilever in place.
5. Mount sample onto sample puck and place on the magnetic holder of the appropriate scanning stage. (two scanning stages are available, the "J" (max scan area of 100 x 100 um^2) and "E" scanner (max scan area of 10 x 10 um^2).

6. Carefully mount AFM head to the AFM base, be sure the cantilever does not come into contact with the sample. If necessary use the "Tip up" switch to lower the sample (raise the tip), preventing cantilever damage. Connect the securing springs.
7. Roughly align the laser onto the cantilever using the x- and y- laser adjustment knobs. Through experience, I found it easier to lower the tip close to the sample surface, then focus the camera system onto the cantilever shadow before attempting to align the laser.
8. Set Tapping Mode or Contact Mode on the AFM base, using the mode selector switch.
9. Carefully maximize the SUM signal using the photodetector mirror lever, located on the back of the head. Use the x- and y- laser position knobs to fine tune the maximum signal.
10. Center laser onto the photodiode. Using the mirror adjustment knobs located on the top left and back of the head to adjust the signal levels. For contact mode the vertical deflection (upper display on the base) should read ~ -1.00 V and horizontal deflection (bottom display) should read 0.00 V. Tapping mode the vertical deflection should read 0.00 V (bottom display)
11. Once sensor setting are correct, and the AFM is in the desired mode the software must be set-up.
    a. Double check you are using the correct microscope (i.e. multimode or extended multimode). Click on "DI" and select "microscope select", choose the correct microscope. Note: If phase imaging is required the extended multimode microscope must be selected.
    b. Select operation mode, click Microscope, then mode and select tapping mode or contact mode as appropriate.
    c. Lastly double check the correct scanner is used. Click "microscope" then "scanner". There are two options "E" scanner or "J" scanner, select the correct scanner.

12. If operating in contact mode, you are now ready to engage the tip. If operating in tapping mode the cantilever must first be auto-tuned. Below are typical settings and are only meant as guidelines, these setting may need to be changed depending on the samples and images obtained.

Contact mode:

i. SCAN SIZE = 10 μm
ii. ASPECT RATIO = 1 to 1 (default)
iii. X- and Y- Offset = 0 nm
iv. SCAN ANGLE = 0° (90° for friction measurements)
v. SCAN RATE = 1 Hz
vi. TIP VELOCITY = set by software
vii. Samples/line = 512 (max resolution)
vii. Lines = 512

b. Feed back controls for contact mode

i. Integral Gain = 2.00
ii. Proportional Gain = 3.00
iii. Set point = 0.00V

Tapping mode settings

i. SCAN SIZE = 10 μm
ii. ASPECT RATIO = 1 to 1 (default)
iii. X- and Y- Offset = 0 nm
iv. SCAN ANGLE = 0°
v. SCAN RATE = 1 Hz (or less)
vi. TIP VELOCITY = set by software
vii. Samples/line = 512 (Max resolution)
viii. Lines = 512

b. Feed back controls for tapping mode

i. Integral Gain = 0.50
ii. Proportional Gain = 0.70

13. To capture an image click on the camera icon, then restart the scan from the top or bottom. The capture status should change from “next” to “on”.
14. Before moving to new samples or new areas on current sample remember to disengage the tip.
15. To shut down the system, disengage tip and shut off power to the system. Remove your sample and cantilever (or cantilever holder) and remember to sign the log book.

Common Image problems and Examples

AFM is a scanning probe microscopy technique and the quality of the obtained images is dependent on the cantilever and the feedback parameter used in "tracing" the sample surface. Displayed below are a collection of images meant to help recognize possible feedback or cantilever tip problems based on the appearance of obtained images.

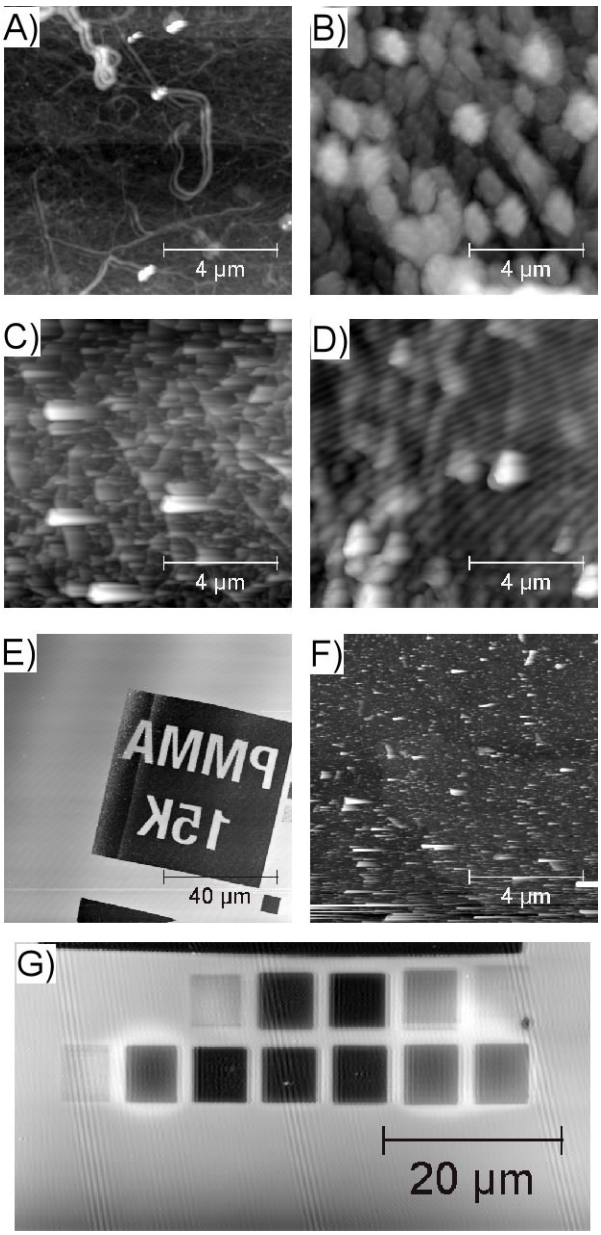

Figure 0.1 Collection of AFM images showing image artifacts and noise problems to be avoided. Images obtained with A) a double tip, B) a blunt tip, C) and F) feedback gain too low, D), E) and G) feedback gain to high.